Thermoelectric Properties of Carbon Nanotube Films

César Alejandro Miranda Reyes

Darwin College
University of Cambridge

This dissertation is submitted for the degree of
Doctor of Philosophy

March 2017

Thermoelectric properties of carbon nanotube films

César Alejandro Miranda Reyes

Abstract

Thermoelectric generators are solid state machines used to convert temperature gradients into electrical energy. They are formed by several thermoelectric units connected electrically in series and thermally in parallel. These units are made by creating a junction between a p-type and an n-type conductor. This investigation documents the characterisation of the thermoelectric properties of carbon nanotube (CNT) films and the fabrication process of carbon nanotube-based thermoelectric devices.

The Seebeck coefficient is a intrinsic property of a thermoelectric material that correlates the voltage produced by a conductor and the temperature gradient applied to it. To measure the Seebeck coefficient of films, an experimental set-up was fabricated and calibrated using constantan as standard material. CNT films of aligned nanotubes fabricated using a chemical vapour deposition method were analysed. The Seebeck coefficient along and across the samples did not show significant variations, with values between $40\,\mu V/K$ and $80\,\mu V/K$.

Using these CNT films, thermoelectric cells were fabricated with the CNT as the p-type conductor and constantan as the n-type. As a proof of concept, two hand-made thermoelectric generators were assembled by connecting hundreds of these thermoelectric cells. These devices were subjected to a temperature gradient of $\approx 200\,K$, which was enough to produce enough power to light an LED.

Other analytical techniques were used to characterise the materials used in this work. Electrical conductivity measurements, thermogravimetric analysis, Raman spectroscopy and scanning electron microscopy were performed.

Using a deposition technique, films of nanotubes were produced from a liquid phase. The impact of the production method on their properties was evaluated. Characterisation equipment was developed to measure the Seebeck coefficient and thermal conductivity. Thermoelectric devices made with the carbon nanotube films were fabricated and characterised.

The values of thermal conductivity of the CNT films analysed in this work are between $0.86\,W\,m^{-1}\,K^{-1}$ and $123.25\,W\,m^{-1}\,K^{-1}$. The electrical conductivity of these materials is between $3500\,S\,m^{-1}$ and $14\,100\,S\,m^{-1}$. The maximum figure of merit of the carbon nanotube thermoelectric devices fabricated in this work is $ZT = 0.35$.

To my parents Tomás and Verónica
and to my siblings Irving and Pamela,
with love and gratitude

Acknowledgements

I want to express my gratitude to all my colleagues, friends, and family. This accomplishment would have not been possible without their continuous support and encouragement.

I would specially like to thank my supervisor Dr. Krzysztof Koziol. I am thankful for introducing me to this challenging but rewarding topic. I am very grateful for the trust you placed in me and for your guidance in the development of my own ideas. Thank you for helping me bring this project to a satisfactory conclusion.

I am very thankful to the Cambridge trust and to CONACYT for their support. Concluding my PhD was only possible with the sponsorship of these institutions.

I want to express my sincere gratitude to Dr Gari Owen for his support during these years, for his help in getting the necessary funds to start this project. Most importantly I would like to thank him for his engagement with the project, for all the fruitful discussions that encouraged me to pursue new ideas.

I will always be grateful to my parents and siblings for their continuous love and support. Thank you for being there for me. I want to thank my friends Alejandro, Armando and Oliver who are always there to talk with me about - everything. Steffi, thank you for reading my work and for all your advices, you are an amazing friend. Karol and Ola, thank you for your endless company and support, you have been my family in England. To my friends Peter, Clara, Craig, Kasia, Enrique and Daniela, you all are what have made Cambridge my home. Fernando, Liz, Ricardo, José and all my friends in Mexico, thank you for all your thoughts and care. Magda - with love and patience you have motivated me to complete my PhD. I feel joy and excitement as we start our future together.

Contents

List of figures

1

Introduction

Carbon nanotubes (CNTs) are materials that have been widely researched over the past decade due to their interesting electrical, thermal and structural properties. CNTs are sought to replace or at least to upgrade some of the classic materials used in electronics and reinforcement applications [1]. In this dissertation, the use of carbon nanotubes as thermoelectric materials is investigated. Their properties and their application in the generation of energy from heat sources is discussed.

The aim of this work is to develop techniques and equipments to characterise the thermoelectric properties of CNT-based macroscopic materials. The fabrication of prototypes that demonstrate the use of nanotubes in energy generation is also within the scope of this work.

This first chapter discusses the thermoelectric theory, thermoelectric materials and their applications. In the second chapter the fabrication of a set-up to characterise the Seebeck coefficient of thermoelectric films is reported. This chapter also deals with the research on the Seebeck coefficient of constantan films, a classic thermoelectric material. The characterisation of the Seebeck coefficient of carbon nanotube films is also reported in this chapter. Using these materials the fabrication of a CNT-based prototype for harvesting electrical energy is discussed in chapter three.

In chapter four, the processing of carbon nanotube dispersions is investigated. The purpose of preparing CNT dispersions is to fabricate CNT thermoelectric devices using printing technology. Chapter five describes the fabrication of nitrogen doped CNT dispersions. These materials are then used to fabricate n-type semiconductors from the CNT dispersions.

In chapter six the fabrication of a set-up for the characterisation of the thermal conductivity of CNT films is presented. In this chapter the electrical stability of the CNT materials is also researched. In chapter seven the development of a 3D printing set-up is presented. The purpose of constructing this device was to develop a scalable method that can be used to manufacture CNT-based thermoelectric devices. In this final chapter, a fully printed thermoelectric device is demonstrated and characterised.

1.1 Thermoelectric phenomena

Thermoelectric phenomena are related to the conversion of thermal energy into electrical energy or the conversion of electrical energy into thermal energy. These phenomena can be observed in any electrically conducting or semiconducting material and are fully described by three related thermoelectric mechanisms; the Seebeck, Peltier and Thomson effects.

The first evidence of a thermoelectric effect was observed in 1821 by Thomas Seebeck, who reported a phenomenon which he described as *"Magnetic polarisation of metals and ores produced by a temperature difference"* [2]. He realised that a magnetised needle suspended near to a closed loop formed by two dry dissimilar metals was deflected when a temperature difference existed between the ends of the circuit. Seebeck did not understand the true nature of the phenomenon and concluded erroneously that the effect was caused by magnetic interactions and, trying to prove his hypothesis, he attempted to relate the Earth's magnetism to the temperature difference between the equator and the polar ice cap [3]. Based on Seebeck's account of his experiment, it is now known that what he observed was caused by thermoelectric currents arising in the closed circuit formed by the junction of the conductors; these currents were caused by the temperature difference between the junctions.

Despite Seebeck's erroneous conclusions, an important contribution of his work lies in the thorough characterisation he made of the effect in different materials. He compiled a considerable amount of experimental data and summarised

it in a series in which he classified a great variety of solid and liquid metals, alloys, minerals and semiconductors according to the magnitude of the product $\alpha \cdot \sigma$, where α is the Seebeck coefficient and σ the electrical conductivity. The Seebeck coefficient is an intrinsic transport property of any conductor material. Expressed in V/K, or more commonly in µV/K, it defines the strength of the Seebeck effect.

Correctly defined, the Seebeck effect refers specifically to any electric potential that results from the creation of a temperature gradient between the ends of an electrically conducting material. This effect is a voltaic phenomenon which occurs both in opened and closed circuits as well as in individual materials (not necessarily connected to an electric circuit), which means that the effect does not necessarily depend on the junction of dissimilar conductors. The Seebeck effect is the only thermoelectric effect that produces electrical energy. It creates an electromotive force that can drive the electric currents needed to produce the other thermoelectric effects.

A few years after Seebeck's finding, Peltier discovered a cooling and heating effect which takes place when a current passes through the junction of two different conductors [4]. He observed that when passing current in one direction through a bismuth - antimony junction, the vicinity of the boundary formed by the two materials was immediately cooled. Then, when he reversed the direction of the current passing through the same junction, he noted that the junction irradiated heat to its surroundings. This phenomenon is named Peltier effect and it relates the generation or absorption of heat at the junction formed by two dissimilar conductors. When the conductors form a closed circuit, a temperature difference between the junctions produces an electric current; if in turn, an external current is passed throughout the circuit, a temperature difference is created at the junction.

This effect is closely related to the Seebeck and despite the fact that Peltier was using a thermoelectric device as a source of weak currents, he did not realise the relationship to Seebeck's findings. Peltier was attempting to prove through his experiments that heat generation by current (Joule-Lenz law) was only possible using strong currents. He could not prove this hypothesis and instead found that the strength of the effect was determined by the nature of the metals at the junction. A definite proof that the effect was indeed related to the thermoelectric properties of the materials was provided by Lenz, who placed a drop of water at the junction of bismuth and antimony rods. He showed that to freeze 1 g of

water it is necessary to remove 80 calories and that to melt the same amount of ice, 80 calories must be supplied. This made it clear that depending on the direction in which an electric current is applied, heat can be either generated or absorbed. The rate of heat transport at the junction is proportional to the current (I) flowing through it, thus

$$\frac{dQ_{\Pi}}{dt} = \Pi I. \tag{1.1}$$

Where Q_{Π} is the heat transport at the junction and Π is the *Peltier coefficient* [5]. This coefficient is an inherent transport property of an individual material and it represents the irreversible thermal change produced at the junction when one Coulomb passes through it. The Peltier effect arises from the difference between the entropies of the conductors forming the junction, which itself manifests as the rate at which heat can be transported in the material. This difference causes heat to be absorbed or dissipated at the junction when current is flowing through it [6].

The third and last thermoelectric effect is the Thomson effect, named after William Thomson (Lord Kelvin) who, through a thermodynamic analysis of the conversion of thermal to electrical energy in the Seebeck and Peltier effects, established the relationship between these two processes and predicted the existence of a complementary effect for electrically conducting homogenous materials [7]. He analysed a thermoelectric closed circuit formed by two dissimilar conductors which joined ends were at different temperatures (Figure 1.1). He then realised that taking only into account the contributions of the Seebeck and Peltier effects, an expression defining the energy of the thermoelectric circuit as a linear function of temperature could be derived. This expression though, did not agree with the non-linear behaviour observed in thermocouples. To solve this discrepancy, he proposed an additional thermal change taking place in the individual thermoelements when they were subject to a temperature gradient. Some years later he proved the existence of his predicted effect by applying an external current to the thermoelectric circuit and observing an increase or decrease of the local heat (IR^2) in the thermoelements.

The Thomson effect is a reversible process concerning absorption or dissipation of heat in a single homogeneous conductor when current flows through a temperature gradient along the conductor. This effect is caused by the change in the potential energy of the carriers when they move in the same or in opposite direction to the temperature gradient. If the carriers (electrons or holes) flow

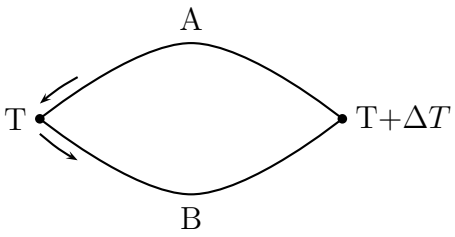

Figure 1.1: Diagram of a thermocouple formed by dissimilar conductors A and B with the junctions at different temperatures.

against the temperature gradient they absorb thermal energy increasing their potential energy; but when they move in the same direction as the gradient their potential energy decreases and energy is released [8]. These changes in the energy content of the material are known as the Thomson effect. The rate at which the heat exchange takes place due to the Thomson effect is proportional to the temperature gradient and to the current that passes through the conductor,

$$Q_\tau = \tau I \frac{dT}{dx}. \tag{1.2}$$

Where Q_τ is the heat exchange, τ is the Thomson coefficient, I is the current flowing through the conductor and dT/dx is the temperature gradient. The Thomson coefficient represents the energy change in the conductor per unit current and per unit temperature gradient along the conductor. Similarly to the Peltier effect, the Thomson effect is proportional to the current passing through the conductor regardless of whether the current is induced by thermoelectric effects in the circuit or if it is externally supplied. It is important to note that if there is no current flowing through the circuit, the Thomson and Peltier effect will not occur.

Thermoelectric circuits found their first applications in thermometry where they are used mainly as thermocouples. The possibility of using the thermoelectric phenomena as an alternative source of energy was firstly addressed by Lord Rayleigh, who calculated the efficiency of a thermoelectric generator [9]. The problem was retaken some time later by Altenkirch, who developed a correct theory of thermoelectric cooling and power generation [10, 11]. Altenkirch's theory showed that the efficiency of a thermoelectric device was related to the Seebeck coefficient, the thermal conductivity (λ) and electric conductivity of the thermoelements. He defined a parameter known as the *figure of merit* which embodies the transport properties of any thermoelectric material. This parameter

is given by

$$Z = \frac{\alpha^2 \sigma}{\lambda}. \tag{1.3}$$

where α is the aforementioned Seebeck coefficient, σ the electrical conductivity, λ the thermal conductivity and Z is the figure of merit. Equation 1.3 is extremely important and is the basis of the practical implementation of the thermoelectric effect.

During the first years of thermoelectricity the research was focused on metals and alloys. These materials have Seebeck coefficients of less than $10\,\mu V/K$ which lead to efficiencies of approximately 1 % [12]. Since in metals the ratio between the thermal and electrical conductivity is governed by the Wiedemman-Franz law, which states that it is not possible to increase the electrical conductivity without increasing the thermal conductivity, the room for improving the figure of merit of metal-based thermoelectric generators is very limited. For this reason, the research in thermoelectric generation waned for several years [13, 14].

The interest in thermoelectric power generation was renewed by the discovery of large Seebeck coefficients in synthetic semiconductors ($\approx 100\,\mu V/K$), which lead to the development of thermoelectric generators with efficiencies of 5 % [15]. Parallel to this, Ioffe developed a theory for semiconductors as thermoelements, predicting that heavily-doped semiconductors would have larger figures of merit [16]. Since then, it is clear that a successful application of thermoelectricity in power generation depends on understanding and controlling the factors affecting the thermoelectric properties of the different materials.

1.2 Thermoelectric theory

A thermodynamic analysis of thermoelectric phenomena provides a basic understanding of the relationship between the three thermoelectric effects. It is also a first approach to describe the properties observed in real thermoelectric circuits or thermocouples. Whereas this is useful to develop a model which takes into account the influence of the carriers on the thermoelectric properties of the material, it is necessary to follow an approach based on solid-state physics. In this section, the basic thermodynamic treatment of the thermoelectric effects is presented; this will lead to the fundamental thermodynamic theorem of thermoelectricity which summarises the interaction between the Seebeck, Peltier and Thomson effects. Following this development, the thermoelectric coefficients are derived using concepts of solid-state physics and quantum mechanics, which will

provide a better insight into the factors affecting the thermoelectric properties of different kinds of materials and will give an explanation of why certain materials are better thermoelements than others.

The thermocouple shown in Figure 1.1 is the simplest thermoelectric circuit and it is one of the most widely used electrical sensors. The voltage generated when a temperature difference is created between its junctions is the *relative Seebeck electromotive force*. Whenever the thermoelectric properties are associated to more than one independent material they are referred as *relative*. Although practical applications only make use of relative properties, which means that thermoelectric circuits are always formed at least by two thermoelements, the Seebeck characteristics also appear in individual materials. These properties of single conductors, which occur independently of any junction to another material, are known as *absolute Seebeck characteristics* and are important in practical and theoretical applications. Understanding the absolute characteristics can help to shed light into the electronic mechanisms governing the thermoelectric properties of materials and also helps in selecting good configurations of paired thermoelements.

If the ends of single homogeneous conductor are placed at different temperatures, a net Seebeck electromotive force (*emf*) will occur between the ends of the material, this is known as the *absolute Seebeck emf* (ASE). A change in the temperature gradient between the ends will produce a corresponding change in the ASE. The ratio between the change in ASE and the change in temperature is defined as the *absolute Seebeck coefficient* and it is expressed as

$$\alpha(T) = \frac{dE_\alpha(T)}{dT}, \tag{1.4}$$

where $\alpha(T)$ is the absolute Seebeck coefficient and $E_\alpha(T)$ is the ASE as a function of temperature (T) [17].

As stated in the equation, this coefficient and the emf are not constant quantities, they are a function of temperature. An example of this non-linear behaviour can be seen in the plot of the absolute Seebeck coefficient of platinum at different temperatures shown in Figure 1.2. The Seebeck coefficient is the local slope of the curve defined by the emf at different temperatures. In any real material, the Seebeck emf does not vary linearly with temperature, but for very small temperature ranges it can be assumed to be a linear function, which in practice permits the calculation of the Seebeck coefficient as the measured emf (E_α) divided by

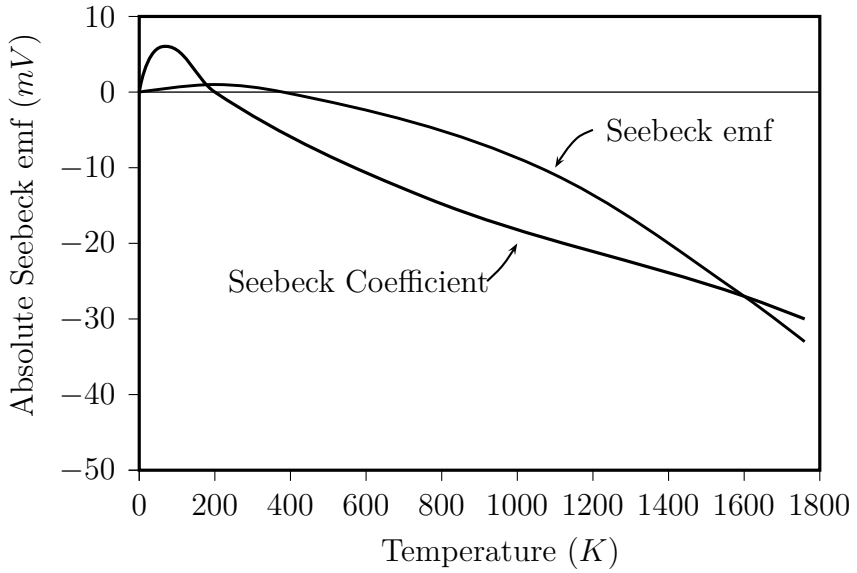

Figure 1.2: Absolute Seebeck emf and absolute Seebeck coefficient of pure platinum [18].

the temperature difference at the ends of the conductor

$$\alpha \simeq \frac{E_\alpha}{(T_2 - T_1)}, \tag{1.5}$$

where T_2 is the temperature at the hot side of the thermoelement and T_1 is the temperature at the cold side.

If any two points defining a non-isothermal segment of the homogeneous conductor are considered, where the temperature gradient between these points is given by the difference of T_1 and T_2, Equation 1.4 can be rewritten as

$$E_\alpha = \int_{T_1}^{T_2} \alpha(T) dT, \tag{1.6}$$

where the integral defines the absolute Seebeck emf produced by the conductor segment. This means that the net Seebeck emf measured between the end points of an homogeneous conductor can be interpreted as the sum of all the emf contributions of a series of adjacent non-isothermal segments forming the segment. The importance of this statement lies in the fact that it provides a tool to analyse inhomogeneous materials, since the overall Seebeck emf of a non-homogeneous conductor can be treated as the sum of all the Seebeck emf produced by a series of connected homogeneous segments forming the inhomogeneous material [6].

The relationship between the three thermoelectric effects can be obtained

analysing the thermoelectric circuit shown in Figure 1.1. Since the circuit is composed by two dissimilar conductors A and B, the thermoelectric properties of the system are relative Seebeck characteristics. If the temperature at the junctions is maintained as T for the colder junction and $T + \Delta T$ in the hotter junction, the relative Seebeck emf generated in the circuit (E_{AB}) is expressed in terms of the relative Seebeck coefficient (dE_{AB}/dT) per unit current as

$$E_{AB} = \frac{dE_{AB}}{dT}\Delta T. \tag{1.7}$$

Since it is assumed that a unit of current is passing throughout the circuit, the other two thermoelectric effects will also take place. The energies associated to the Peltier and Thomson effect can be expressed as the thermal exchanges within the circuit. In the case of the Peltier effect, the heat absorbed at the hotter junction is given by $\Pi_{AB}(T + \Delta T)$ and the heat liberated at the colder junction is $-\Pi_{AB}(T)$. For the Thomson effect, the heat exchange occurs throughout the conductors A and B; the heat absorbed by the conductor B is $\tau_B(\Delta T)$ and the heat liberated by the conductor A is $-\tau_A(\Delta T)$.

If the irreversible thermal losses produced by Joule heating (IR^2) are neglected[a], the thermoelectric circuit can be approximated as a reversible heat engine and the energy balance of the system can be written as

$$\frac{dE_{AB}}{dT}\Delta T = \Pi_{AB}(T + \Delta T) - \Pi_{AB}(T) + (\tau_B - \tau_A)\Delta T. \tag{1.8}$$

Where dE_{AB}/dT is the relative Seebeck coefficient, Π_{AB} is the relative Peltier coefficient and τ_A and τ_B are the Thomson coefficients of the thermoelements [8]. Again, this equation assumes a unit of current in the circuit.

Dividing Equation 1.8 by ΔT and considering an infinitesimal change in temperature ($\Delta T \to 0$) leads to

$$\frac{dE_{AB}}{dT} = \lim_{\Delta T \to 0}\left(\frac{\Pi_{AB}(T + \Delta T) - \Pi_{AB}(\Delta T)}{\Delta T}\right) + (\tau_B - \tau_A), \tag{1.9}$$

$$\frac{dE_{AB}}{dT} = \frac{d\Pi_{AB}}{dT} + (\tau_B - \tau_A), \tag{1.10}$$

where $d\Pi_{AB}/dT$ is the instantaneous rate of change of the Peltier effect in relation to the temperature [8].

[a] Considering that the electrical resistance of a thermocouple is small, less than $10\,\Omega$, the irreversible heat loss will be less than 10^{-5} W. Thus it can be neglected [5].

This equation is the *fundamental thermodynamic theorem* of thermoelectricity, it states the energy relationship between the Seebeck, Peltier and Thomson effects. It should be noted that the derivation of this equation was made for a closed circuit and that it was assumed a unit of current is flowing through it. In the case of an open circuit when there is no current present, only the Seebeck effect occurs; the Thomson and Peltier effect are current dependent. Therefore this equation is not valid for open circuits and shows that the Seebeck effect should not be regarded as the algebraic sum of the Peltier and Thomson effects but rather as the driving force for the currents that give rise to the latter effects in the case of closed circuits.

While the previous equations describe the observed thermoelectric phenomena, their derivation assumed a thermoelectric circuit and the flow of electric current. Considering the fact that the Seebeck effect is independent of the current and that it can also occur in isolated conductors, these equations cannot be regarded as the most fundamental description of the phenomenon. Thus, a more general approach is required to understand the properties of thermoelectric materials.

In broad terms, the distribution of the carrier in an homogeneous and isothermal conducting material can be considered uniform, with the carriers evenly distributed over the volume of the material. The charge distribution associated with the carriers is also evenly distributed but this distribution is temperature dependent, which means that if the temperature of the material is not uniform, the charge distribution will also not be uniform. The accumulation of charge in some parts of the body will cause a reduction of charge carriers in other parts of the material and this will modify the equilibrium of the electric potential in the body. This potential difference caused by the non-uniform temperature distribution in the material is the source of the Seebeck electromotive force.

In a non-isothermal segment of a conducting material, the temperature difference will cause the more energetic carriers to move from the hotter to the colder side, decreasing their kinetic energy whilst they move through the temperature gradient. This movement of charge creates a potential difference E_{pd} between the ends of the conductor. A second potential difference related to the temperature change arises in the material. This potential is induced by the difference in the Fermi energy between the hot and cold side of the conductor. The Fermi energy is a function of temperature, it increases from the hot to the cold side creating a second potential difference E_f [19]. The net emf created by the temperature

gradient imposed to the conductor is then the sum of both contributions

$$\alpha = \frac{\partial E}{\partial T} = \frac{\partial E_{pd}}{\partial T} + \frac{\partial E_f}{\partial T}, \tag{1.11}$$

where $\partial E_{pd}/\partial T$ represents the rate of change of the electric field created by the carrier movement in relation to the temperature and $\partial E_f/\partial T$ is the change rate of the potential created by the difference in Fermi energy along the conductor in relation to temperature. This equation shows that the absolute Seebeck coefficient (Equation 1.4) is the sum of these two effects.

The first contribution to the absolute Seebeck coefficient is induced by the carrier density difference between the hot and cold ends and it is denoted as α_{pd}. The electric field E_{pd} at equilibrium is given in terms of the carriers by

$$ne\mathbf{E}_{pd}\partial x = \partial P, \tag{1.12}$$

in which n is the number of carriers, e is the elementary electron charge and $\partial P/\partial x$ is the rate of change of the "pressure" of the carrier gas along the thermoelement [5]. Using this expression the potential dependence on temperature can be derived [b]

$$\alpha_{pd} = \frac{\partial E_{pd}}{\partial T} = \frac{1}{ne}\frac{\partial P}{\partial T}. \tag{1.13}$$

The second contribution to the potential difference is denoted as α_f and can be expressed in terms of the Fermi energy E_F as

$$\alpha_f = \frac{dE_f}{dT} = -\frac{1}{e}\frac{\partial E_F}{\partial T}, \tag{1.14}$$

where $\partial E_F/\partial T$ represents the change of the Fermi energy in relation to temperature [17].

The net absolute Seebeck coefficient ($\alpha = \alpha_{pd} + \alpha_f$) of the conductor is then expressed as

$$\alpha = \frac{1}{e}\left(\frac{1}{n}\frac{\partial P}{\partial T} - \frac{\partial E_F}{\partial T}\right). \tag{1.15}$$

This is a general expression which is derived taking only into account the effects induced by the movement of the carriers in the material, thus it is valid

[b] Using the chain rule and noting that $\mathbf{E}_{pd} \cdot \partial x = \partial E_{pd}$,

$$ne\mathbf{E}_{pd} = \frac{\partial P}{\partial T} \cdot \frac{\partial T}{\partial x} \Longrightarrow ne\frac{\partial E_{pd}}{\partial T} = \frac{\partial P}{\partial T}$$

Table 1.1: Absolute Seebeck coefficient of electrically conducting materials [5, 8, 12, 16].

Thermoelement	Carriers' energy	Seebeck coefficient
Normal metals	$\langle E\rangle \cong \frac{3}{5}E_F(0)\left[1+\frac{5\pi^2}{12}\left(\frac{k_BT}{E_F(0)}\right)\right]$	$\alpha \cong A\frac{\pi^2}{2}\frac{k_B^2T}{eE_F}$
Transition metals	$\langle E_h\rangle \cong \frac{3}{5}[E_0-E_F(0)]\left\{1+\frac{5\pi^2}{12}\left(\frac{k_BT}{E_0-E_F(0)}\right)\right\}$	$\alpha \cong A'\frac{\pi^2}{6}\frac{k_B^2T}{e(E_0-E_F)}$
Semiconductors	$E_F \cong k_BT\ln\frac{nh^3}{2(2\pi mk_BT)^{3/2}}$	$\alpha \cong \pm\frac{k_B}{e}\left[(2+x)-\frac{\Delta E}{k_BT}\right]$

$\langle E\rangle$: Average carrier energy. E_F: Fermi energy. k_B: Boltzmann constant. α: Seebeck coefficient.
A, A': Parameters to account for the electron model used to derive these equations.
$E_0 - E_F$: Energy range of unfilled portion of the d band.
ΔE: Energy range between the band edge (conduction or valence band) and the Fermi energy.
x: Parameter to differentiate between phonon or impurity scattering.

for any electrical conductor. This equation shows the dependency of the inherent thermoelectric properties of the material on the Fermi energy, which varies from one kind of conductor to another. This gives a point of reference to evaluate and compare the thermoelectric properties of normal metals, transition metals and semiconductors.

Using Equation 1.15 specific expressions for Seebeck coefficient of metals and semiconductors can be derived. This equation is composed of two terms, the first one is a function of the pressure. This pressure is induced on the gas of carriers by the temperature gradient and it can be approximated by the ideal gas equation

$$P \cong \frac{N}{V}k_BT = \frac{2}{3}n\langle E\rangle, \tag{1.16}$$

where N is Avogadro's number, V the volume, k_B the Boltzmann constant, n is the number of carriers per unit volume and $\langle E\rangle$ is their average energy [5]. Substituting this equation and the corresponding expression for the energy of the carriers given in Table 1.1 into Equation 1.15, the equations for the specific Seebeck coefficient of the different conductors can be obtained. Table 1.1 summarises the results of these substitutions; the detailed derivation procedure of these equations can be found elsewhere [5, 8, 12, 16].

The difference between metals, transition metals and semiconductors is due to the specific electrical conduction mechanisms occurring in each material. In the case of normal metals, the conduction is purely by electrons. In transition metals and semiconductors, the positive holes make contributions to the electrical

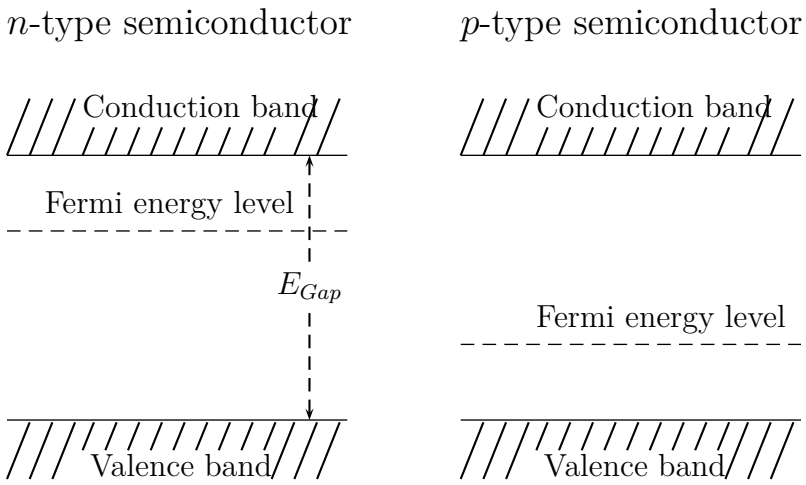

Figure 1.3: Simplified diagram comparing the Fermi levels of an n-type and a p-type semiconductor. For n-type materials the Fermi level is positioned closer to the conduction band. In the case of p-type materials the Fermi level is closer to the valence band [20].

conductivity of the material.

Transition metals are characterised by the incompleteness of their d-bands and by the partially filled outer s-valence levels. The empty states in the d-band can be treated as positive charges or holes. The conductivity of the material can then be described by the behaviour of the positive charges. The energy of the unfilled states measured with reference to the top of the d-band (E_0) is ($E_0 - E_F$). This factor is present in the equations describing the energy of the carries and affects directly the magnitude of the absolute Seebeck coefficient of the material (Table 1.1). A simple analysis of these equations shows why transition metals are preferred in thermoelectric applications over normal metals. The values of ($E_0 - E_F$) for transition elements are very close to 1 eV, which compared to the magnitude of the Fermi energy of a noble metal ($\approx$6 eV) will lead to absolute Seebeck coefficients of transition metals at least twice larger than those of noble metals [8].

In the case of semiconductors, the type of conduction depends on the position of the Fermi level. The closer the Fermi level is to the conduction band, more energy levels of the band are filled causing n-type conduction (Figure 1.3). If the Fermi energy lies close to the valence band, the probability of conduction by positive charges increases, causing a p-type behaviour [20]. Looking at the equation of the absolute Seebeck coefficient for semiconductors, where x takes

values of 1 or 3 depending on the carrier scattering mechanism[c], it is possible to see why semiconductors have much larger Seebeck coefficients than metals. Considering that in semiconductors the energy ratio $\Delta E/k_BT \gg 1$, the absolute Seebeck coefficient of these materials is in the range of mV/K as opposed to µV/K in metals.

A final note on the Seebeck coefficient equation for semiconductors concerns the sign of the carriers. When the semiconductor is an n-type material, the charge of e is negative and so is the Seebeck coefficient. The opposite holds true for p-type semiconductors.

From the previous discussion, it is clear that modifications to the Fermi energy level will have a direct impact on the magnitude of the absolute Seebeck coefficient of transition metals and semiconductors. In transition metals, modifications of the Fermi energy level can result by alloying or impurity inclusions in the material. In semiconductors, the carrier concentration is the main factor affecting the Fermi energy level; modifying the stoichiometry of the particular semiconductor or the addition of impurities will change the carrier concentration [21].

1.3 Thermoelectric materials

In a previous section it was stated that the figure of merit (Equation 1.3) is the parameter that defines the desired properties of thermoelectric materials. According to this figure, a good thermoelectric material not only should posses a large Seebeck coefficient, but also a low thermal conductivity combined with a high electrical conductivity. A low thermal conductivity will avoid heat leakage between the hot and cold side of the thermoelements, maintaining the temperature gradient. A large electrical conductivity implies lower resistivity, which will reduce the heat losses produced by Joule heating. The figure of merit has dimensions of K^{-1}, therefore it is rather quoted as the dimensionless parameter ZT. The enhancement of the thermoelectric properties of a material depends solely on the optimisation of the three parameters determining the figure of merit [22].

The electrical conductivity and the Seebeck coefficient are a function of the Fermi energy level, which in turn is a function of the carrier concentration [23, 24]. The relationship between the Seebeck coefficient, the thermal and electrical conductivity and the carrier concentration is shown schematically in Figure 1.4. The expression $\alpha^2\sigma$ in Equation 1.3, is known as the *power factor*. This quantity

[c] $x \cong 1$ for phonon scattering and $x \cong 3$ for impurity scattering [8].

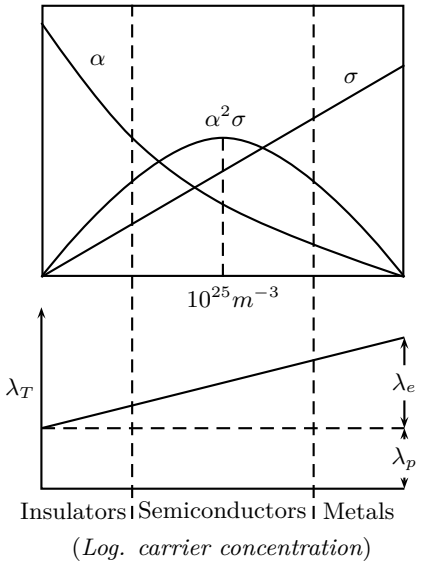

Figure 1.4: Dependence of the electrical conductivity σ, Seebeck coefficient α and thermal conductivity λ on the concentration of carriers. λ_T is the total thermal conductivity which is the algebraic sum of the contributions of the thermal conductivity through carriers λ_e and the thermal conductivity due to phonons interactions λ_p [27].

has importance in itself for thermoelectric applications. Due to the fact that the dependency of the thermal conductivity on the carrier concentration is very weak [25], the effect that an increase in the amount of carriers has on the figure of merit is reflected directly in the power factor. As it can be seen in Figure 1.4, the power factor marks the carrier concentration at which the figure of merit reaches it maximum. The position of this maximum varies with the magnitude of the mass carrier and the type of crystal lattice, but it is usually found in the carrier concentration range of $10^{25}\,\mathrm{m}^{-3}$ to $10^{26}\,\mathrm{m}^{-3}$ [26].

The improvement of the figure of merit through the reduction of the thermal conductivity has to be done without affecting the power factor. It is well known that in metals the thermal conductivity takes place through the carriers (electrons) (λ_e), but in the case of semiconductors, the overall thermal conductivity is the sum of the carrier contributions (λ_e) and the contributions arising from the lattice vibrations or phonons (λ_p) [28]. Research towards the reduction of thermal conductivity has followed various paths focusing mainly on the control of the phonon scattering mechanisms to reduce the thermal lattice contribution [29]. It has been proven theoretically and experimentally that controlling the grain size of materials whilst maintaining the long range periodicity of the lattice results in an effective scattering of the short wavelengths of phonons. Under these modifi-

cations, the longer wavelengths associated with the movement of charge carriers are weakly affected. This process has lead to a certain improvement of the figure of merit [30–33]. Parallel to this approach, the inclusion of defects and impurities in the crystal lattice has been studied as a possible way to reduce the thermal conductivity [34, 35].

Following the previous discussion it is now possible to understand why the most widely used thermoelectric materials are heavily-doped semiconductors. Metals posses intrinsicly low Seebeck coefficients and a large electronic contribution to the thermal conductivity. Insulators and lightly-doped semiconductors have larger Seebeck coefficients, but their very low carrier concentration (Figure 1.4) result in a very low electrical conductivity and consequently a small figure of merit [36].

Despite the intense research towards the improvement of the figure of merit and the fact that it has been shown theoretically that larger values of ZT can be achieved by different methods [22, 37], the maximum values of ZT in established thermoelectric materials has remained close to 1. Thermoelectric materials can be conveniently categorised according to their operation temperature range. Figure 1.5 shows the plot of the figure of merit of the most commonly used thermoelectric materials at different temperatures. Perhaps from all of these synthetic and heavily doped semiconductors, only bismuth and lead telluride alloys can be regraded as established thermoelectrics.

Bismuth alloys in combination with tellurium, selenium or antimony are used in the low temperature range and up to 450 K [39]; therefore these are the materials preferred for thermoelectric refrigeration applications [40, 41]. Materials based on alloys of lead are used up to approximately 850 K and together with silicon germanium alloys, which can operate up to 1300 K, are the preference for thermoelectric power generation [42]. Thermoelectric materials based on bismuth chalcogenides have the highest figures of merit; the best p-type and n-type materials are $Bi_2Te_3-75Sb_2Te_3$ and $Bi_2Te_3-25Bi_2Te_3$ respectively. A thermocouple fabricated from these materials has an average figure of merit of $2.5 \times 10^{-3}\,\mathrm{K}^{-1}$ [43].

Even though thermoelectric generators for commercial applications are mainly fabricated with these established materials, research in the field has produced new materials with improved thermoelectric performance. Higher figures of merit have been achieved by reducing the lattice thermal conductivity in synthetic materials. In this respect, low dimensional structures like quantum wells and quantum

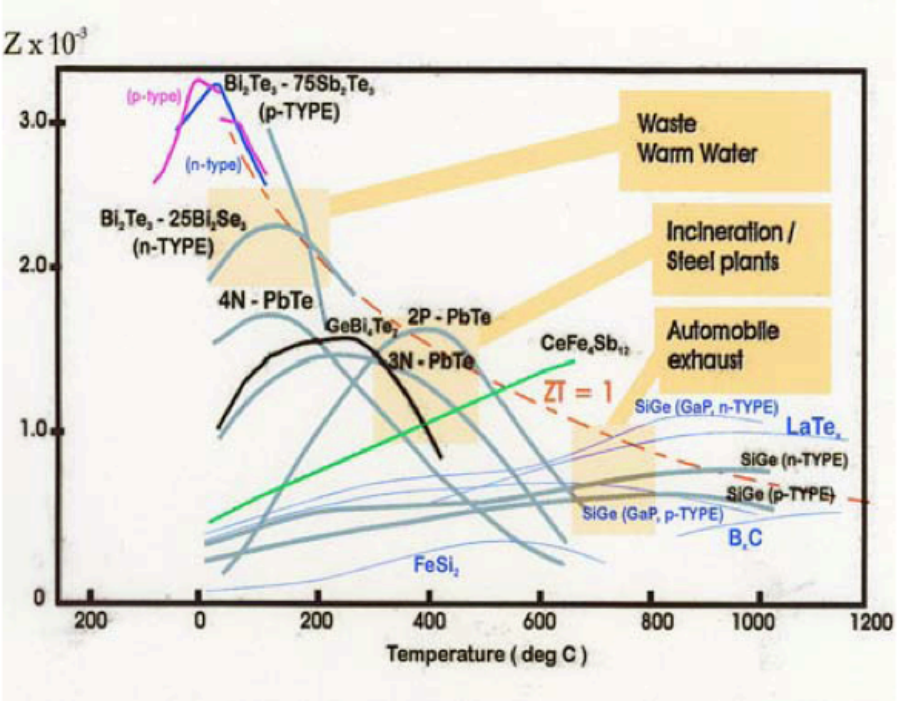

Figure 1.5: Figure of merit of selected materials showing their applications at different temperatures [38].

wires are a very a good alternative for achieving even higher figures of merit. The reduced dimensions of these structures can be used to increase the phonon scattering and thus reduce the lattice thermal conductivity of the material. From all the nanostructured materials, nanowires seem to be the most attractive route for thermoelectric applications. Indeed, the geometry of these materials favours the current flow. They are also more suitable for their integration to microelectronics, which implies more efficient fabrication processes [38].

1.4 Carbon nanotubes as thermoelectric materials

Among the different nanomaterials, due to their electrical and thermal transport properties, bulk samples of aligned carbon nanotubes constitute a promising alternative for thermal management [44]. The intrinsic properties of the constituents of these materials have been widely explored and it has been found that the thermal and electrical conductivity of a single nanotube has a value of $\approx$3000 W m^{-1} K^{-1} and $\approx$10 000 S/m respectively [45]. Regarding the thermoelectric properties of carbon nanotubes, values for the Seebeck coefficient of single

walled have been reported to be between 40 µV/K and 80 µV/K in the case of multiwalled nanotubes [46, 47]. The semiconductor behaviour of carbon nanotubes can be used to manufacture thermoelements with a p-type or n-type behaviour; the type of conduction in the nanotubes can be modified by doping the tubes without affecting the magnitude of the Seebeck coefficient [48].

It is not only the possibility of transferring the thermoelectric properties of carbon nanotubes to macroscopic materials has driven research in this direction. When carbon nanotubes are grown in the form of a bulk conductor, they form junctions between them. This is expected to reduce the thermal conductivity of the bulk material and therefore enhance the value of the Seebeck coefficient.

The thermoelectric properties of arrays of CNTs have been explored by different groups [49–51]. The thermoelectric power of crystalline single walled carbon nanotube ropes has been measured over a large temperature range, finding that the magnitude of the thermopower at room temperature is larger than that of a single nanotube. The reported value of the thermopower ranges from 50 µV/K to 65 µV/K [52]. On the other hand, when mats of single walled and multiwalled CNTs were analysed, they showed a lower value of the Seebeck coefficient (10 µV/K) compared to the one of single tubes. This decrease in the magnitude of the Seebeck coefficient was attributed to the lower amount of carriers present in the array of carbon nanotubes [53].

Another route to achieve larger figures of merit is to incorporate carbon nanotubes in composites. The thermoelectric properties of polymers have been greatly enhanced by embedding CNTs into a matrix formed by the polymer. Unfortunately, the intrinsic thermoelectric properties of the polymers used in those works were very poor, in particular the electrical conductivity [50, 54]. For this reason, the thermoelectric characteristics of the mixed materials are not competitive in comparison to established thermoelements.

In the following section, the development of an experimental set-up to measure the Seebeck coefficient of films is described. The optimal operational parameters of this set-up are discussed through the measurement of the Seebeck coefficient of a reference material. Then, the Seebeck coefficient of carbon nanotube films is measured at different temperatures. Following the characterisation of the materials, their thermoelectric application is demonstrated by the fabrication of a CNT-based thermoelectric generator.

2

Thermoelectric films

The evaluation of any potential thermoelectric material requires the measurement of its transport properties. These include the Seebeck coefficient, electrical and thermal conductivity. The measurement of the Seebeck coefficient can be made by relating the generated voltage across the material when it is subjected to a temperature gradient (ΔT). Despite the apparent simplicity of the measurement there is still no standardised technique to evaluate this property. This has led to a debate regarding which of the available techniques provides the most accurate measurement of the Seebeck coefficient [55–57].

The different methods developed to measure this coefficient can be categorised into differential or integral techniques. In the integral technique one side of the sample is maintained at a constant temperature while the temperature of the other side is increased through the temperature range of interest. This method is sometimes also referred as the large ΔT or the slope method. These names come from the fact that large temperature differences are imposed between the two sides of the samples during the measurement and because the Seebeck coefficient is obtained as the slope of the curve voltage against temperature difference [57, 58].

In the differential technique, the sample is placed at a temperature of interest. Then a small temperature difference ΔT is applied between the ends of the sample and the Seebeck coefficient is calculated as the instantaneous ratio of the

electrical potential and the temperature difference [56]. This method requires a synchronous measurement of the electric potential and the temperature at both ends of the sample. The temperature gradient should be appropriately selected to reduce heat losses associated to radiation of the sample whilst maintaining the accuracy of the method. Typical ΔT values will range between 4 K to 20 K [57, 59].

An advantage of the integral method over the differential is that due to the large temperature gradient applied to the sample, large output voltages are generated. This helps to minimise the effect of parasitic voltages arising from the hardware used in the measurement. The main drawback of this method is the difficulty of maintaining a constant temperature in one side of the sample when a large ΔT is applied. This normally requires corrections to the data which can complicate the measurement. For this reason this method is considered more appropriate for bulk or large samples [55].

Differential techniques can be divided into steady-state, quasi-steady-state or transient conditions. In steady-state conditions the temperature gradient is stabilised prior to each voltage (V) measurement. As the temperature gradient is slowly increased several data points are collected. The Seebeck coefficient is calculated from the linear fit of the ratio $V/\Delta T$ generated at the measurement points. Using this method it is possible to quantify and eliminate spurious voltages generated by the measurement equipment. This offset voltage will be represented as a shift in the curve V vs ΔT [59–62].

Under the quasi-steady-state regime, the voltage measurements are made continuously as the temperature gradient applied to the sample is slowly increased. This decreases the amount of time required per measurement as it is not necessary to wait for the temperature gradient to stabilise. The method relies on measuring multiple instantaneous $V/\Delta T$ ratios which requires a simultaneous measurement of the electric potential and the temperature with nano volts precision [63–66]. It has been found that the results obtained with both methods are equally accurate when good electrical and thermal contacts are ensured between the sample and the measuring probes [56].

The AC method was developed to avoid the thermal stability requirement imposed by the steady-state methods. In the AC method a small sinusoidal temperature gradient between 10 mK and 500 mK is applied to the sample. Using a lock-in amplifier capable of detecting very small signals, the amplitude of the voltage and temperature signals is continuously detected. This method is very

sensitive to the geometry and morphology of the sample. It requires modulation of the temperature signal and specific thermocouple positioning according to the characteristics of each sample. The sensitivity of this method to very small changes in the temperature and voltage signals makes it suitable for measurements at critical points where rapid measurements are necessary [55, 67].

Regarding the design of the electric contacts between the measuring apparatus and the sample there are two type of configurations, they are known as the 2-probe and the 4-probe techniques. In the methods categorised as 2-probe, the measurements of voltage and temperature difference are made at the ends of the sample. In the 4-probe method, the two additional probes are place in contact with the sample at an off-axis position. These extra contacts allow for the simultaneous measurement of the Seebeck coefficient and the resistivity of the material. Although this is considered as an advantage over the 2-probe technique, it has been shown that the 4-probe tends to overestimate the value of the Seebeck coefficient. This has been attributed to what is known as the cold finger effect, caused by a temperature gradient formed between the two extra contacts and the sample. This gradient results in an underestimation of the sample's temperature and therefore a higher value of the Seebeck coefficient [56, 64].

There are a some commercial systems available for the measurement of the Seebeck coefficient. ULVAC technologies, Ozawa science, LINSEIS and MMR technologies are amongst the companies that produce this type of equipment. Most of their systems use the steady-state method and are designed mainly to test bulk samples. The evaluation of the Seebeck coefficient of films has been made using custom-made equipment [68, 69]. In this work, films made from CNTs will be used to fabricate thermoelectric devices. This chapter will focus on the development of a set-up to characterise the Seebeck coefficient of films using a 2-probe steady-state differential method.

2.1 Experimental set-up

To characterise the Seebeck coefficient of carbon nanotube films, it is necessary to measure the voltage the film generates when a temperature gradient is created between the ends of the sample. The calculation of the Seebeck coefficient is then made by relating the generated voltage to the magnitude of the temperature gradient. The experimental set-up developed for this purpose consists of a sample stage holder, a temperature feedback circuit, a heater controller circuit

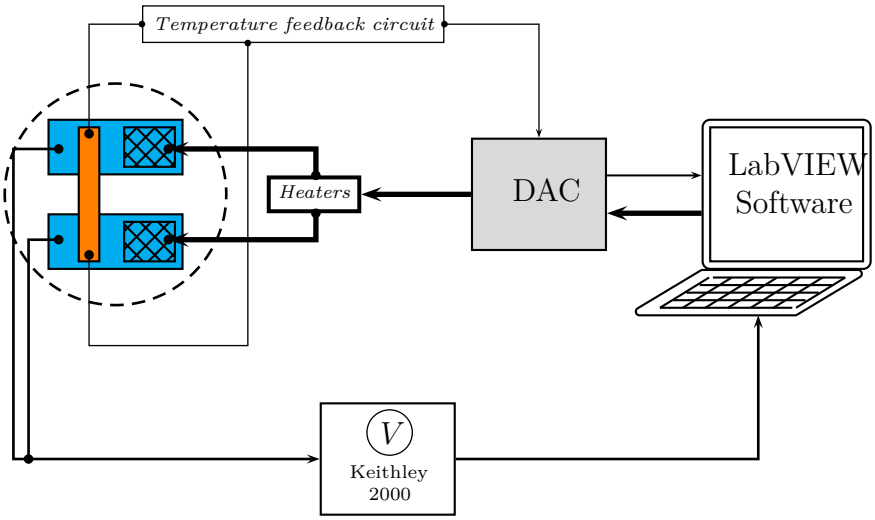

Figure 2.1: Diagram of the experimental set-up to measure the Seebeck coefficient of films. The dashed circle encloses the stage holder where the sample (orange) is positioned.

and a voltage measurement device. All these components are connected through a software written LabVIEW which processes the input signal and produces an output signal that controls the temperature of the sample.

A diagram of the set-up is shown in Figure 2.1. The dashed circle encloses the stage holder, where the heaters and the temperature sensors are located. The thermistors provide the necessary information to measure the temperature at both ends of the sample. These readings are acquired by a Data Acquisition Card (DAC) model NI PCI-6052E, which transfers the readings to the LabVIEW software. After the software processes the temperature information, it sends a signal back to the DAC, which also controls the power supplied to the heaters, i.e. creating a closed feedback circuit.

The stage holder is enclosed in a chamber and is formed by two S102C 120 Ω precision heaters used to increase the temperature at the ends of the sample up to 150 °C. The temperature of each heater is manipulated independently by controlling the amount of current supplied. The temperature of the heaters and the sample is monitored by two PT1000 class A thermistors placed on top of each heater between the sample and the heater, as shown in Figure 2.3. The working range of these temperature sensors is −200 °C to 600 °C and they have a tolerance of ±0.15 °C to ±0.95 °C depending on the operating temperature. The distance between the two heaters is fixed at 40 mm.

The temperature feedback circuit comprises two temperature sensors and two 10 kΩ resistors. The readings acquired by the analogue input of the DAC are

voltages that relate to the heater's temperature. Two analogue inputs of the DAC are used to get the signal from the temperature feedback circuit. The LabVIEW software converts the input voltage readings into temperature readings using the thermistor resistance equation $R(T)$ provided by the manufacturer.

The connection between the software output signals and the heater controller circuit is made through the DAC analogue outputs. These are connected to the heater circuit, which is formed by a transistor-based electronic circuit and a power supply that controls the amount of current supplied to the heaters. The temperature dependency on the current supplied to the heater is controlled internally by a proportional-integral-derivative controller (PID controller). A 24 V power supply is used in this set-up to deliver the necessary current to increase the temperature of the heaters.

The potential difference between the ends of the sample is measured using a Keithley 2000 nanovoltmeter. The readings of this device are sent to the LabVIEW software using a general purpose interface bus (GPIB) adaptor which is an 8-bit parallel interface bus used for short-range digital communications.

The LabVIEW software was designed to acquire and analyse the temperature data and based on that deliver current to the heater's circuit. This is regulated by the experimental parameters, which are set through the software interface (Figure 2.2). The software permits the independent control of each heater, in the right side of the panel of the software interface, the temperature of each heater can be set to a specific value. This value can remain constant or increase automatically according to the kind of experiment being performed. If the temperature gradient is kept constant during the experiment, both sides are heated; but if the temperature difference is set to increase, only one side of the sample is heated. All the data generated during an experimental run is displayed and recorded at the same time.

To perform an experimental run, the value of the initial and final temperature of each heater and the magnitude of the temperature ramp are set through the program. The magnitude of the temperature gradient is set by specifying different initial temperatures for each heater. Once these values have been set, the software monitors the temperature sensor readings and waits until the temperature at each end of the sample reaches its corresponding value. This is achieved when the temperature remains for 15 s at the set temperature $\pm 0.1\,^{\circ}\mathrm{C}$. At this point the software applies the temperature ramp and the temperature in the heaters is modified. This cycle is repeated until the final temperature is achieved.

Figure 2.2: LabVIEW software screen showing the control of the experimental parameters. The plot shows the temperature on each side of the sample during the experimental run. The bottom left panel shows the readings of the instantaneous Seebeck coefficient and Temperature difference between the two ends of the sample. The right panel contains the temperature controls for both ends of the sample.

To calculate the Seebeck coefficient, the program measures the voltage generated between the ends of the sample and divides it by the temperature difference between the ends (Equation 1.5). Since the voltage is measured using copper cables, a junction is generated between the sample and the copper wire. Therefore, the measured Seebeck coefficient is the relative coefficient of the sample and copper. Taking this into account, the absolute value of the coefficient can be calculated from

$$\alpha_x = \alpha_{Cu-x} - \alpha_{Cu}, \tag{2.1}$$

where α_x is the absolute Seebeck coefficient of the sample, α_{Cu-x} is the measured coefficient and α_{Cu} is the Seebeck coefficient of copper. Considering that the value of the absolute Seebeck coefficient of copper is $\approx$1.8 µV/K for the temperature range where the sample is analysed [70, 71], the absolute value of the Seebeck coefficient of the sample during the experimental run is calculated by $\alpha_x = \alpha_{Cu-x} - 1.8$ in (µV/K).

2.2 Constantan films

Constantan is a group of alloys of copper and nickel. The name derives from the fact that the electrical resistivity of these alloys remains constant at different temperature ranges [72]. Copper is soluble in nickel in both the liquid and the solid state. At all proportions they form alloys with homogeneous structures which gives place to several nickel - copper alloys. Although in the case of constantan the nominal composition is 45 % of copper and 55 % of nickel (45Cu-55Ni), specific compositions can vary from 50Cu-50Ni up to 65Cu-35Ni [73]. The properties of constantan vary accordingly to the composition of the alloy. The electrical resistivity of constantan increases as the nickel content of the alloy increases until it reaches a maximum of about 50 µΩ cm, the highest of any of the nickel-copper alloys [74]. The electromotive force of constantan is negative with respect to platinum (usually a reference standard for the Seebeck coefficient) and its magnitude reaches a maximum of approximately $-35\,\mu V/K$ at room temperature for the 45Cu-55Ni composition [75]. For the different compositions of this alloy, the value of the emf is directly proportional to the nickel content, increasing its magnitude in a linear manner with the increase of temperature [73]. Having the highest emf of any of the copper-nickel alloys constantan is widely used in temperature measurement systems.

The calibration of the experimental set-up was made using films of constantan 45Cu-55Ni. To ensure all the samples had the same dimensions (40 mm × 5 mm), they were cut from a 0.050 mm thick constantan foil using a programmed laser cutter. The samples were placed in the stage holder as shown in Figure 2.3. The ends of the sample were fixed to the heaters and the temperature sensors using silver paint. The thermal and electrical contacts provided by the silver paint have been tested against other compounds and it was found that silver paint provides a thermal and electrical transfer as good as other varnishes, having the advantage of being soluble in acetone. This makes it easy to remove the sample from the stage holder [76]. All the experimental runs were carried out connecting the samples in the same way.

In the first calibration experiment, one side of the sample was heated from ≈300 K to 420 K in steps of 1 K while the other side was left unheated. During the experimental run, the temperature of both sides was monitored. It was shown that the temperature of the colder side did not remain constant. By the end of the experiment it had increased almost by 10 K, Figure 2.4.b. Examination of

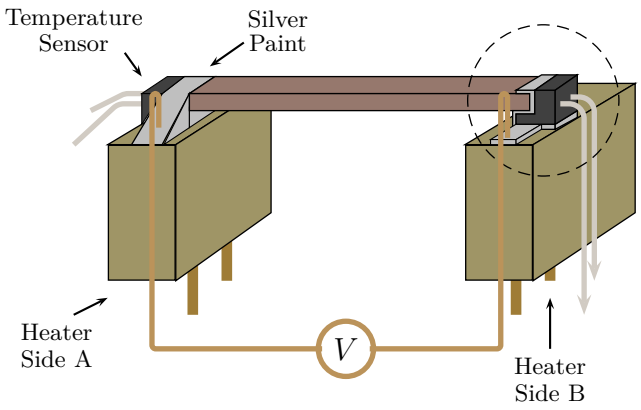

Figure 2.3: Holder scheme. The dashed circle encloses the cross sectional area of the junction. It shows the type of thermal and electrical contact used to measure the Seebeck coefficient of every sample.

the temperature plots of both sides of the sample and the temperature of the air inside the chamber shows that the increase in temperature might be caused by hot air flowing from the hot to the cold side of the sample. Taking this into account, the values of the absolute Seebeck coefficient against the temperature difference between the sample ends are shown in Figure 2.4.a. To ensure the set-up configuration was the correct one, the same sample was tested again heating the opposite side this time. The results, as expected, are the same regardless of which side is being heated as it can be seen in Figure 2.4.a.

The plot of the Seebeck coefficient in Figure 2.4 shows the value obtained when different temperature gradients are applied to the sample, it does not represent the value of the coefficient at different temperatures. The value of the Seebeck coefficient (α) was obtained dividing the voltage generated between the ends of the sample by the temperature difference. Therefore, the increase in the magnitude of the coefficient is clearly related to the increase in the voltage created by the temperature gradient.

The results of the experiment also show that for small temperature differences the values of the Seebeck coefficient show a larger variation compared to the measurements done using larger temperature gradients. This could imply that the measurements are more accurate when larger temperature gradients are used. On the other hand, as discussed previously, the Seebeck coefficient can only be approximated by Equation 1.5 if small temperature gradients are taken into account. To determine the value of the Seebeck coefficient at different temperatures and the optimum temperature gradient that should be used during the

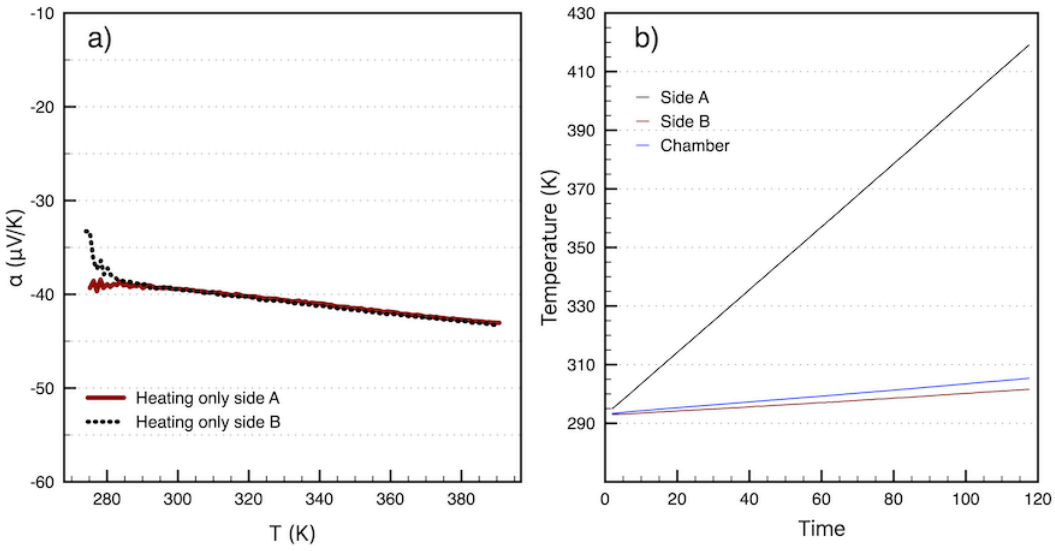

Figure 2.4: a. Magnitude of the absolute Seebeck coefficient (α) of constantan at different temperatures. **b.** Temperature inside the chamber and temperature at the end A and B of the sample.

measurements, a second experimental run was carried out.

In this second set of experiments, a fixed temperature difference was created between the ends of the sample. This time, the temperature on both sides was increased by 1 K between each calculation, keeping a constant temperature gradient through the sample. Similarly to the first calibration experiments, the temperature range spans from ≈300 K to 420 K. The samples were exposed to three different temperature gradients of magnitude 5 K, 7.5 K and 10 K. The results of the experiments are shown in Figure 2.5.

The green line in the Figure 2.5 is a parametric fit of the Seebeck coefficient of constantan in terms of the temperature. The model was developed by Lowhorn et al. using the data measured by eight different laboratories [77]. The equation of the model is

$$\alpha(T) = -1.076 + 0.5294\log(T+1) - 2.22\sqrt{T} - 1.160\sin(2\pi T/700) + 3.248\cos(2\pi T/700), \quad (2.2)$$

where $\alpha(T)$ is the Seebeck coefficient of constantan as a function of the temperature (T). The standard deviation of this model is $\sigma = 3.3$, which represents a variation of 3.3 μV/K between the values provided by the different laboratories. A direct comparison of the results obtained and the predictions of the model show that using temperature gradients of 7.5 K and 10 K result in measurements that

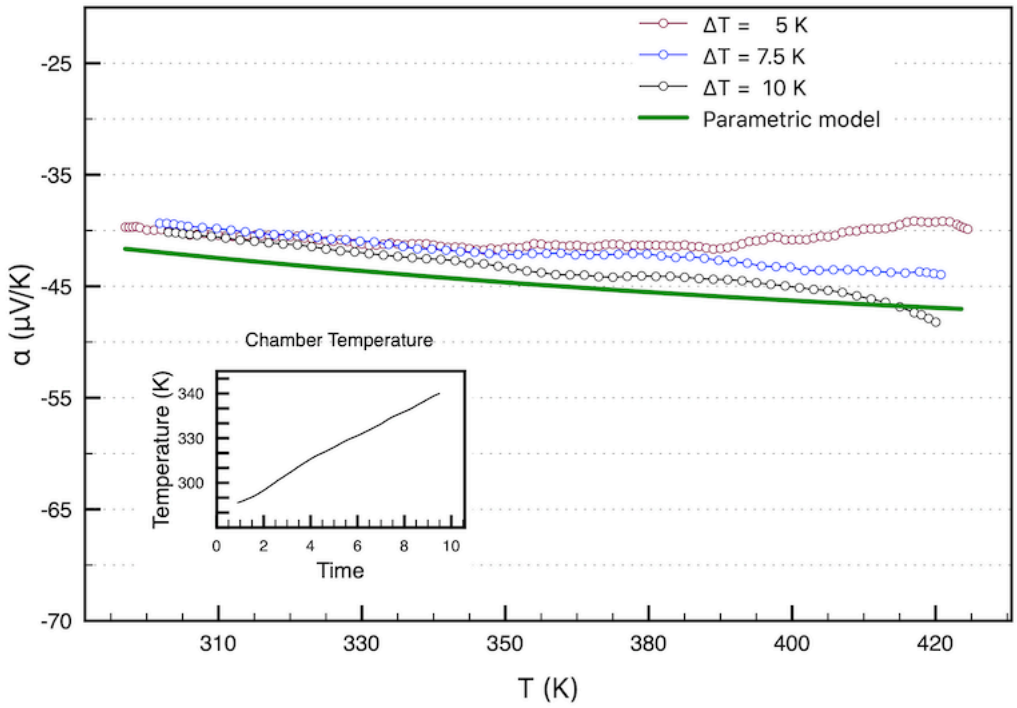

Figure 2.5: Measured absolute Seebeck coefficient of constantan at different temperatures. (Inset) Temperature inside the chamber during the experimental run. The green line is a parametric model fit of the Seebeck coefficient of constantan. The model was prepared by Lowhorn et al. from the experimental data of eight different laboratories [77].

fall within the standard deviation of the model.

When a temperature difference of 5 K was set, the value of the coefficient in the temperature range remains almost constant compared to the results obtained when 7.5 K and 10 K temperature differences were applied. An increase in the magnitude of the Seebeck coefficient of constantan at this temperature range has previously been reported [75, 78]. Thus, according to the results of the experiment, applying temperature differences of 7.5 K and 10 K give more similar results to the ones reported in the literature. Another comparison between the values obtained for Seebeck coefficient of constantan and the reported ones for this temperature range is shown in Table 2.1.

An analysis of the values in Table 2.1, it is clear that the calculations using 5 K difference should be discarded. Not only they are the farthest in magnitude to the known coefficient of constantan, but also, as previously seen in Figure 2.4.a, the smaller the temperature difference used, the higher the variation in the results obtained. Also, the values measured using this temperature gradient do not show the temperature dependency of the coefficient. In the case of 7.5 K and 10 K

Table 2.1: Comparison between the reported and measured values of the absolute Seebeck coefficient of 45Cu-55Ni alloy

Temperature	α (µV/K)	α (µV/K)		
K	Ahmad [75]	Δ T = 10 K	Δ T = 7.5 K	Δ T = 5 K
320	-42.0	-40.1	-39.9	-40.3
350	-45.5	-42.1	-40.8	-40.8
370	-46.0	-43.6	-41.5	-41.4
400	-48.5	-44.6	-43.1	-41.9
420	-50.0	-47.2	-44.2	-40.0

difference, it appears that using a higher temperature gradient leads to more similar values to the reported ones. Also the calculated coefficient shows the characteristic temperature dependency for this temperature range. It is possible that even higher temperature gradients could result in closer values to those reported by Ahmad [75], but again, this method assumes a small temperature difference for the calculations, therefore using higher temperature gradients will violate this assumption.

One possible cause of the variation between the values of the coefficient obtained for constantan and the established ones arises from the limitations of the experimental set-up. Looking at the inset in Figure 2.5, it is possible to see that the temperature of the chamber only reaches ≈340 K. This means that the samples have not been exposed to higher temperatures than this. The temperature gradient is created with high temperatures, but the actual temperature at which the measurement is performed is the temperature of the chamber. Despite the fact that the results obtained with this experimental set-up present a small variation compared to the values of the absolute Seebeck coefficient of constantan, they are a very good approximation. The sign of the coefficient is consistent, also the order of magnitude and the temperature dependency. Therefore, under the performance conditions described, the set-up can be used to obtain a good approximation of the actual values of films.

2.3 Carbon Nanotube Films

The carbon nanotube films used in this work were produced using a spinning method whereby the films are withdrawn directly from the reaction zone of a furnace [79]. The synthesis method uses methane as the main carbon source, thiophene as a source of sulphur and ferrocene as a precursor of iron catalyst particles. The precursors are evaporated and taken into the system through a hydrogen gas stream. The feedstock is then moved to the hot zone of the furnace, which is at approximately 1560 K. Once it reaches this point, the precursor molecules dissociate and the carbon atoms start diffusing to the catalyst particles where they nucleate forming the carbon nanotubes. This process forms an aerogel which condenses into a stock-like-structure of bundled carbon nanotubes as it reaches the colder outlet of the furnace. At this point, a fibre can be collected using a spinning rod or winder which collects 20 m of fibre per min. The continuous spin of this fibre forms the film of carbon nanotubes [80].

The films obtained using this method contain mainly multi-walled and single-walled carbon nanotubes, but also some other particles like amorphous carbon and impurities. The mechanical and transport properties of this material are defined by its composition and structure. These factors are dependent on the processing conditions, i.e. the spinning rate, temperature of the furnace, the carrier gas flow rate [81]. The alignment of the nanotube bundles within the film, the amount of voids present in the material and the length of the nanotubes are also factors affecting the material properties. Longer and well aligned nanotubes can promote the transfer of the axial properties between them. Lower amount of impurities and surface defects will enhance the transport properties of the material [82].

The carbon nanotube film is composed of approximately 70 % CNT-based material, 10 % absorbed species (hydrocarbon from the reaction chamber) and 20 % of residues from the catalysis (Fe) and amorphous carbon. The fibre is mainly formed by carbon nanotube bundles with diameters ranging from 20 to 60 nm, with a high proportion of double-walled nanotubes and a lower amount of single and multi-walled carbon nanotubes [83, 84].

The same method used to position the constantan samples in the experimental set-up is applied in the characterisation of the CNT films. Silver paint is applied to create an electrical and thermal contact at the ends of the sample. For this reason, an analysis of the effect silver paint has on the structure of the CNT film

was performed.

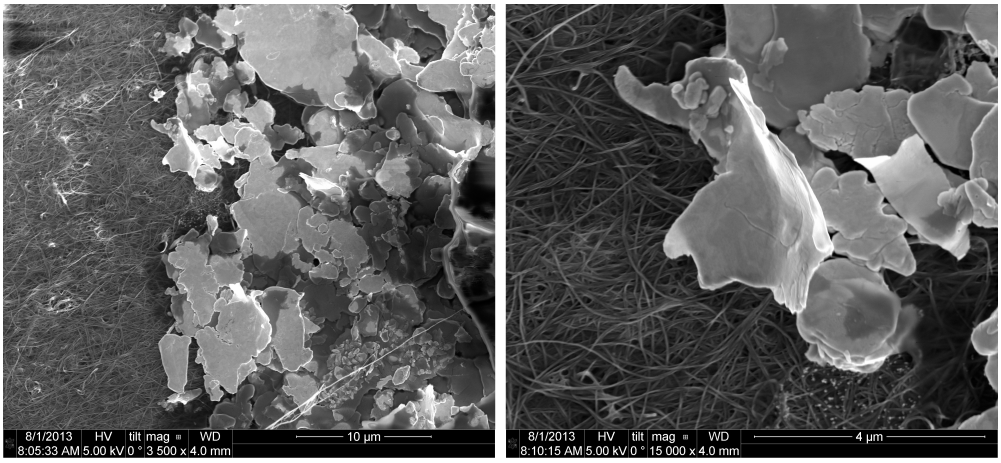

Figure 2.6: SEM image of the carbon nanotube film covered by a layer of silver paint. The image in the right shows a magnification of the silver particles.

A layer of silver paint was deposited on the carbon nanotube film and scanning electron microscope (SEM) images were taken using the SEM station of a FEI Helios Nanolab microscope. Figure 2.6 shows the boundary of the silver paint layer on top of the carbon nanotube film. The image on the right is a magnification of the silver particles. It is evident that they are bigger than the space between the bundles, which stops the silver from penetrating the carbon nanotube film.

To reveal the transverse section of the CNT film in the section where the layer of silver paint was located, a vertical cut in the sample was performed using the focused ion beam (FIB) stage of the Helios Nanolab. The SEM images in Figure 2.7 provide the confirmation that silver paint does not diffuse through the bundles, it stacks on top of them forming a layer much thicker that the CNT film. Using the magnification in Figure 2.7, an approximate value for the thickness of the CNT film can be calculated. The image was taken tilting the stage at 52°, which is the angle between the FIB and SEM columns. The observed thickness is divided by tan(52°) to obtain the actual thickness of the CNT film, which is estimated to be $\approx 1.3\,\mu m$[a].

The characterisation of the absolute Seebeck coefficient of the CNT films was performed on samples with dimensions of $40\,mm \times 5\,mm$. As in the case of constantan, to keep the dimensions as similar as possible between the analysed

[a]This value is just a reference. The thickness of the film depends on several factors associated to the synthesis process (spinning time, size of the spinning rod, winding speed, etc.), it is thus expected to have different magnitudes in different sections of the sample. A proper calculation would consider an average of the thickness in several regions.

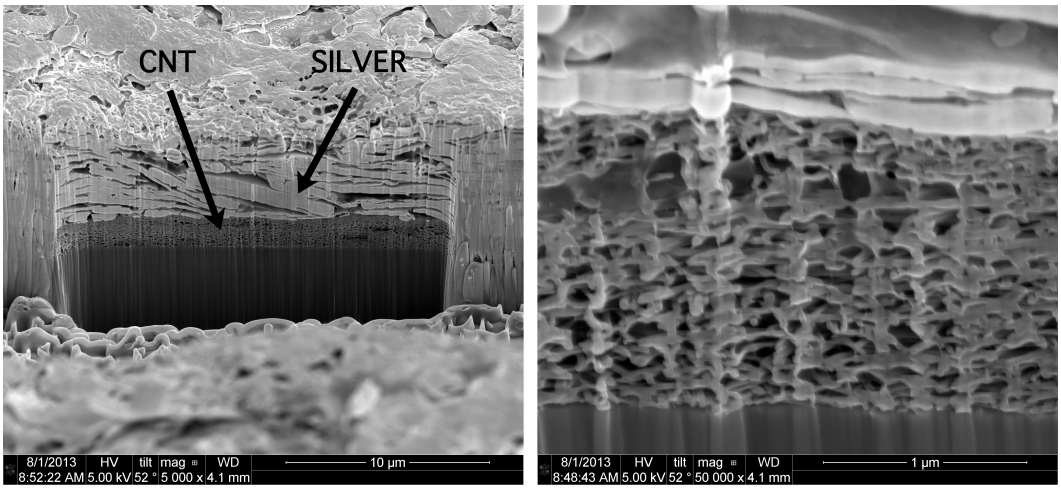

Figure 2.7: SEM image of the transversal section of the CNT film - silver paint system. The magnification shows the thickness of the CNT film.

samples, the films were cut using a programmed laser cutter. The samples were obtained from five different batches, which means the films were synthesised in five different furnace runs.

All the samples were produced using the same experimental parameters. The temperature of the furnace was set to 1550 K. Methane, the carbon source, was introduced into the reaction zone at $80\,\mathrm{mL\,min^{-1}}$. Thiophene was injected at a rate of $1.3\,\mathrm{mg\,min^{-1}}$ and ferrocene at $0.35\,\mathrm{mg\,min^{-1}}$. The flow of hydrogen was set to $0.8\,\mathrm{L\,min^{-1}}$.

The calculation of the Seebeck coefficient was carried out in a temperature range of ≈300 K to 370 K in samples from the five batches. The experimental parameters defined in the previous section were used during the experimental runs. A temperature gradient of 10 K was imposed between the ends of the samples and a temperature ramp of 2 K per measurement was used.

Figure 2.8 shows the results of these experiments. The values of the Seebeck coefficient of the CNT films at ≈300 K lies within the range of 45 µV/K to 60 µV/K. Since the samples originate from different batches, one can expect to find slightly different properties between them. For example, the measured resistance of the samples can vary from 10 Ω to 40 Ω. Despite these differences, the Seebeck coefficient of all samples is positive and has the same order of magnitude. Also, it can be observed in the plot, that the coefficient of all samples presents the same temperature dependency. As the temperature increases, the magnitude of the coefficient increases as well.

The CNT films normally contain a mixture of metallic and semiconducting

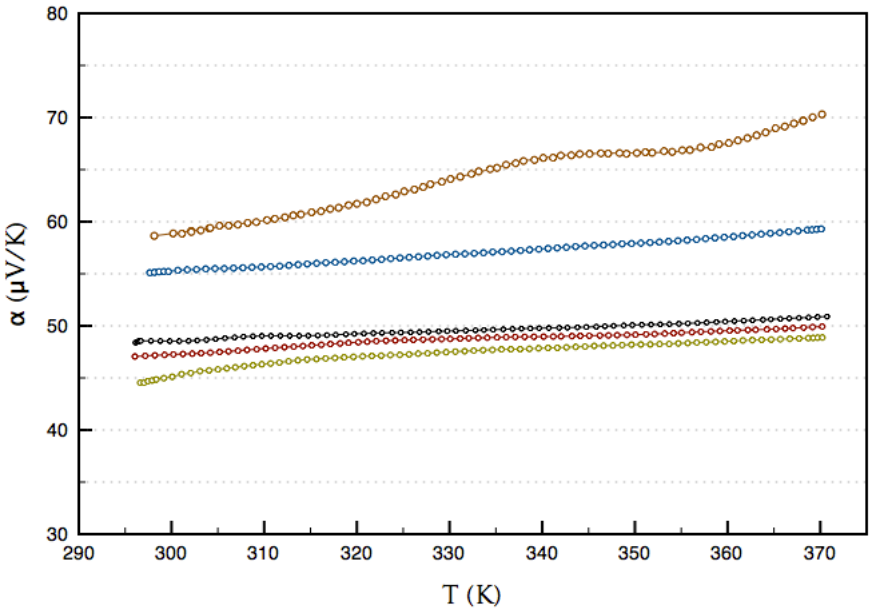

Figure 2.8: Seebeck coefficient of five carbon nanotube films produced using the floating catalyst spinning method. The synthesis parameters of the five samples were the same. The synthesis was carried out at 1550 K and the ratio of the precursors was constant for all the samples. Methane was used as the carbon source, thiophene as the sulphur source and ferrocene as source of the catalyst particles.

nanotubes, with the semiconducting tubes predominating in the film. The ratio of species in this material is 2/3 of semiconducting tubes to 1/3 of metallic tubes [85]. This is consistent with the measured positive value of the absolute Seebeck coefficient of the sample. It was discussed in Section 1.2 that a positive value implies the conduction is done mainly through positive carriers.

It is known that lower thermal conductivities lead to a larger figures of merit, which is desirable in order to achieve higher efficiencies in thermoelectric devices. Parting from the fact that the thermal conductivity of aligned carbon nanotubes is up to ten times higher when it is measured parallel to the direction of alignment, than when measured perpendicularly to the same direction [86], an experimental run to evaluate the effect of the alignment of the tubes on the magnitude of the Seebeck coefficient was performed on samples from the batch which showed the largest Seebeck coefficient in the previous experiments.

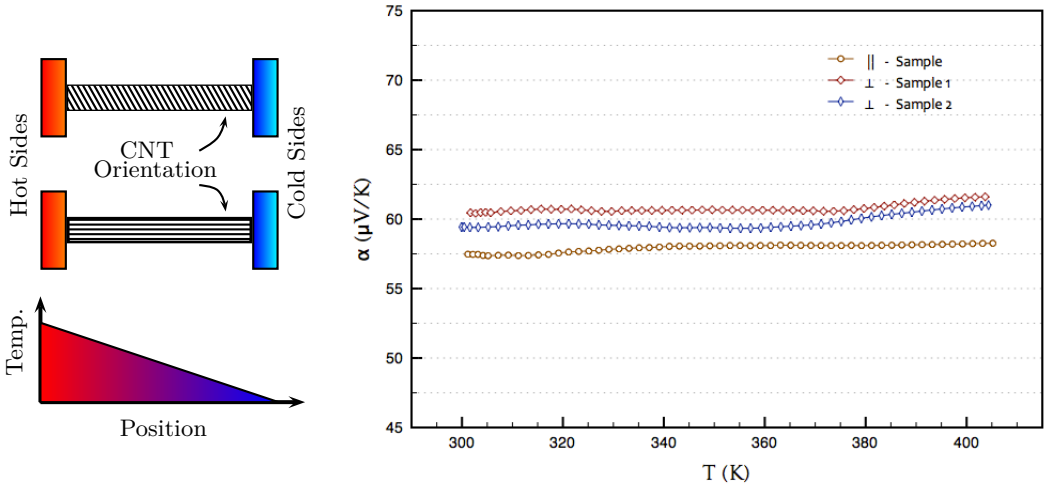

Figure 2.9: Seebeck coefficient of carbon nanotubes films of samples with the tubes aligned parallel and perpendicularly to the longitudinal axis of the sample.

Carbon nanotube bundles in the film are mostly aligned parallel to the spinning direction. Taking this into account it is possible to prepare samples where the tubes are mainly oriented parallel or perpendicularly to the longitudinal axis of the sample. In the left side of Figure 2.9 a schematic diagram of the orientation of the tubes and the positioning of the samples in the set-up is shown. The Seebeck coefficient of these samples was evaluated from ≈300 K to 400 K. The same experimental parameters as used for the characterisation of the previous samples were used in this experimental run.

Figure 2.9 shows the results of these experiments. Since the value of the Seebeck coefficient varies between samples, it is not possible to assess from these results if the observed increase in the magnitude of the coefficient of the samples composed by perpendicularly oriented nanotubes is related to the alignment of the tubes or if it is just a results of the intrinsic differences between samples.

Regarding the thermal conductivity, is worth pointing out that despite the fact that overall the tubes are aligned in the spinning direction, they form entanglements. These entanglements (see Figure 2.6 and Figure 2.7) are itself a barrier to the movement of phonons, which decreases the overall thermal conductivity of the material. Therefore, a deeper analysis which includes measurements of thermal conductivity in both directions will be necessary to investigate the effect of the tubes alignment on this transport property of the sample.

Based on these results, it is already possible to establish a first comparison between the thermoelectric properties of the CNT films and some established thermoelectric materials. The CNT films may be regarded as a low-temperature

range material and the magnitude of their Seebeck coefficient puts them in an intermediate range, one order of magnitude higher than the Seebeck coefficient of any normal metal and one third of the magnitude of the coefficient found in heavily doped semiconductors. But the thermoelectric properties of the CNT films become more attractive when they are associated to some advantages they have over other materials, such as their extremely low weight, flexibility and strength.

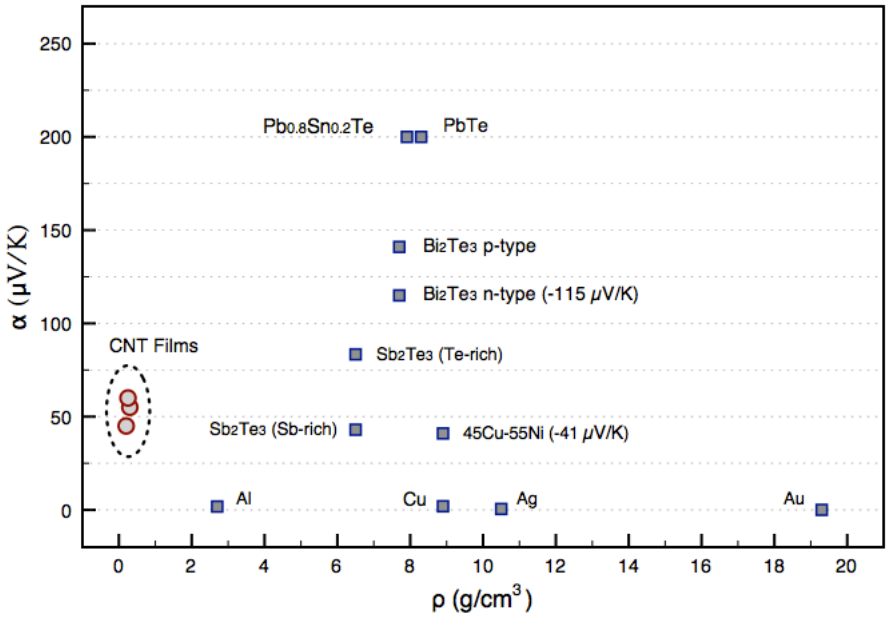

Figure 2.10: Plot of the absolute value of the Seebeck coefficient against density for different semiconductors and metals. Sources: Bi_2Te_3 [87, 88], Sb_2Te_3 [12, 89], $PbTe$ [90], $Pb_{0.8}Sn_{0.2}Te$ [91], Al [92], Au and Ag [93].

In Figure 2.10 the thermoelectric properties of several materials and carbon nanotube films are compared by plotting their Seebeck coefficient against their density. Clearly the CNT films are the least dense material ($\approx 0.12\,\mathrm{g/cm^3}$)[b], at least one order of magnitude below aluminium. In terms of the Seebeck coefficient, they are comparable to constantan and to antimony telluride, but again, these materials are far heavier.

The importance of the lightness of the CNT film rests in the potential applications of this material as an element in thermoelectric generators, where the output power increases linearly with the number or thermoelements connected. Industries such as aerospace and transport, where weight is a very important design factor, could greatly benefit from the energy harvested by extremely light

[b] A previous measurements reported a value of $0.05\,\mathrm{g/cm^3}$ for the same material [94].

weight thermoelectrics.

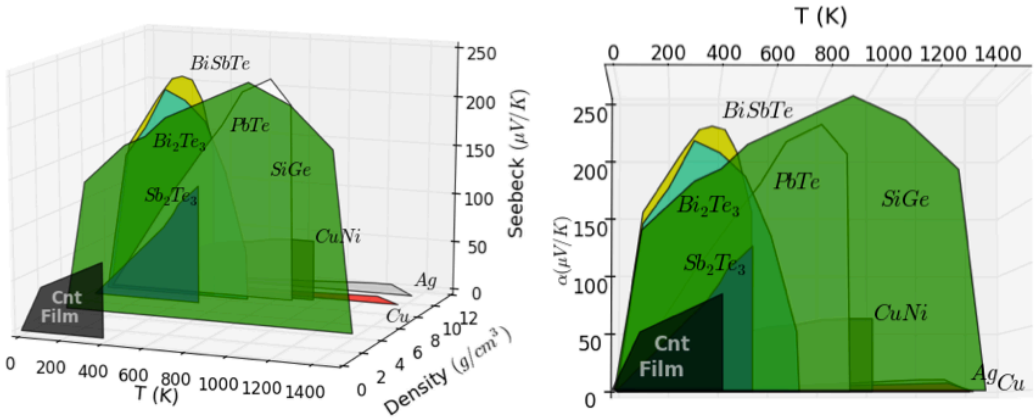

Figure 2.11: (Left) 3D-Plot showing the Seebeck coefficient of TE materials at different temperatures. (Right) Front view of the same plot.

As previously discussed, the thermoelectric characteristics of any material are temperature dependent. This leads to a specific performance according to the temperature range of operation. In Figure 2.11 the value of the Seebeck coefficient at different temperatures are shown. Due to the fact that density also has some variations with temperature, the plotted value should be taken only as a reference. CNT films are in the low temperature range together with bismuth and antimony alloys of telluride. The medium temperature range is dominated by lead telluride and the alloy of silicon germanium, which has a large temperature operation up to 1400 K.

In Section 1.3, the power factor was defined as the product of the square of the Seebeck coefficient and the electrical conductivity ($\alpha^2\sigma$), it was discussed that enhancement of this factor is reflected in the figure of merit. The power factor is a measure of the efficiency of a thermoelement and it is commonly expressed in $\mu W\,cm^{-1}\,K^{-2}$.

Figure 2.12 plots the power factor of several thermoelectric materials through the different temperature regions were thermoelectric elements find application. The maximum of the curve corresponding to each material shows the temperature at which the thermoelement has its best performance.

The plot in Figure 2.12 clearly illustrates that a large Seebeck coefficient is not the only requirement for a good thermoelement. As seen in Figure 2.11, the magnitude of the Seebeck coefficient of the CNT film is smaller than any of the telluride alloys. Analysing the power factor in the low temperature region, however it can be observed that the CNT-based material has a better performance

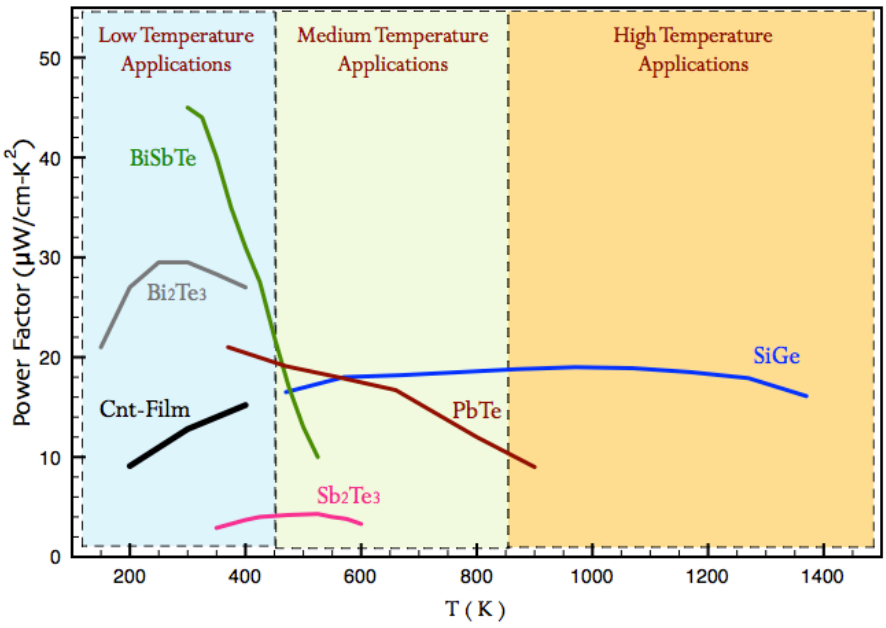

Figure 2.12: Power Factor of TE materials at different temperatures. Sources: $BiSbTe$ [95], Bi_2Te_3 [87, 88], Sb_2Te_3 [12, 89], $PbTe$ [90], $SiGe$ [22, 96].

than antimony telluride.

One of the principal advantages of building thermoelectric devices with CNT films as thermoelements is the very low weight this material adds to the whole device. The power factor was re-expressed in terms of the thermoelement's weight, in order to make a comparison of the power delivered per unit of mass.

The amount of power (P) delivered by a thermoelement at a specific temperature (T) is the product of the power factor by the square of the operation temperature ($P = T^2(\alpha^2\sigma)$). Using the definition of electrical conductivity in terms of the electrical resistivity, this factor can be expressed in terms of an arbitrary length of the thermoelement as

$$P = (T)^2 \frac{\alpha^2}{\rho} \frac{A}{l}; \tag{2.3}$$

where P is the power, ρ the electrical resistivity, l the thermoelement's length and A is the area of the thermoelement. Note that the units of this expression are W/m. Introducing the density into this formula, a power factor $P'(\gamma)$ which is a function of the density and the area of the thermoelement can be defined as

$$P'(A, \gamma) = \frac{1}{\gamma} PA, \tag{2.4}$$

where P' is the power factor as a function of the density γ. This factor has units of W/kg or W/g. To evaluate the power generated per unit of mass by different thermoelectric materials, thermoelements with a unitary area (A=1 cm^2) were considered and the factor over the whole temperature range of operation for each material was evaluated.

Figure 2.13 shows the amount of W/g each material produces at different temperatures. CNT films have the highest specific-efficiency in the low temperature range, only comparable to the silicon germanium alloy, which is normally used in high temperature applications.

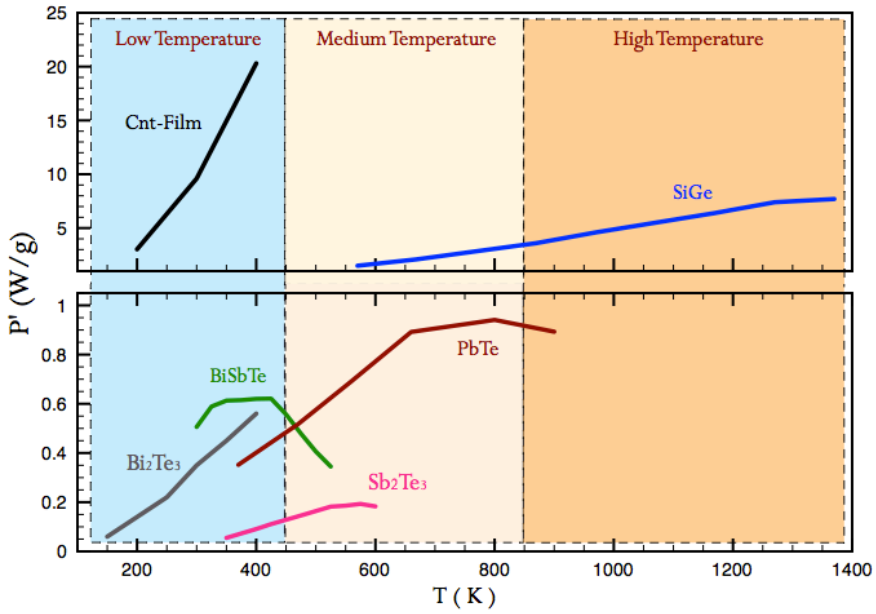

Figure 2.13: Power Factor per unit of mass of the TE materials at different temperatures. Sources: $BiSbTe$ [95], Bi_2Te_3 [87, 88], Sb_2Te_3 [12, 89], $PbTe$ [90], $SiGe$ [22, 96].

A final remark comparing several factors influencing the use of thermoelectric materials in different applications could help understand why it is important to search for new materials for power generation. The weight factor of the thermoelectric materials is an important characteristic to be considered in certain industries. Assuming this is not a decisive factor, one still has to note that the cost of production of some thermoelements could be a limiting aspect.

Some of the semiconducting materials currently used as thermoelements need a high amount of doping to achieve the power factors and figures of merit they show. This turns into a costly and complicated processing methods.

Furthermore, the abundance of some of thermoelectric materials, like tellurium and some other rare earths, is very low and scarcity might be of strategic

importance to manufacturers. Hence several approaches have to be followed in the search for new materials with good thermoelectric characteristics.

2.4 Conclusion

For the presented work, an experimental set-up for the measurement of the Seebeck coefficient of films has been characterised. The adequate experimental parameters required for an optimal performance have been determined and the limitations of the device have been described.

Based on a comparison between the measurements performed with this set-up on calibration samples and their literature values, it is possible to conclude that the results obtained using this set-up are reliable. Further improvements to the device can be made by adding heating and cooling systems to the chamber in order to expand the temperature range where the coefficient is measured. Modifications to the stage holder could be carried out to permit the analysis of samples of different sizes.

The Seebeck coefficient of the CNT films analysed in this work falls within the range of 45 µV/K to 60 µV/K. The magnitude and sign of the coefficient reflects the semiconducting nature of the samples, i.e. the electric transport is dominated by positive carriers. The difference that was found in the magnitude of the coefficient between different samples can be attributed to the variations in their microscopic structure and the hence resulting difference in their transport properties. As shown, the non-uniformity of the material is due to the entanglement of carbon nanotube bundles, which are not perfectly aligned towards one specific direction.

The alignment of the tubes in relation to each other is a factor which could improve the electrical conductivity. A larger contact area between tubes will maximise the chances of electron coupling, which could result in an enhanced electrical conductivity. Therefore, nanotubes aligned parallel to each other are more desirable rather than tubes randomly oriented ones. If such alignment is achieved, the electronic component of the thermal conductivity would also be enhanced. The phonon transfer, which is the second major contribution to the thermal conductivity, is greatly affected by phonon barriers. In this case the junctions between tubes are the main obstacle for the movement of the phonons. Thus, the improvement in the thermal conductivity is not expected to be as large as the one of the electrical conductivity.

Overall, the most important factor to take into account is the network of nanotubes forming the CNT film that needs to be a well connected arrangement of tubes in order to form a good conductor. Since the ratio between electrical and thermal conductivity is one of the factors that defines the efficiency of a thermoelectric material, the enhancement of electrical conductivity through the modification of the tubes alignment should be weighted up by the improvement of thermal conductivity to achieve the optimum ratio between this two transport properties.

An important result obtained is related to the impact of alignment of CNT bundles in the sample. As observed in the previous section, the magnitude of the Seebeck coefficient of a sample with the bundles aligned parallel to the longitudinal axis of the film did not show a significant variation when a sample with bundles aligned perpendicularly to the same axis was examined. This result could imply that other deposition methods, where less control of the orientation of the alignment of the bundles can be achieved, will result in materials with similar thermoelectric characteristics as the ones measured in this work. Methods like printing of CNT solutions on different substrates, sputtering, mixing and sintering of powders could be used to improve the production of CNT-based thermoelectric materials.

Any thermoelectric application requires the junction of a pair of thermoelements. It is desirable to have two different materials with similar thermoelectric characteristics. The principal difference between these thermoelements is that one of them must be a source of positive carriers and the other one of negative carriers. It was found that the samples analysed in this work show a p-type behaviour. The next step for the creation of a CNT material-based thermoelectric device is to find an appropriate n-type material which can be used with the CNT films. One possibility is to use compatible existing materials, i.e. $Cu - Ni$ alloys or Sb_2Te_3 which have a similar Seebeck coefficient, power factor and temperature range of operation as CNT films. Another possibility would be to explore the synthesis of n-type CNT-based material. Combining the aforementioned methods of powder mixing or depositing of CNT solutions with doping could be the route to synthesise a CNT-based material where the main electronic transport is through negative carriers.

3

Thermoelectric device

In the previous chapter, the Seebeck coefficient of carbon nanotube films was analysed and it was concluded that this material has a positive Seebeck coefficient with values ranging from $45\,\mu V\,K^{-1}$ to $60\,\mu V\,K^{-1}$. While the measurement of this coefficient indicates that the CNT films could be used as thermoelectric elements, it is still necessary to evaluate if this material is suitable for its integration into a thermoelectric device that can be used in real-life applications. In this section, the manufacturing process of a carbon nanotube-based thermoelectric generator is described. This device was built with a view to understanding the manufacture requirements needed to process the CNT films into a device that can be used to harvest electrical energy from waste heat.

A thermoelectric generator is a solid-state heat engine in which a flow of heat is converted into electricity. These devices are generally formed by several alternated junctions made of n-type and p-type semiconductors connected electrically in series and thermally in parallel as shown in Figure 3.1. These plates are sandwiched between two thermally conducting and electrically insulating plates to form the thermoelectric module. The efficiency of these devices is defined as the ratio of the electrical power delivered to the load of heat absorbed [97]. In this regard, inorganic semiconductors based on metal alloys like bismuth telluride (Bi_2Te_3) and lead telluride ($PbTe$) are still the preferred components for

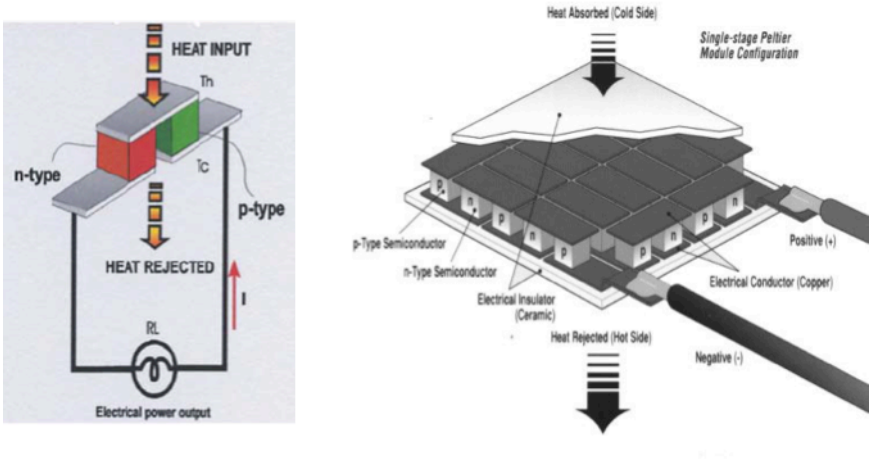

Figure 3.1: Diagram of a thermoelectric unit cell and a thermoelectric generator formed by several units connected electrically in series (reproduced from [38]).

thermoelectric devices. This is because they posses highest power factors which translates into better energy conversion efficiencies [98].

Although inorganic semiconductors are well established as commercial materials for thermoelectric applications, there has been a vast amount of research focused on organic materials. This is due to the fact that inorganic thermoelectrics are normally scarce and difficult to process which increases their production cost. Another important factor that has propelled the research in organic thermoelectrics is a growing number of applications where flexible thermoelectric or materials that can processed over large areas are required. This could be achieved in a cost-effective way using organic thermoelectrics if the manufacturing process and transport properties of these materials are optimised [99, 100].

The development of organic-based thermoelectrics has concentrated mainly on conductive polymers and organic composites made with carbon nanofillers. Conductive polymers have drawn considerable attention due to their relatively high power factors. Seebeck coefficients between $14\,\mu V\,K^{-1}$ and $386\,\mu V\,K^{-1}$ have been measured in Poly(3,4-ethylenedioxythiophene)-poly(styrenesulfonate) (PEDOT:PSS), polyaniline (PANi) and Poly(3-hexylthiophene) (P3HT) and power factors between $3.5\,\mu W\,m^{-1}\,K^{-2}$ and $400\,\mu W\,m^{-1}\,K^{-2}$ have been reported for the same materials [101–104]. Studies have also shown that by combining these polymers with graphene and carbon nanotubes it is possible to increase the power factor of these materials by one order of magnitude achieving values above $1500\,\mu W\,m^{-1}\,K^{-2}$ [105, 106].

Although the thermoelectric properties of inorganic semiconductors and in general their efficiency as thermolements are still better than those of organic

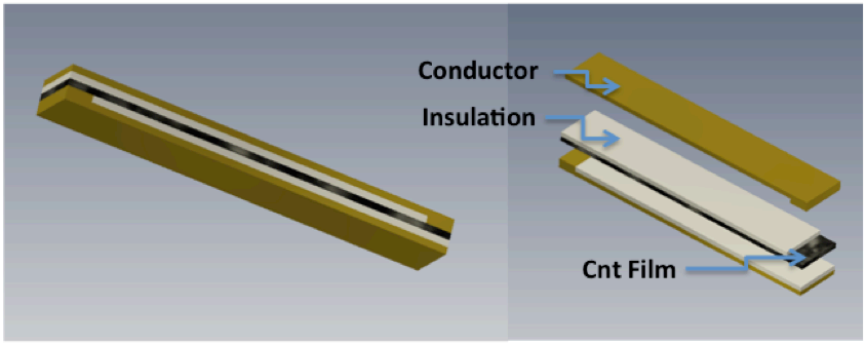

Figure 3.2: Diagram of a thermoelectric unit cell formed by joining a CNT film to constantan.

thermoelectris, over the past few years the field has seen a steady increase in the reported values of the power factor of organic thermoelectrics while the improvement of inorganic materials has stalled. This is related to the possibility of improving the the thermoelectric properties of organic materials through different doping methods or by combining different materials to achieve enhanced electronic properties [100].

In this chapter the performance of a device made using the materials studied in Chapter 2 is presented. As reported, the Seebeck coefficient of the CNT films has a positive value above room temperature and the Seebeck coefficient of constantan is negative in the same range. This will make it possible to use the CNT films as the p-type leg of a thermoelectric device and constantan as the n-type leg.

3.1 Device design

The principal element of a thermoelectric generator is the unit cell formed by the union of two conducting materials. The total power output delivered by the thermoelectric device is the overall sum of the power output of each thermoelectric unit. The design of the device starts with consideration of the thermoelectric unit cell. In the case of the CNT-based generator, a junction of a metal and semiconductor was designed. The cell is formed by connecting a strip of CNT film and two stripes of constantan (45Cu-55Ni) in the disposition shown in Figure 3.2.

In order to keep contact between the carbon nanotube film and constantan restricted to the junction, a thin film of insulating material was placed between the layers. This layout forms a single cell and comprises two junctions or unions of semiconductor and metal. Placing the materials in this disposition puts one junction of the cell in the hot side of the device and the other junction in the cold side ensuring a temperature gradient.

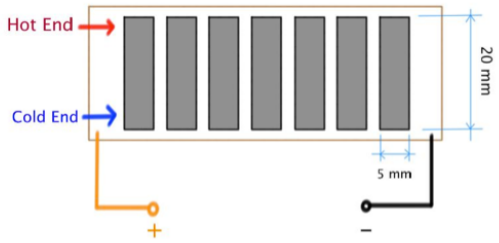

Figure 3.3: Diagram of a thermoelectric layer composed by seven thermoelectric units electrically connected in series.

Each unit cell is 20 mm long and 5 mm wide; seven of them are placed parallel to each other (Figure 3.3) to form one thermoelectric layer. In this disposition, the junctions are thermally in parallel. Once a layer is fabricated it can be stacked and connected in series to another layer. Thus, the generator will be composed by a number of thermoelectric layers packed together. As the number of layers forming the device increases, the voltage generated will increase proportionally.

Since the cells are electrically connected in series, the voltage produced by a single thermoelectric layer will be the sum of the voltages generated independently by each cell. For the same reason, the electric current produced by one layer will be the same as the current produced by a single cell; therefore, if all the cells are connected in series, the overall electric current of the device will be independent of the number of cells in the device.

A thin foil of Kapton was used as the insulation film in each thermoelectric layer of the device. Kapton is a polymer film very thermally stable over a large temperature range, from 4 K to approximately 673 K [107], it is a good dielectric and it is available in flexible thin foils which makes it a suitable insulation layer for the device.

3.2 Device manufacture

The fabrication process of the thermoelectric device starts by cutting the films of CNT and Kapton into single cells. All the cells from both materials must have the same dimensions and, to ensure that the resulting thermoelectric layers are the same size, every cell should be placed in a specific position in the layer. This can be achieved by cutting the films using a laser cutter, which cuts a pattern in the film. The pattern is designed using the laser software, which allows to accurately shape the material into 5 mm × 20 mm stripes. It is also possible, as shown in

Figure 3.4, to control precisely the spacing between the constantan stripes. In this prototype a 2.5 mm gap was left between them.

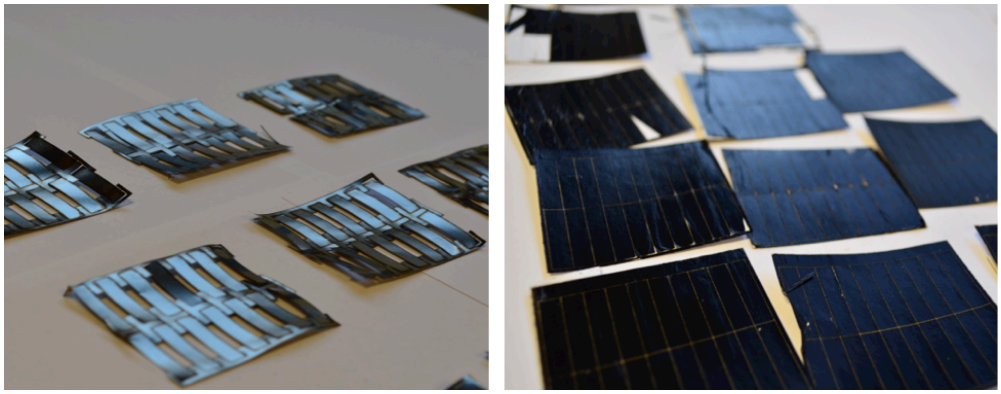

Figure 3.4: Image of patterns cut in the constantan foil and CNT films using a laser cutter.

After the constantan foil was cut in the pattern shown before, it was sandwiched between two pieces of Kapton foil, leaving an exposed space in one of the ends of the stripe to create the junction with the CNT film. Then a strip of CNT film was attached to the constantan to build up seven junctions.

The CNT thermoelements were fabricated from a CNT film synthesised using the floating catalyst spinning method described in Section 2.3. To form CNT film strips with the same dimensions as the constantan strips, the CNT film was cut using a laser cutter. The longitudinal axis of the CNT strips were cut parallel to the direction of alignment of the tubes. This ensured that when the CNT films were placed in contact with the constantan strips, the nanotubes were mainly aligned along the longitudinal axis of the thermoelectric cell. This configuration facilitates the flow of carriers through each thermoelectric cell and through the whole device.

The next step was the isolation of the CNT film by placing another layer of Kapton foil. Again, an exposed space was left in every CNT to create a second junction with constantan (Figure 3.2). The second set of constantan stripes were attached to the CNT to obtain one thermoelectric layer formed by seven cells.

It is important to note that just placing the constantan and the CNT film in contact does not join them; the mechanical contact between the materials does not provide a good electrical and thermal transfer and relying solely on it could cause the device to fail. In fact, one of the major problems in the design of thermoelectric devices is the creation of a good and stable contact between the thermoelements. Several techniques have been developed for devices working at different temperature ranges [108]. In the present case, SCP silver

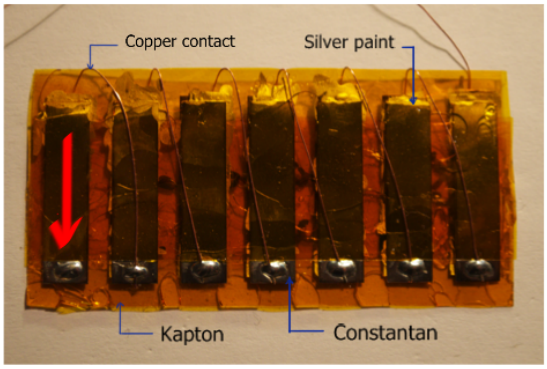

Figure 3.5: Image of a thermoelectric layer comprising seven thermoelectric cells. The red arrow shows the main direction of alignment of the nanotubes in the unit cell. This configuration facilitates the flow of carriers through the TE device.

conductive paint was used to join both materials. According to the manufacturer, the silver content of of this adhesive is 45 %. The remaining 55 % is a solvent that contains 1-Ethoxypropan-2-ol, Acetone and Ethyl acetate. The surface resistance varies between $0.01\,\Omega\,\mathrm{cm}^2$ and $0.03\,\Omega\,\mathrm{cm}^2$ depending on the amount of material deposited on the substrate.

A key technological challenge when creating a TE device is the quality of the interface between the thermoelements. These contacts have to be ohmic and must have a contact resistance with a much lower value than that of the thermoelements. The thermal conductivity should be as high as possible to transfer all the heat flow to the thermoelements. This is why metallic interconnects are usually placed at the interface between the p-type and n-type components. If the contact resistance of the metallic interface is large, heat losses will be produced at the interface between the thermoelements due to Joule heating, this will decrease the magnitude of the thermal gradient which in turns will reduce the current produced by the TE generator diminishing its efficiency [109, 110].

Once the seven cells were created, the electrical connections between them were made using copper cables to join one end of each cell to the end of the contiguous one. The image of the thermoelectric layer in Figure 3.5 shows the final configuration of the cells and the interconnections between them. The red arrow points the direction of alignment of the CNTs in the thermoelectric unit.

The thickness of one thermoelectric layer is approximately 1 mm. Thus, the dimensions of a thermoelectric device formed by 10 cells stacked together are approximately 52 mm × 25 mm and 10 mm thick, as shown in Figure 3.6. These small dimensions would make it possible to accommodate several devices in a reduced area. The overall power output being proportional to the number of

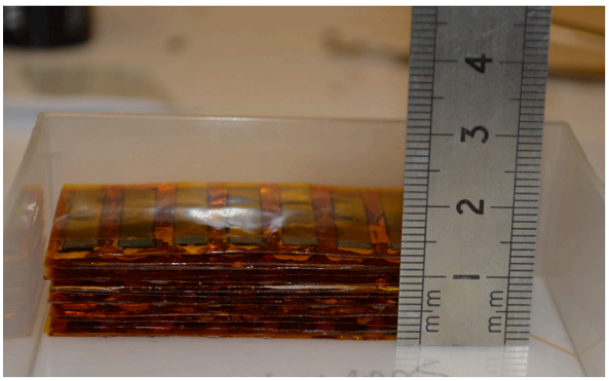

Figure 3.6: Picture of the thermoelectric devices formed by 10 thermoelectric layers.

thermoelectric devices.

To evaluate the performance of one thermoelectric cell, a temperature difference of 373 K between its two ends was set. Then the generated voltage and current were measured. This process was repeated in several thermoelectric units and it was found that the voltage generated under these conditions ranged from 9 mV to 11 mV. The value of the measured output current falls between 3 mA and 4 mA. Since each cell comprises two junctions, these measured values mean that every constantan/CNT junction produced 5 mV and 4 mA on average.

The reason why the variations between the measured current and voltage generated by different cells were observed, is related to the fact that the CNT film is not a uniform material. The properties of this material can have variations even between different parts of the same sample. A slight change in the electrical resistivity of the CNT film will have an effect on the amount of generated current and, as shown previously, the Seebeck coefficient also varies between samples from the same batch.

Measurements performed in single thermoelectric layers resulted in generated voltages of around 70 mV when the layer was exposed to a 373 K temperature gradient. The output current under these conditions remained close to 3 mA.

The finalised first prototype consisted of 22 layers. Although this number of layers should have resulted in 154 connected cells, after a careful evaluation of each unit, it was decided not to connect some of them because their electrical resistivity was very high and if connected, they would have decreased the overall output current of the device. The electrical resistivity of the thermoelectric cells with a good contact between the p-type leg and the n-type leg varied between 1 Ω and 20 Ω. The cells that were fabricated with a defective junction had an electrical resistivity above that threshold and could reach up to 10 MΩ. Measuring

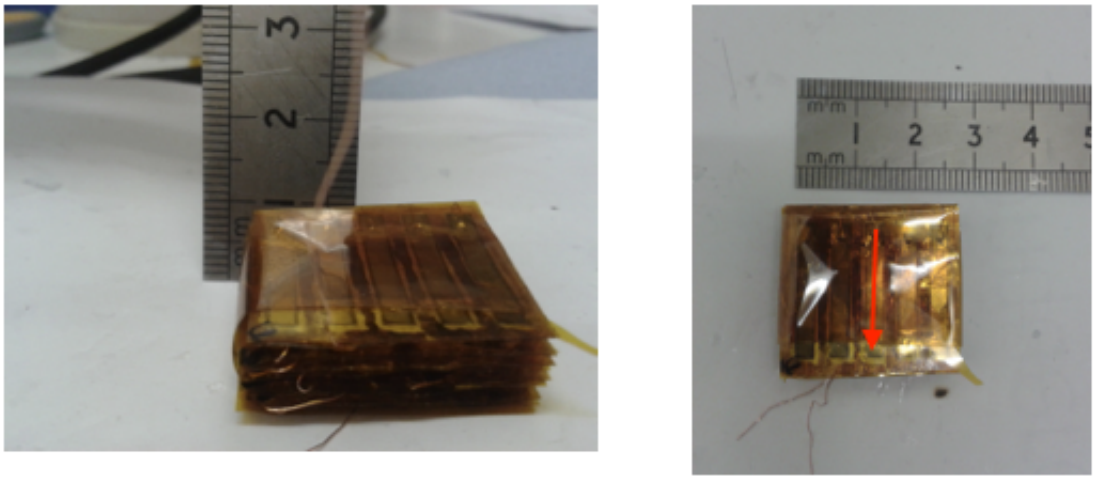

Figure 3.7: Picture of the CNT and constantan thermoelectric device formed by 2.5 mm × 20 mm. The alignment of the CNTs in the TE cell is shown by the red arrow.

the electrical resistivity is a good indicator of the quality of the contact between constantan and the CNTs. The thermoelectric cells with high resistivity were not removed from the generator but just skipped when the electrical connections were made. This resulted in a smaller number of active cells than the total number of cells in the device. The final prototype had approximately 80 % working cells and 20 % non-connected units.

The performance of this thermoelectric generator was evaluated by immersing one of its sides into liquid nitrogen. This means the device was subjected to a temperature difference between its two sides of just more than 220 K. The generated voltage produced by this temperature difference was ≈1.9 V and the electrical current was 3 mA. These results were consistent with the results obtained from the measurements performed in single cells and thermoelectric layers.

A second prototype was built using the same manufacture procedure. This time the width of the cells was 2.5 mm × 20 mm, which is half the size of the cells in the first prototype. The gap between the cells in the TE layer was reduced to 2 mm and the number of cells per layer was reduced to 5. The total number of TE cells in the device was 300. During the manufacture, additional steps where taken to improve the contact between the CNT films and the constantan layer. Silver paint was applied as the metallic interface between constantan and the CNT film, pressure at the interface was applied using clamps and the layer was dried in an oven at 323 K.

Using the same criteria as in the first prototype, TE cells with a resistivity higher than 20 Ω were discarded. The resulting number of cells was 285 cells,

Table 3.1: Comparison between the two CNT and constantan thermoelectric devices

	Prototype 1	Prototype 2
Unit cell dimensions	5 mm × 20 mm	2.5 mm × 20 mm
Total number of unit cells	154	300
Number of active cells	122	221
Voltage per unit cell $\Delta T = 100\,\mathrm{K}$	11 mV	8 mV
Maximum voltage output $\Delta T = 220\,\mathrm{K}$	1.9 V	2.4 V

which was an improvement of 5 % on the percentage of active cells. When a temperature gradient of 100 K was applied to a single cell, the voltage produced was 8 mV. Testing the device under a temperature gradient of 221 K, which was produced by immersing one side of the TE cells into liquid nitrogen, the maximum voltage recorded was 2.4 mV.

Table 3.1 summarises the characteristics and performance of both devices. The fabrication procedure used in the second prototype in which the junctions were hot pressed, improved the quality of the junctions and increased the number of active cells in the device. This resulted in a TE device which could deliver more voltage when subjected to the same temperature gradient. The size of the unit cells was also decreased in the second design, this allowed to pack more TE cell in a similar space, but at the same time decreased the output voltage of each unit cell.

As it was already discussed, the overall conversion efficiency of the thermoelectric device is dependent on the temperature difference, the Seebeck coefficient, the thermal conductivity and the electrical conductivity of the materials. But the key factor in the design of a prototype like the ones just developed is the quality of the junctions between the constantan and the CNT film in each cell. If there is a poor electric or thermal contact between the constantan and the CNT film at the junctions, the amount of heat retained at the junction will be lower and therefore the generated current and voltage will decrease. Also, a small contact area at the union will increase the electrical resistivity of the whole cell.

These results highlight the importance of the interface between the legs of the

TE device. The electrical and thermal conductivity of the material used should be higher than that of the thermoelements, but most importantly, the specific contact resistivity of the interface, which is defined as the contact resistance by the contact area, should be minimised. The specific contact resistance decreases the efficiency of the thermoelectric device according to [109]

$$(ZT_{device}) = \frac{L}{L + 2\rho_c\sigma}(ZT_{thermoelement}), \tag{3.1}$$

where ZT is the efficiency of the device given by the figure of merit Z multiplied by the temperature T. L is the length of the thermoelement, ρ_c is the specific contact resistance and σ is the electrical conductivity. An estimation of the effect of the contact resistance required to have efficient CNT TE devices can be made by assuming an electrical conductivity of the films to be $1500\,\mathrm{S\,cm^{-1}}$ [111]. This means that the contact resistance should be lower than $L/2\sigma$, which is $\rho_c < 6 \times 10^{-4}\,\Omega\,\mathrm{cm}^2$ with $L = 2\,\mathrm{cm}$.

3.3 Conclusions

The methodology to fabricate hand made thermoelectric devices was shown in this chapter. CNT films produced using a CVD method were used as the p-type legs of the TE device and constantan as the n-type semiconductor. To connect these two semiconductors, silver paint was used as an interface material. The performance of both devices was evaluated by immersing them into liquid nitrogen. This produce a temperature gradient of 220 K. Under this conditions, the first prototype produced 1.9 V and the second one 2.4 V.

The difference between the two devices was the dimensions of the TE cells and the manufacture process. In the first prototype, the width of the CNT and constantan stripes were 5 mm and the junction between the n-type leg and p-type leg was made simply by applying silver paint at the interface of the two conductors. The second prototype was manufactured to prove the scalability of the method. the width of the TE cells was reduced to 2.5 mm, but the junctions were fabricated by drying the silver paint in an oven whilst pressing the contact at the interface between the n-type and p-type leg. This new process improved the contact at the interface. The reduced dimensions allowed for more TE cells.

These results showed that improvements to the device could be achieved in several ways. Enhancing the contact between constantan and CNT at the junc-

tions which would result in a better heat and electronic transfer and consequently higher conversion efficiency. Exploring new materials with higher Seebeck coefficients than constantan is another route of improvement. Also, decreasing the electrical resistivity of the CNT film would lead to higher values of generated electric current.

In terms of the design, the spacing between individual cells can still be reduced, which will also decrease the size of the whole device. Potentially, more cells could be accommodated in one generator to have a higher output voltage with a device of the same dimensions as the ones just demonstrated.

But the main conclusion of the present chapter is that the efficiency of a TE device not only depends on having thermoelements with a high Seebeck coefficient and good electrical and thermal transports. The quality of the junction is a key parameter in the manufacture of TE devices. It is required to have a very low contact resistivity at the junction. This would reduce heat losses due to joule heating and would improve the movement of carriers through the interface.

In general, to reduce the contact resistance, ohmic contacts or low Schottky barriers are desired at the interface between the p-type and n-type thermoelements. This type of contacts can be achieved using metallic interconnects. In the case of the p-type CNT films, when this material is in contact with a metallic element, the mismatch between the Fermi level of the metal and the valence band of the CNTs create the Schottky barrier. The height of the Schottky barrier is determined by the electron affinity of the CNTs, their band gap and the work function of the metal [112]. The band gap of the nanotube depends on its chirality and diameter. In the case of the CNT films, which are formed by different types of semiconducting and metallic nanotubes, it is difficult to determine one specific value for the energy band gap and electron affinity. Therefore the analysis should be focused on the metal used at the interface.

Silver paint was used because it simplifies the manufacture process, but there are some other materials which could improve the contact between the nanotubes and the metal at the interface. The contact resistance between a metal and a nanotube is not only related to the work function of the metal, but also to its wettability. When the wettability of the metal is good, like in the case of Cr, Fe an Ti, the work function plays a lesser role in the magnitude of the contact resistance. The better the wettability, the lower the contact resistance. When the wettability of the metal is poor, the dependence of the contact resistance is transferred to the work function of the metal. This effect has been associated

to the number of vacancies in the d orbital of transition metals [113]. Silver has only one d-vacancy and a work function of 4.26 eV, these values are comparable in copper (1 d-vacancy and 4.65 eV, but less attractive than Ti and Cr which have similar work functions but 8 and 6 d-vacancies respectively [113].

This points to the possibility of using other type of metals which would reduce the contact resistivity at the n-type, p-type interface, increasing the efficiency of the TE cells.

It is important to note that there are no limits or restrictions to the number of layers connected in the device or to the number of cells in each layer. Indeed, linear scalability is a key advantage of thermoelectric generators. Therefore, the size of the device is not limited to the one just presented. The size and output values of the generator can be designed to specific applications just by modifying the arrangement of cells and layers.

This motivates a new type of methodology to make the TE devices, if the legs can be fabricated with specific dimension and improved transport properties, there would be more control over the efficiency of the TE device. The following chapters will explore the fabrication of CNT based devices made by a controlled deposition of CNT thermoelements.

4

Carbon nanotube dispersions

In the previous chapter, the manufacture of a hand-made carbon nanotube-based thermoelectric device was demonstrated. Some problems were identified; a number of thermoelectric cells were not active due to the poor electric contact between the p-type and n-type conductors which was caused by the manual assembly of the device. The fabrication process is time consuming which makes it impractical from an industrial point of view. To overcome these problems, the possibility of manufacturing the devices using a printing method was explored.

In order to create macroscopic assemblies of nanotubes using a deposition technology, it is necessary to find a method to disperse the nanotubes in a solution that can be easily deposited using a printer. This objective requires an understanding of the parameters that control the dispersability of the materials. In this chapter the different dispersing methods available are discussed. The development of a methodology to disperse CNTs and its effect on the properties of the nanotubes is investigated in this chapter.

4.1 Theoretical background

The vast majority of applications which could benefit from using carbon nanotubes require the processing of the CNTs into bulk materials that preserve specific properties of the individual nanotubes. Electronic applications where the nanotubes are used as current paths require a final product exhibiting the high electrical conductivity of CNTs, thermal sinks for cooling systems would need the high thermal conductivity of single nanotubes. In reinforcement applications, materials made with a network of nanotubes must maintain the structural strength of the individual tubes.

Unfortunately, the synthesis process of CNTs yields a material made of an entangled network of nanotube bundles. These bundles are formed due to the strong electrostatic interaction between the tubes which pulls them together, forcing them to arrange into stacks of nanotubes. This configuration is known to hinder the transfer of the properties of individual nanotubes into macroscopic assemblies [114].

Carbon nanotubes films, ropes or composites can be manufactured through post processing methods [115–117] or can be produced directly as fibres and films during the synthesis process using a continuous spinning method [81, 118]. To be commercially viable, any of these technologies must be capable of delivering materials with tailor-made properties for specific applications. Furthermore, the production methodology is expected to be scalable in order to be incorporated into industrial manufacturing processes. Up to now, this has been a major barrier preventing the use of carbon nanotubes in real-world applications.

In this respect, processing carbon nanotubes from a fluid-phase into bulk materials offers more control over the properties of the final product than the solid-state production methods. During the solubilisation stage the nanotubes can be sorted or functionalised, careful selection of dispersion method leads to solutions with specific properties. Extrusion or controlled deposition of the solution provides different manufacture paths and paves the way to scalability. Extensive research has been done and is still needed in this field. A successful macroscopic assembly from liquid-phase requires an understanding of the interaction between the different molecules present in the solution as well as the underlying mechanisms of the dispersing methodologies.

When dispersing CNTs in any solvent the principal goal is to achieve a free from aggregates and stable solution. One of the main obstacles to accomplish

this objective is to separate the individual nanotubes from the bundles which means overcoming the strong van der Waals force that keeps the tubes together, approximately 0.5 eV/nm [119]. It is important to avoid the agglomeration of nanotubes in a dispersion because during the phase transformation from liquid to solid the agglomerates can produce stress concentration sites in the structure which could ultimately lead to fractures and failure of the material [120, 121].

The hydrophobic nature of carbon nanotubes which makes them insoluble in water and their high molecular weight that prevents them from dissolving in most solvents are also barriers for the production of good nanotube dispersions. From a thermodynamic point of view, in order to be soluble, the free-energy of mixing ΔG_{Mix} of a dispersion must be negative. The free-energy of mixing is a function of the enthalpy of mixing ΔH_{Mix} and the entropy of mixing ΔS_{Mix},

$$\Delta G_{Mix} = \Delta H_{Mix} - T\Delta S_{Mix}. \tag{4.1}$$

In the case of nanotube dispersions, the high molecular weight of the nanotubes renders a very small entropy of mixing and the discussed strong interactions between tubes makes the enthalpy of mixing of almost all nanotube-solvent mixtures positive. The net effect of the combination of these two factors results in a positive free-energy of mixing, which makes the nanotubes insoluble in most solvents [122].

Several techniques have been developed to disperse CNTs in different solvents. Most of them can be categorised into two different approaches. One encompasses all methods in which the nanotubes are chemically treated in order to modify their surface energy by attaching surfactants or through a functionalisation process. The second approach is dispersing the nanotubes through mechanical techniques like sheer mixing and ultrasonication. These mechanical methods transfer energy to the nanotubes in order to separate them from each other. This process tends to compromise the integrity of the nanotubes and generally reduces the size of the tubes.

Chemically modifying the surface energy of the nanotubes has the objective of maximising the dispersability of the CNTs. It has been shown that the enthalpy of mixing depends on the balance between the surface energy of the solvent and that of the nanotubes. Therefore, the highest dispersability is achieved when the surface energy of the CNTs is similar to the energy of the solvent [123].

There are three methods to accomplish this energy balance. The first one involves the non-covalent attachment of wrapping agents like surfactants, poly-

mers, peptides and DNA to the walls of the nanotubes [124–126]. The second strategy is the covalent functionalisation of the walls of the nanotubes. The objective of these two methods is to improve the wetting and adhesion properties of the nanotubes to make them more compatible with the solvent and reduce their intrinsic agglomeration tendency [127]. The third approach, known as solvent exfoliation, consist of carefully selecting a solvent that matches the surface energy of the CNTs in order to obtain stable solutions.

Using solvent exfoliation, carbon nanotubes can be dispersed without the need of any additives or functionalisation. Solvents like dichloroethane [128], N, N-Dimethylform [123, 129] and N-methyl-2-pyrrolidone [130] are used in this kind of dispersing methods. The principal disadvantages of producing CNT solutions with these solvents are that they are either toxic or posses a low boiling point, which makes their manipulation more complicated and blocks their introduction into practical applications [131, 132].

Covalent functionalisation is a method which involves the non-reversible attachment of chemical moieties to the side walls of the nanotubes. The addition of amino (NH2) and carboxyl (COOH) groups as well as oxygen molecules is attained through chemical treatments [133, 134]. Some of these molecules induce repulsion between nanotubes which aids towards the improvement of the miscibility of the tubes in different solvents. Liquid crystalline solutions of CNTs in water and superacids have been prepared using this method [135–137].

While it is possible to solubilise CNTs in a wider range of solvents using the covalent functionalisation, this process usually requires the treatment of the nanotubes with acids at high temperature. This not only introduces structural defects to the nanotube, but it can also digest partially or completely the CNTs resulting in dispersions with inferior properties [138]. Despite the fact that a method in which the CNTs were covalently functionalised with chlorosulfonic acid reported no damage to the walls of the nanoutbes, the solubilisation is highly dependent on the purity of the CNTs, achieving better dispersabilities with defect-free nanotubes [139]. This hampers the practical feasibility of the process, as it would require to select the nanotubes before dispersing them.

The advantage of using covalent functionalisation is that no additives are required to disperse the nanotubes. On the other hand, any functionalisation induces modifications to the sp^2 framework of the CNTs, which will invariably affect the electrical properties of the nanotubes [133, 140]. This is an important condition to be considered when selecting a dispersion method for electronic

applications where high conductivities are usually required.

The remaining technique, non-covalent functionalisation, is a method in which agent molecules are physically attached to the surface of the nanotubes. The absorption takes places through weak physical interactions such as $\pi - \pi$ staking for uncharged molecules like DNA and uncharged surfactants, Coulombic attraction in the case of charged molecules or hydrophobic interactions for dispersions in water. This approach is very promising due to the fact that it does not alter the $\pi-$electron cloud of the nanotubes, which means that the intrinsic electrical properties of the nanotubes are preserved whilst improving the interfacial interaction between the CNTs and the solvent [141, 142].

The drawback of using the non-covalent method is that the additives used to stabilise the suspension require further purification processes in order to be removed. Sometimes this cannot be achieved completely, resulting in additional electrical resistance at the nanotube junctions [143].

The mechanical methods, ultrasonication and sheer mixing, are used to input energy into the solution. This energy serves to separate the tubes and create inter-space for the stabilising molecules. It is important to note that the utrasonication or sheer mixing of a solution without the adequate selection of a solvent or stabilising agent will lead to reaggregation of the CNTs. A second consideration to be made is that the use of mechanical energy invariably damages the structure of the nanotubes. For these reasons the sonication parameters to achieve a an optimal dispersion need to be determined for every specific application. The sonication mechanisms are discussed in detail in Section 4.3.

In order to develop a dispersion methodology whose final product could be used in a wider range of applications, the use of toxic solvents and methods that could highly compromise the integrity of the transport properties of the nanotubes was avoided. Throughout this work, the parameters to fabricate dispersions of nanotubes in water that could be deposited using a printing system were researched. The following section covers the selection of the surfactant and its effect on the nanotube dispersion properties.

4.2 Surfactants

Surfactants are molecules composed of polar and apolar groups. Due to their tendency to adhere at the interface of immiscible phases and form supra-molecular structures through self absorption, these molecules are widely used in the production of dispersions. Structurally, a surfactant is an amphiphilic molecule, with the polar head being the hydrophobic region and the tail group or hydrophobic section which is generally formed by hydrocarbon chains [127].

The classification of surfactants is done according to the charge of its polar head. Those with no charge are called non-ionic surfactants and ionic surfactants are those with a charged head. More specifically, ionic surfactants with a positive charge are known as cationic and anionic if they posses a negatively charged head. Non-ionic surfactants attach to the surface of the nanotubes through strong hydrophobic interactions between the surface of the particle and surfactant's tail. The interaction of ionic surfactants with the particle's surface is driven by Coulombic attraction between the charged head and charged regions in the particle [144].

The mechanisms by which nanotubes are dispersed in water depend on the specific surfactant used. In broad terms, these molecules coat the nanotubes inducing electrostatic or steric repulsions that oppose the van der Waals attraction between the nanotubes impeding their agglomeration. At the same time, the hydrophilic groups of the surfactant associate with water, which reduces the surface energy of the interface resulting in a thermodynamically stable dispersion [145].

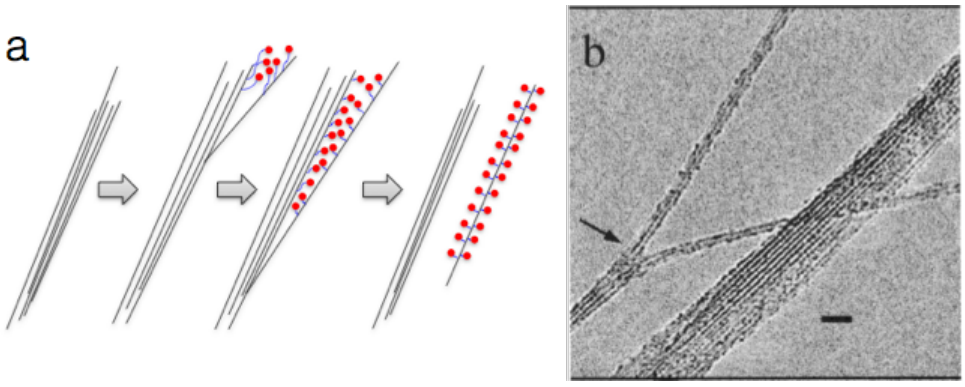

Figure 4.1: A) Diagram of the debundling process induced through high shear sonication and the absorption of surfactant molecules. B) cryo-TEM image of a nonutbe dispersion. The arrows show the location of the surfactant molecules. Image reproduced from [146].

Carbon nanotube dispersion in water are generally achieved through the sonication of an aqueous solution containing CNT and low surfactant concentrations.

It has been proposed that the sonication provides the energy necessary to separate the ends of the bundles through high local shear. A diagram of this process is shown in Figure 4.1. The spaces created between the nanotubes serve as sites for the absorption of surfactant molecules. As the high shear continues separating the nanotubes the absorption process also continues and the surfactant propagates along the bundles separating them in a unzip-like fashion [147]. The TEM image by Bandyopadhyaya et al. in Figure 4.1 shows this process happening in a dispersion of CNT using Gum Arabic as surfactant [146].

During the dispersion process, an equilibrium between the surfactant particles, the nanotubes that have been separated from the bundles and CNT aggregates is established. This equilibrium is dependant on the surfactant's concentration [147]. The concentration at which the agent molecules have occupied all the available spaces in the nanotube walls is know as the critical micelle concentration (CMC). Below this concentration, the surfactant molecules cannot fully balance the electrostatic forces between the nanotubes and aggregates can still be found in the dispersion. Above the CMC, the surfactant start to self-aggregate into supramolecular assemblies called micelles [148].

The interaction between the surfactant and the CNTs depends on how the surfactant molecules arrange themselves onto the nanotube walls. Several configurations depending on the surfactant's concentration have been proposed. Simulations show that at low densities the surfactant molecules lay flat on the surface of the nanotubes and evolve with increasing concentrations into cylindrical micelles or hemimicelles which can accommodate a higher density of molecules [149–151]. Other studies found that there is no particular arrangement of the surfactant on the nanotubes and that the final configuration is also dependent on the nanotube diameter [152–154].

The dispersing efficiency of a surfactant is also related to how strongly it attaches to the surface of the nanotube. Surfactants possessing a benzene ring in their structure have a better adsorption due to the $\pi - \pi$ interactions with the nanotube walls. The length of surfactant's alkali chain also affects its dispersing power. Longer tails provide higher spatial volume which translates into stronger repulsive forces which keep the individual nanotubes apart from each other [141]. When surfactants with a similar benzene rings or headgroups were compared, those with larger tails proved to be better dispersing agents. Dodecyl was found to be the minimum alkali chain length needed to disperse SWCNTs [124, 151].

Despite the fact that ionic and non-ionic surfactant are both capable of dis-

persing CNTs in water, using non-ionic surfactants can lead lower electrical conductivities. The dispersing mechanism of non-ionic surfactants is highly dependent on the size of the hydrophilic group of the molecule. Therefore polymers with high molecular weight are needed to disperse the CNTs in water. Using surfactants with long hydrophilic tails creates large spaces between tubes which results in an increased percolation threshold [155]. This is a disadvantage for applications which require the formation of a nanotube network that permits electric transport.

A wide variety of ionic surfactants can be used to disperse CNTs in water. Amongst them, the molecular surfactants sodium dodecyl sulfate (SDS) and sodium dodecylbenzenesulfonate (SDBS) are widely used due to their high nanotube quenching rate. Both surfactants have a polar headgroup and a symmetric non-polar tail. They differ by the benzene ring which is only present in the structure of SDBS.

Studies comparing these surfactants have shown that the desorption energy of SDS is larger for tubes with small diameters, which translates into SDS being more efficient at dispersing small diameter tubes. This tendency has not been observed in SBDS, which suspends equally nanotubes of all diameters. This diameter dependence of SDS can be explained if it is considered that smaller nanotubes permit a higher packing density of the surfactant tails leading to a reduction of the electrostatic repulsion of the headgroups. In the case of SDBS, this effect is enhanced by the attraction between the benzene rings, which balances the surfactant molecules regardless of the tube diameter [156, 157].

The amount of surfactant required to prepare a water dispersion of CNTs is a function of the CMC. The lower the CMC value, the lower the surfactant concentration required to achieve an stable dispersion. Taking into account the diameter dependence of SDS and the fact that SDBS has a lower CMC than SDS, SDBS can be considered as a more suitable choice for the fabrication of conductive macroscopic assemblies of nanotubes from aqueous dispersions [156, 158].

Although SDBS is commonly used in personal care and household products like soaps, detergents and toothpaste. Studies in human skin and other animals reported that the product can cause skin irritation and eye damage [159, 160]. But the main cause of concern when using SDBS is its environmental impact. Reports have shown that the swimming behaviour of fish can be affected by concentrations of SDBS higher than 12.5 mg/l in water [161, 162]. Despite the fact that most surfactants are degraded in sewage plants or by microbial activity, its excessive

use could cause an accumulation that would have a detrimental impact to the ecosystem [163]. From this perspective it is important to minimise the use of surfactant molecules in the preparation of CNT dispersions.

4.2.1 Experimental section

The carbon nanotubes used in this work were synthesised via Chemical Vapour Deposition (CVD). A mixture of ferrocene and toluene is introduced into the hot zone of a furnace using a flow of argon as a carrier gas. In this process toluene acts as the carbon source. Inside the high temperature section of the furnace, ferrocene decomposes into iron particles that serve as a catalyst for the nucleation of the carbon atoms. While the synthesis process continues, the nanotubes tend to grow aligned perpendicularly to the quartz substrate. This CVD technique produces a combination of single walled (SWCNT) and multi-walled nanotubes (MWCNTs) dominated by tubes of several walls. It has been reported that the diameter of the nanotubes falls between 20 nm and 70 nm [164, 165].

A solution with a 5 % mass fraction of ferrocene in toluene was injected at a feed rate of 5.6 ml/min into the first section of the furnace. This zone was preheated to 180 °C to ensure the evaporation of ferrocene and toluene. The flow of argon was set to 1 l/h to transport the feedstock into the second stage of the furnace which was heated to 760 °C. The synthesis process lasted 6 h.

The formation of CNT films from a liquid phase requires the deposition of the solution onto a substrate. During this process it is fundamental to have control over the ratio of evaporation speed of the solvent to the lateral spreading of the dispersion [166]. For water-based CNT suspensions, the quality of the dispersion has a strong effect on the film formation process. Figure 4.2 shows a dried drop of a CNT dispersion deposited on a glass slide. The strong attraction between nanotubes causes their re-aggregation into small islands. This occurs due to the non-homogeneous evaporation process which is promoted by different concentration gradients in not fully dispersed solutions [167].

Due to their high surface-to-volume ratio, surfactant molecules adsorbed on the surface of the CNTs are a considerable fraction of the mass of the CNTs [168]. These molecules create electrical barriers at the junctions between nanotubes diminishing the electrical conductivity of the whole CNT network. For these reasons it is necessary to find the minimum surfactant to CNT ratio that maximises the solubility of the nanotubes in water. To determine this quantitative relation five dispersions were prepared keeping the CNT concentration

Figure 4.2: Effect of the dispersion quality on the deposition of water-based CNT solutions.

constant and varying the surfactant concentration.

A 1 % mass fraction of CNT were dispersed in 25 ml of deionised water. The surfactant mass concentrations of the dispersions were 0.25 %, 0.5 %, 1 %, 1.5 % and 2 %. The surfactant used was dodecylbenzenesulfonic acid sodium salt, 88 %, technical grade from ACROS organic. Each dispersion was sonicated for 1.5 h using a digital sonifier Branson 450 with a 19 mm disruptor horn. This equipment provides a 20 kHz sonication frequency and adjustable power output with a maximum of 400 kW. The sonication parameters were set to 20 % of the power output and an intermittent sonication pulse of 2 s ON and 0.5 s OFF. To maintain the dispersion at a low temperature and avoid water evaporation during the sonication process, the suspension was immersed in an ice-bath.

Immediately after sonication, 1 g of each dispersion was separated on a vial and centrifuged for 1 h at 220 Hz using an Eppendorf 5415R centrifuge. Figure 4.3 shows a picture of the 0.5 % to 2 % dispersions (from left to right) after being centrifuged. It can be observed that the precipitation of the nanotubes is higher as the surfactant concentration increases. Above 1 % mass fraction of SDBS the precipitation of the nanotubes becomes apparent and at a concentration of 2 % the majority of the nanotubes have precipitated.

At surfactant concentrations above the CMC surfactant aggregates are formed. These micelles do not fit between nanotube bundles and as consequence they start exerting an osmotic pressure around the bundles that they surround. This effect is

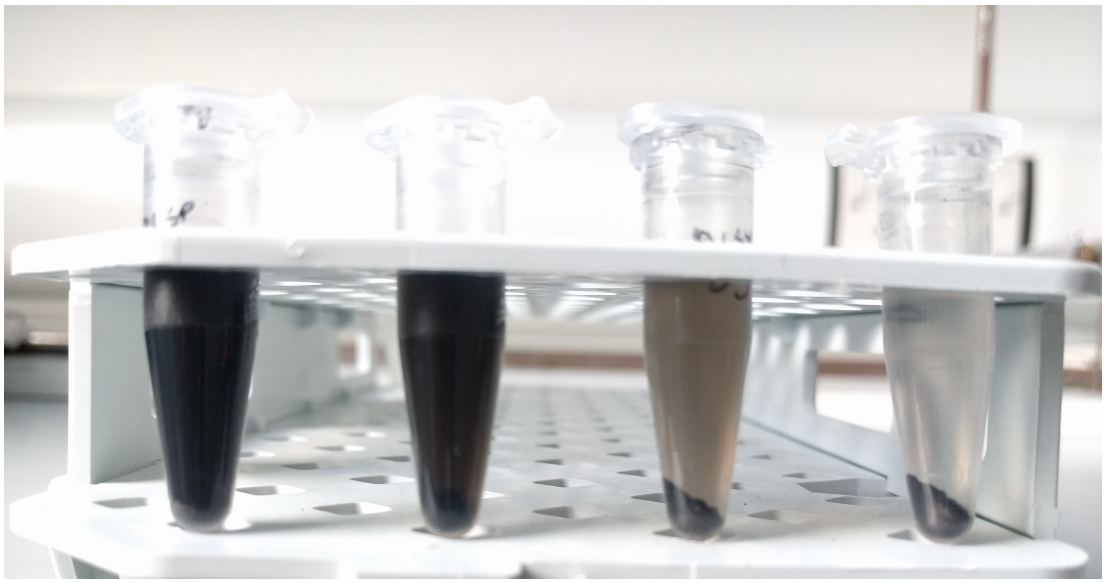

Figure 4.3: CNT and SDBS dispersion centrifuged at 220 Hz. The SDBS concentration from left to right are 0.5 %, 1 %, 1.5 % and 2 %.

known as depletion attraction and causes the reduction of the electrostatic repulsion between the nanotube bundles. When the pressure generated by the micelles is high enough, the net effect is an attraction between the nanotubes which forces them to re-aggregate in order to reduce the osmotic pressure [169–171]. This explains the precipitation observed in the dispersions above 0.5 % concentration. The optimal surfactant concentration is achieved when a balance between this depletion interaction and the maximum surfactant absorption is reached.

Thermogravimetric analysis (TGA) was carried out to determine the exact concentration of SDBS and CNTs in each dispersion. TGA is a destructive analytical technique used to measure the thermal stability of materials. By heating up the material and recording the mass loss as a function of temperature, the ratio of volatile components in a sample can be determined. TGA measurements can be carried out in an inert or an oxidative atmosphere [172]. In a standard measurement a constant heating rate is applied. The resolution of the measurement is dependant on the magnitude of the heating rate. Smaller heating ramps will normally result in higher resolution measurements but will take considerably more time. An alternative technique called high resolution TGA uses a dynamic heating technique in which the heating rate is modified according to the mass change of the sample. If there is no mass change the heating rate remains constant but when the instrument detects a mass change, the heating rate is decreased to achieve higher accuracy. This technique has the advantage of im-

proving the resolution of the measurement without extending the length of the experiment but it is restricted to instruments with this capability [173, 174].

The thermal decomposition of CNTs is well documented. During the thermal degradation of CNTs, the major mass loss is attributed to the oxidation of carbon into gaseous carbon dioxide. The carbon content of the sample corresponds to CNTs and carbonaceous materials. The degradation of the latter is expected to be the first one to occur followed by nanotubes with defects and small diameters. Defects like vacancies, dislocations or any disruption in the CNT lattice increase the reactivity of the CNTs. The diameter of the nanotubes also has an effect on the reactivity of the material. As the degree of curvature of the tube increases, the reactivity also increases. For this reason SWCNTs and tubes of small diameter will degrade faster than MWCNTs. The amount of metallic particles in the sample can also be determined using TGA if the measurement is stopped before the degradation temperature of these particles is reached [173, 175–177].

Using TGA, the concentration of SDBS that produces the highest concentration of nanotubes in a dispersion was found. The measurements were performed using a Meter Toledo thermogravimetric analyser. The samples were placed in 70 µL alumina crucibles and introduce into the equipment at 30 °C. All the measurements were carried out in air. The temperature range of the analysis was set from 30 °C to 1000 °C. The heating ramp used in all measurements was 10 °C/min. For higher accuracy, prior to any set of experiments, a measurement with empty crucible was performed (blank curve) and the results were used to automatically subtract the background noise.

Figure 4.4 shows a typical curve of the thermal decomposition process of a CNTs and SDBS dispersion. Immediately after the sonication process, a sample of supernatant was taken and TGA was performed. The major drop in weight observed between 80 °C and 150 °C corresponds to the evaporation of water. Given the composition of the sample, the remaining material after 150 °C is a combination of carbon nanotubes, SDBS and possible residues of the CNT synthesis. The inset in Figure 4.4 shows that the decomposition of these materials occurs between 300 °C and 650 °C. This particular sample contains 96.7 % of water and 2.3 % of carbon and surfactant. The remaining 1 % which can be calculated from the tail of the curve after 800 °C corresponds to the residues of the catalytic iron used in the synthesis process of the nanotubes.

Further thermal analysis was performed to understand the decomposition of CNT and SDBS and to determine the exact ratio of theses materials in the

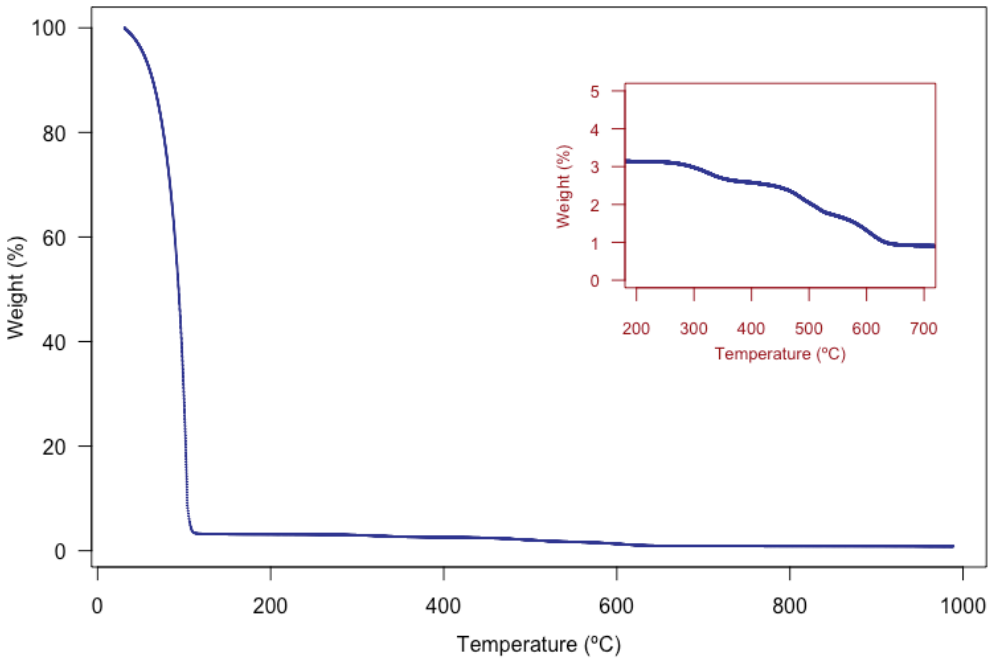

Figure 4.4: Thermal decomposition curve of a CNT and SDBS dispersion in water. The inset shows the detail of the second weight loss that occurs between 300 °C and 650 °C.

dispersion. For this purpose, liquid samples were placed in pre-weighted alumina crucibles. Before carrying out the TGA, the water in the sample was removed by placing the crucibles in a hot pan at 100 °C for 30 min. The dried samples were analysed using the same experimental parameters.

The results of the TGA of a dried sample are shown in Figure 4.5. The black curve represents the weight loss of the sample and the red curve is the first derivative. The maxima points of the derivative mark the temperatures at which the highest flux of heat occurs. These points in the curve represent the thermal stability of material and are used to determine its oxidation temperature [178]. Single peaks in this curve indicate the decomposition of an individual material. Shouldered peaks like the one seen in Figure 4.5 between 400 °C and 700 °C occur during the thermal degradation of multiple materials.

The deconvolution of these peaks can be done by analysing the decomposition curves of CNT carpets and surfactant. The TGA curve of a powder sample of SDBS is shown in Figure 4.6. Two plateau regions are clearly defined: the first one from room temperature to 400 °C followed by major mass fraction loss of 50 % which occurs between 400 °C and 450 °C. This first decomposition step can be

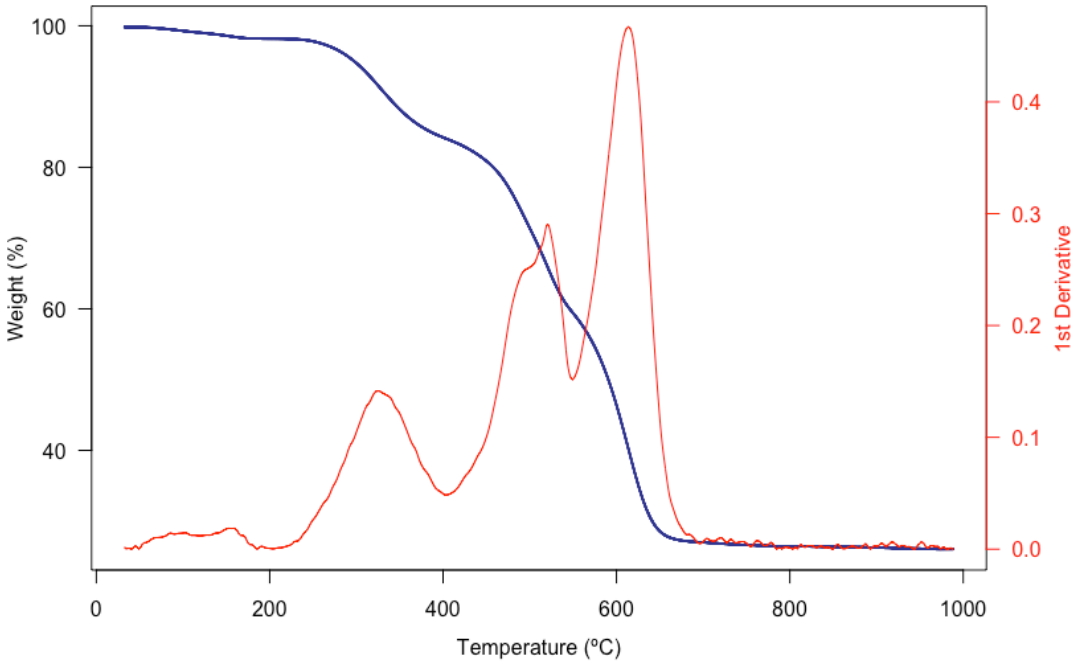

Figure 4.5: TGA curve of a dried sample of CNTs and SDBS. The black curve represents the weight loss of the sample at different temperatures. The derivative curve in red has been inverted for visualisation clarity.

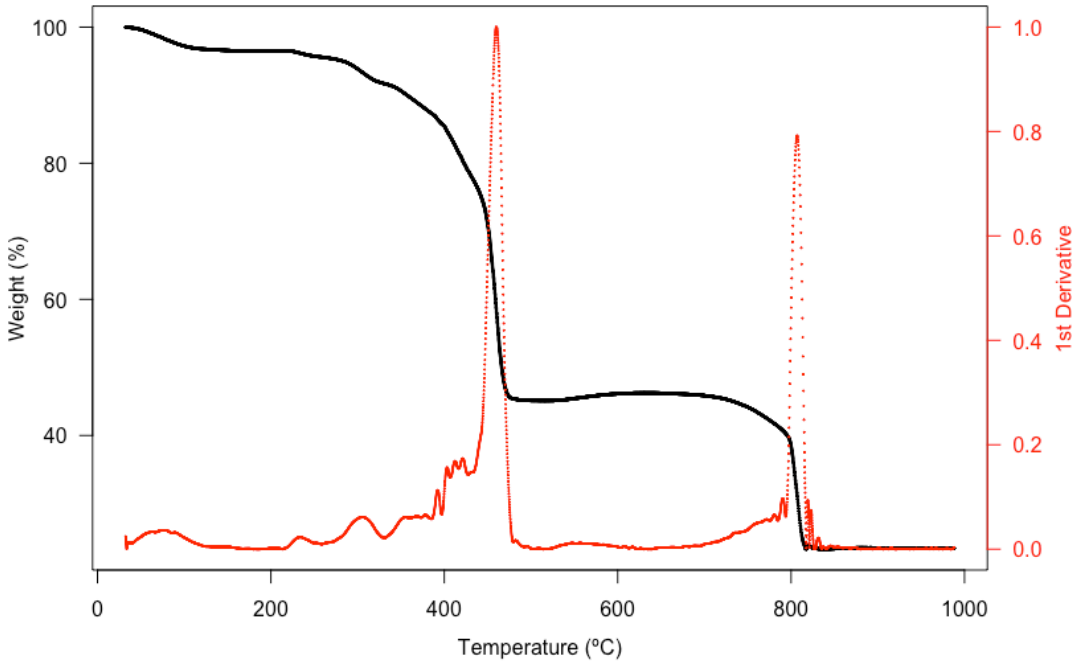

Figure 4.6: TGA curve of SDBS powder. The black curve correspond to the weight loss and the red curve is the 1st derivative.

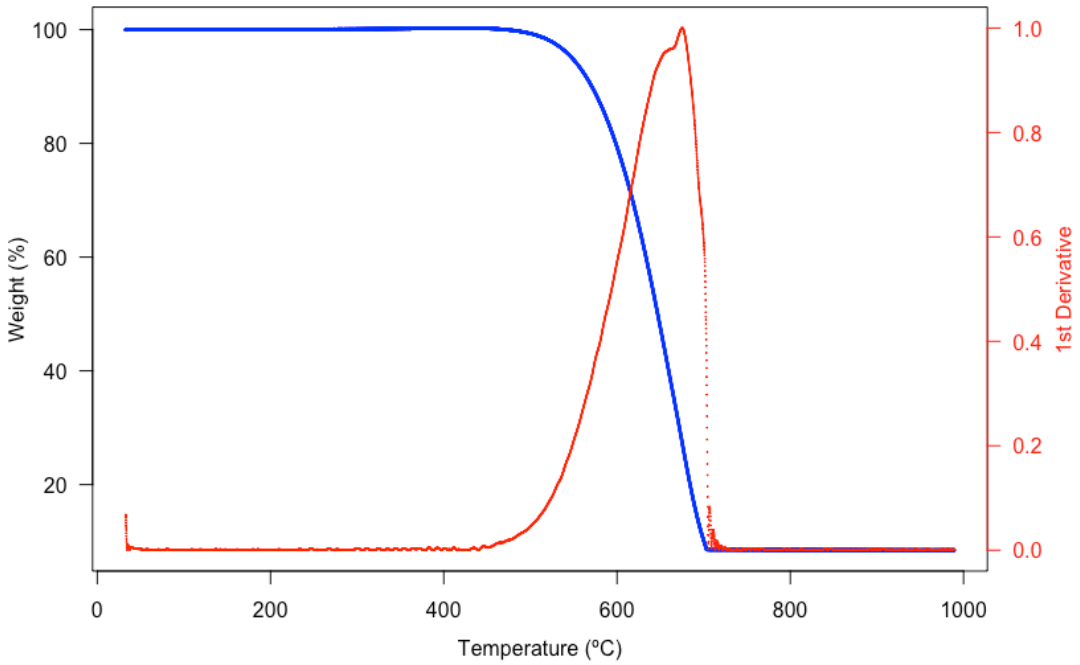

Figure 4.7: TGA curve of as prepared CNT carpets.

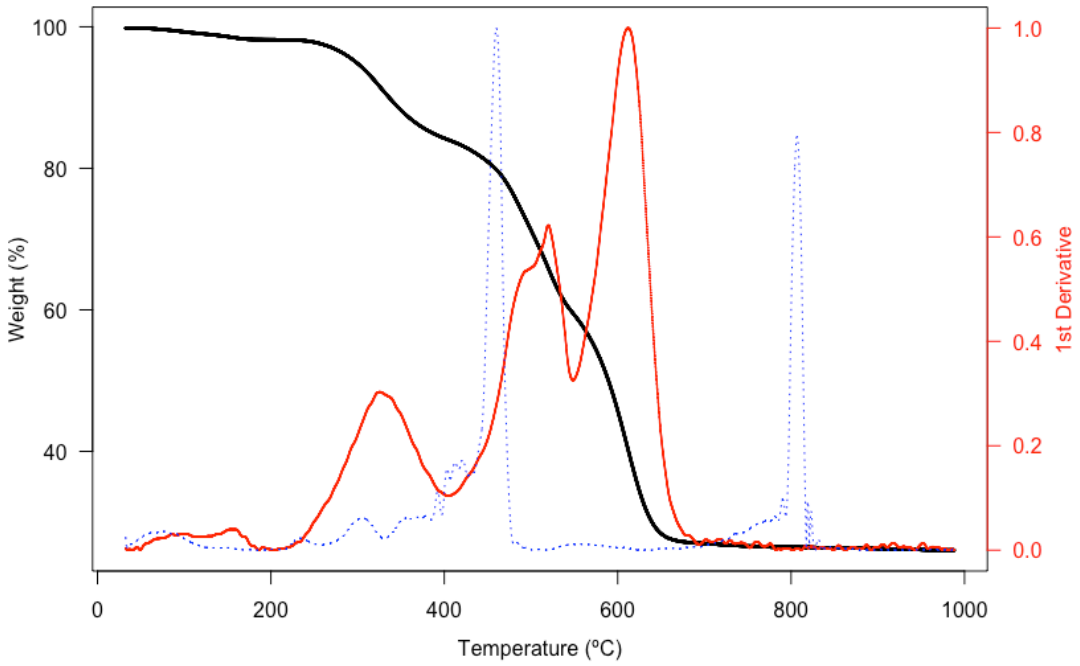

Figure 4.8: TGA curve of a dried sample of CNTs and SDBS showing the derivatives of the carbonaceous elements (red curve) and the surfactant (blue dotted curve).

attributed to the degradation of the dodecyl chain ($C_{12}H_{25}$) which corresponds to approximately 49 % of total molecular weight. The remaining polymer would be an aromatic compound which remains stable until the second decomposition at 800 °C. This organic compound has double bonds and a SO_3 group which stabilises it. After the full decomposition of this polymer, there is a residual compound of sodium, possibly sodium oxide (Na_2O), equivalent to 20 % of the total weight. This residual material remains stable until the end of the experiment.

Figure 4.7 shows the TGA performed on as produced CNT carpets. The carbon based material starts burning at 470 °C. Between this temperature and 550 °C the weight loss can be attributed to the degradation of small diameter tubes, amorphous carbon and highly defective nanotubes. These materials are thermodynamically less stable than the well-structured carbon [178, 179]. A major mass-loss event occurs between 550 °C and 700 °C, it corresponds to the degradation of different CNTs species. The high temperature achieved during this step can be associated to the amount of MWCNT present in the sample [180]. The residual mass left after 700 °C, approximately 8.5 % of the total weight, are the iron particles used as catalyst in the synthesis process.

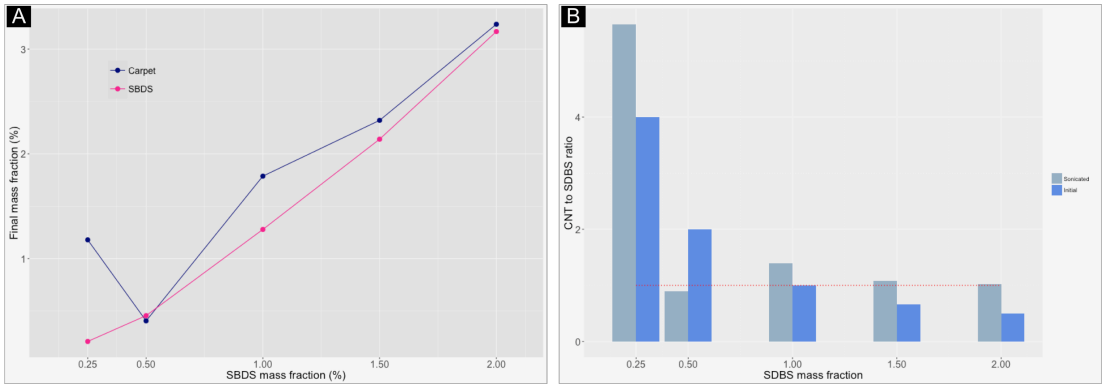

Figure 4.9: A) Surfactant and CNT concentration of dispersions with varying initial surfactant mass fraction. B) Initial and final CNT to SDBS ratio

Overlapping the derivative curve of the SDBS decomposition process (dotted line) to the degradation curve of the dried dispersion in Figure 4.8, the exact composition of the dispersion can be determined. At 450 °C, 20 % of the material has been evaporated. According to the analysis of SDBS, this amount corresponds to 50 % of the total amount of surfactant in the dispersion. This means that this particular sample contains 40 % of surfactant and 60 % of carbonaceous materials and catalytic particles. After this temperature and before 550 °C there is a weight loss of 20 % due to the oxidation of amorphous carbon. The thermal degradation of the CNTs occurs between 550 °C and 720 °C and corresponds to 34 % of the total mass of the sample. The residual mass of 26 % are the remaining surfactant particles and the catalytic iron.

This particular sample was prepared with 1 % mass fraction of CNT and 1 % mass fraction of SDBS. The results of the TGA correspond approximately to the original proportions. 60 % of the material comes from the CNT carpets and 40 % from the surfactant. The CNT concentration of the dispersion considering the amorphous carbon is thus 1.08 % and removing the defective carbon and the iron particles is 0.68 %. This is the amount of material that will contribute to the formation of the CNT network.

Using this type of analysis, the final carbon nanotube and surfactant concentration for each dispersion was calculated. The results are plotted in Figure 4.9.A The initial CNT mass fraction of every dispersion was 1 %. The concentration increased due to the evaporation of the solvent during the sonication process. The highest concentration of nanotubes after the dispersing process was achieved with a surfactant concentration of 0.25 %. As the SDBS concentration increased, the ratio of surfactant to CNTs appears to achieve a limit.

This is illustrated in Figure 4.9.B. The plot shows the initial and final ratio of CNT to SDBS. The highest ratio achieved was CNT:SDBS equals 1:5. When the SDBS concentration increased, the ratio tends to a value of 1:1. This result is important as it means that no matter how much surfactant is added to the dispersion. The maximum concentration used should be equal to the concentration of CNTs.

4.3 Effects of sonication

As discussed in Section 4.2, some form of mechanical energy is used to separate the nanotubes and introduce the surfactant molecules needed to solubilise them in water. The main drawback from this technique is that it introduces defects to the nanotubes, from wall fractures to the complete destruction of the tubes. The destruction of single walled nanotubes starts in localised regions of the CNTs, breaking them into smaller tubes. In the case of multiwalled nanotubes it commences destroying the outer walls, thinning the tubes at the same time that it shortens them. If the nanotubes are completely destroyed they transform into amorphous carbon. All these damages alter the electronic properties of the CNTs. It is therefore important to control the sonication parameters to be able to de-bundle them with a minimum damage to the nanotubes structure [181–183].

When the nanotubes are ultrasonicated three physical processes occur, formation and destruction of bubbles, heating and formation of radicals. The formation of bubbles or cavitation is the main cause of nanotube damage. As the bubbles nucleate on the nanotube walls they grow and collapse, releasing energy that can push the nanotubes apart or damage the CNTs walls at the nucleations sites. The size of the bubble is determined by the oscillation frequency of the ultrasonication equipment. High frequencies of approximately 4000 kHz typical in ultrasonication baths produce small bubbles. Low frequencies of about 20 kHz are common in disruptor horns. At this low frequencies large bubbles are produced releasing more energy when they collapse [138].

As the ultrasonicator horn oscillates at a fixed frequency, energy is transferred to the fluid within a conical area surrounding the horn tip. The bubble nucleation and collapse causes a flow of material that leaves and re-enters the energy field around the tip. The size of this conical area depends on the viscosity and boiling point of the fluid. In solutions with high viscosity the recirculation through the energy zone is reduced which decreases the efficiency of the sonication. In the

case of carbon nanotubes, bubbles can become trapped within the CNT bundles, which also reduces the liquid flow affecting the energy transfer to the solution. This effect is therefore intensified with high CNT loadings which increase the viscosity of the dispersion [138].

If CNTs are dispersed in water through sonication without any additives, the CNTs will re-bundle after the sonications stops. Using a surfactant in the dispersion will prevent re-agglomeration to happen. A previous study has shown that the addition of surfactants does not have an effect on the shortening of the nantotubes, only helping the de-bungdling process. This study also suggests that the first process to occur during sonication is the disentanglement of the nanotube bundles and then the tube degradation upon continued sonication [142]. This theory rivals the conclusions of other works that suggest the shortening occurs immediately after the sonication starts [184, 185]. In either case, it is important to limit the sonication time to avoid tube damage.

4.3.1 Experimental section

To study the effect of sonication on the carbon nanotube length, CNTs were dispersed in water using the same procedure described in Section 4.2.1. The Branson sonifier was used with a 20 % amplitude power and the horn tip was immersed 50 mm into the solutions. The energy transfer from the horn to the sample depends on the immersion depth of the horn into the liquid. For a fixed power amplitude, the ultrasonication rate energy increases with the immersion depth [142]. It is thus important to maintain the immersion depth as a fixed parameter in order to compare the results of the different experimental runs.

The sonication process causes the dispersion to heat up. The increase in temperature is high enough to evaporate the water. To avoid this, the samples were placed into an ice bath during the experimental runs. For dispersions with a high CNT content (> 0.5 wt%) the energy transfer from the sonicator horn to the sample is restricted by the large particles formed by the entangled nanotubes. The CNT bundles have a large aspect ratio and empty spaces between the nanotubes, the volume that a few mg of CNTs occupy is large enough to saturate the solvent, this prevents the flow of liquid to leave and re-enter the energy field around the horn tip. This can be observed during the sonication as the nanotubes are only dispersed in the conical area formed around the horn tip.

This effect can also be observed if the power output of the sonicator is plotted at different times during the sonication process. Figure 4.10 shows the evolution

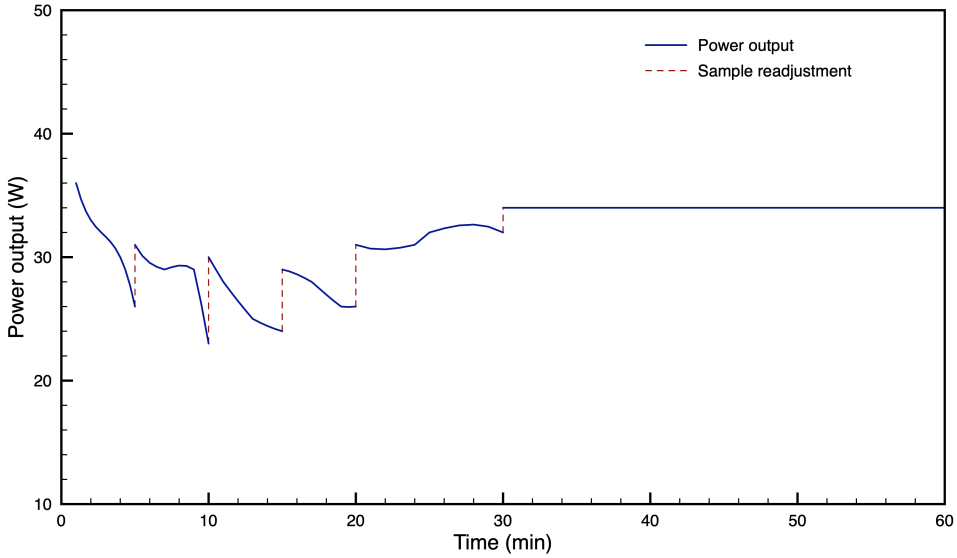

Figure 4.10: Evolution of the sonicator power output for a 0.5 wt% CNT and SDBS dispersion in water. The blue line represent the power output at different times during the sonication. The red dotted line marks the points where the process was stopped and the sample manually readjusted.

of the sonicator's power output when dispersing a 0.5 wt% solution of CNTs and SDBS in water. This measurements were made using the Branson sonicator at 20 % of power amplitude. The blue line represents the power that the horn delivers to the sample. The initial power, 36 W, decreases as the CNTs around the horn are dispersed but contained within the conical area around the horn. To prevent this from happening, the instrument was stopped and the sample manually mixed and placed again in the sonicator. This manual readjustment of the sample is marked in Figure 4.10 as the red dotted line. Throughout the experiment this effect repeats until the nanotubes achieve a degree of dispersion that allows the recirculation of liquid around the tip. This is observed in Figure 4.10 as the increase in power transmitted to the sample between 20 min and 30 min. After this point there is a constant recirculation of fluid which translates into a constant energy transfer from the sonicator tip to the dispersion.

For dispersion with a CNT load of 1 wt% or above, the minimum amount of time required to fully disperse the nanotubes is between 2 h and 3 h. Two dispersions with a CNT mass fraction of 1 % and 0.25 % of SDBS were prepared to investigate the effect of this amount of sonication on the size of the tubes.

The first dispersion was sonicated for 2 h at 20 % of the power output of the sonicator. The second dispersion was sonicated for 3 h. An intermittent sonication pulse of 2 s ON and 0.5 s OFF was set for both sonication processes.

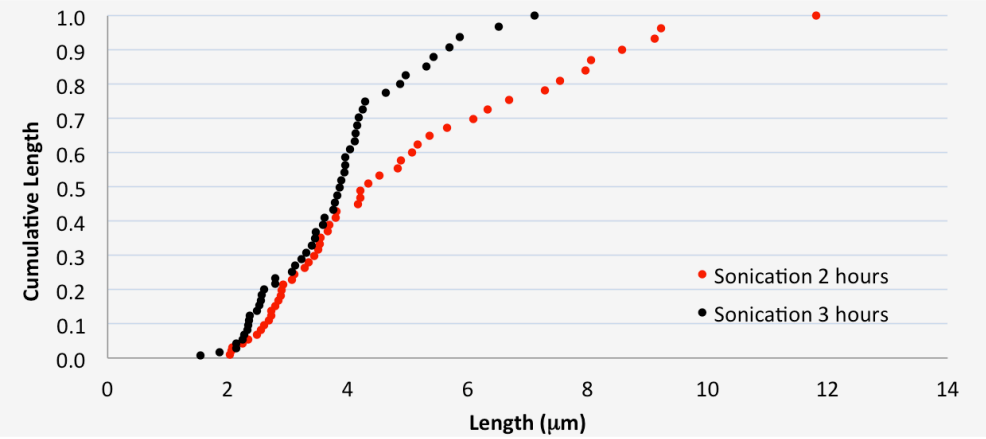

Figure 4.11: Cumulative length distribution of MWCNTs after a sonication process of 2 h and 3 h.

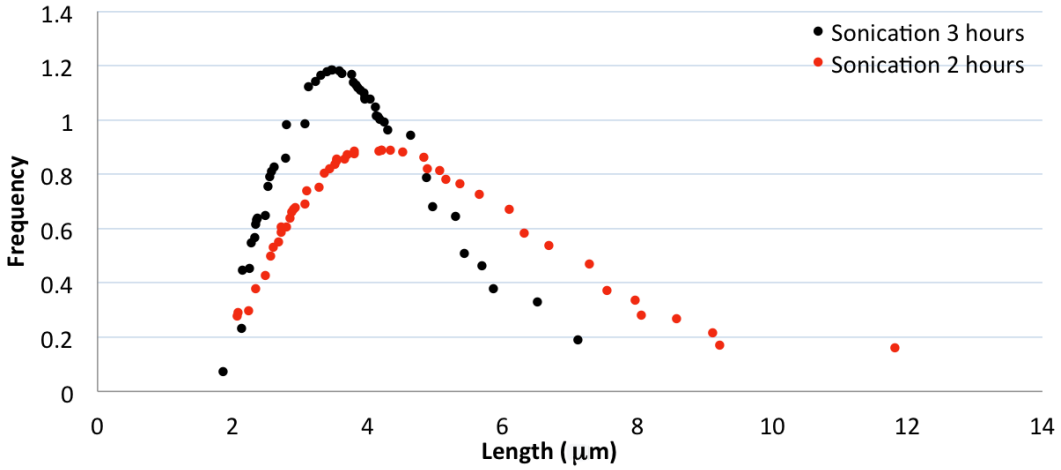

Figure 4.12: Differential length distribution of MWCNTs sonicated for 2 h and 3 h.

Both samples were kept on an ice bath during the sonication.

After the dispersing process, samples of both dispersions were analysed using an SEM microscope. Ten images of each dispersion were taken at two different magnifications (≈4000 x and 9000 x). These images were used to calculate the size distribution of CNTs in each dispersion.

The images were processed using Inkscape software. Five nanotubes were randomly chosen from each image and the size of each tube was calculated. The size of fifty tubes were collected for each dispersion. Using these fifty points the frequency distribution of the nanotube size in each dispersion was calculated.

The size frequency of the nanotubes length can be fitted with a log normal model [138]. The log normal distribution is a function of the mean value (μ) and standard deviation (σ) of the natural logarithmic of the tubes length. This

differential probability density function is given by

$$f(ln(L)) = \frac{1}{\sigma\sqrt{2\pi}} e^{-(\frac{ln(L)-\mu}{\sigma})^2}, \tag{4.2}$$

where L is the size of the nanotubes.

The cumulative frequency distribution shown in Figure 4.11 was calculated from the contribution of each observed length. This plot shows that for longer sonication times, the change in tube size is smoother than the one occurring for shorter sonication periods. This means that difference between the nanotubes lengths is smaller. This translates into smaller nanotube sizes with prolonged sonications.

The frequency distribution in Figure 4.12 shows the amount of nanotubes with a specific length. In the case of the solution sonicated for 3 h, the majority of tubes will have an average length of 3.4 µm and for a sonication time of 2 h the average length of the tubes is 4.16 µm.

These results were expected, as longer sonication times will tend to damage the tubes for longer periods. This method can be used to quantify the damage to the tubes, but more importantly is a parameter to decide the appropriate sonication time when shorter or longer tubes are needed.

4.4 Conclusions

The aim of this chapter was to develop a methodology to disperse carbon nanotubes. As produced, CNTs form different types of networks; in the form of carpets or forests, they grow perpendicularly to the surface of a substrate and parallel to each other. When produced as fibres or films, the CNTs grow in an entangled network of bundles. In order to change the CNTs from these configurations into a printable solution, which remains stable through the printing process, it is necessary to de-bundle the nanotubes and stop their re-aggregation.

To avoid toxic materials, which would limit the potential applications of this dispersion, water was chosen as the solvent. As CNTs are not miscible in water some type of functionalisation is necessary to disperse the nanotubes. Surfactants provide a non-covalent functionalisation that does not alter the nanotube structure and renders them miscible in water. For this reason adding a surfactant to the dispersion and applying sonication was the route used to disperse the CNTs.

Sodium dodecylbenzene (SDBS) was used as the surfactant. Two important

factors were identified which indicate that the amount of surfactant used in the dispersions should be minimised. The fist one is related to the toxicity of SDBS; although for humans it is very low, the excessive use of this molecule could have an impact on the environment if it is not adequately disposed or treated. But perhaps the main factor to consider is the effect it has on the electric and thermal properties of the nanotubes.

From a thermoelectric point of view, it is important to maintain the electrical conductivity of the nanotubes after the dispersion has been deposited on a substrate. In water, the surfactant molecules attach to the walls of the nanotubes through the polar head whilst the hydrophilic tail of the surfactant prevents the CNTs from re-bundling. When the dispersion is deposited on a substrate and water evaporates, the nanotubes form a network but the surfactant molecules remain attached to them. The charge flow within this network occurs by charges travelling through the nanotubes and hopping between adjacent tubes. The surfactant molecules affect this charge flow by creating electric barriers for the charges and this increases the overall resistance of the CNT network.

The minimum amount of surfactants in a dispersion is defined by the quantity required to fully disperse CNTs. It was shown that when a suspension of CNTs is not homogeneously disperse it leads to non uniform depositions. To find the optimum ratio of SDBS to CNTs, different surfactant concentrations were studied and it was found that above 0.5 wt% of surfactant agglomeration of CNTs starts to form. This concentration defines the balance point between the maximum surfactant absorbed by the CNTs and the depletion interaction which cause the nanotubes to collapse towards each other as the osmotic pressure applied by the surfactant molecules accumulates.

Part of the dispersing process involves sonicating the suspension to separate the nanotube bundles and introduce the surfactant molecules. This process has several effects on the dispersion and in the nanotubes. After sonication, the initial concentrations change due to the evaporation of the solvent and the destruction of CNTs and surfactant molecules. Using thermogravimetric analysis this effect was characterised. The technique presented in this chapter allows the quantification of the exact mass proportion of CNTs and SDBS in a dispersion.

To produce electrically conductive tracks of nanotubes from CNT dispersions, it is necessary to reach the percolation threshold during the deposition. This requires a high concentration of nanotubes in the dispersion which translates into longer sonication periods. This prolonged sonication cause more damage

to the nanotubes. To investigate how the this process affects the CNTs, the length of the nanotubes was analysed using SEM images of samples sonicated for three and four hours, this is the time required to disperse solutions with more than 1 wt%. The results revealed that after 3 h of sonication the CNTs are 20 % shorter than the ones sonicated for 2 h. This result shows the importance of using a minimum sonication time, as shorter nanotubes will create a CNT network with more nanotube junctions, which means the charges will have to travel across more potential barriers.

In the following sections, the dispersion methodology presented in this chapter will be used to explore the thermal and electrical properties of conductive tracks made from CNT dispersions. As this process can be used regardless of the initial morphology of the nanotubes, the dispersions can be produced from carpets, films, forest or from doped CNTs. This presents an advantage in the fabrication process of thermoelectric devices as both types of conductors required (p-type and n-type) can be fabricated using the same process. This will be examined in the following sections.

5

Carbon nanotube N-doping

The fabrication of a thermoelectric device requires a flow of positive and negative charges through the thermoelectric elements. To achieve this, a donor of positive charges is joined with an electron donor. Normally this n-type, p-type configuration is formed using two completely different materials or by doping a p-type source to convert it into a negative donor. In this chapter the conversion of carbon nanotubes from p-type to n-type semiconductors through doping is investigated. The objective of this procedure is to use the dispersion technique developed in Chapter 4 to prepare an n-type water based carbon nanotube dispersion that can be deposited using a printing method.

5.1 Nitrogen doping

The sign of the Seebeck coefficient of as-produced carpets of MWCNTs has been measured to be positive. This would imply that the majority of carriers are holes produced by the semiconducting nanotubes. The value of the thermoelectric power is the net effect of the contribution of metallic and semiconducting tubes. It has been suggested that the large p-type behaviour exhibited is not an intrinsic property of the CNTs but rather an effect caused by oxygen doping.

Collins et al. showed that after introducing CNTs into a vacuum chamber and removing the oxygen, it was possible to shift the sign of TEP from positive to negative. The sign would reverse again when oxygen was reintroduced and the nanotubes became again hole-doped due to the electron affinity of the adsorbed oxygen [186]. Air exposure of the nanotubes will immediately dope them with oxygen, which can only be completely desorbed after heating the CNTs above 420 K in vacuum conditions. Theoretical calculations of the density of states of an oxygen-doped nanotube showed that oxygen mainly affects the semiconducting tubes. The electronic orbital of oxygen can slightly overlap the one of the nanotubes becoming a source of positive carriers or holes [187].

Several doping strategies to reverse the p-type behaviour of the CNTs have been explored. Treatments with alkali-metals have been used to improve the conductivity of the tubes and to induce a change of carrier density from holes to electrons [188]. The main problem with this technique is that it is not air-stable which makes it unfeasible for many practical applications. An alternative doping method consist of exposing the nanotubes to reducing agents like $NaBH_4$ [189].

Another approach is to coat the nanotubes with molecules which work as electron donors. Aromatic amines, polymers like polyethyleneimine (PEI) and other organic dopands can be used to wrap the nanotubes and use the lone-pair of electrons in the nitrogen atoms to shift the Fermi energy level into the conduction band changing the nanotube conduction from p-type to n-type [190–192]. This is achieved through a physisorption process in which the polymer molecules around the nanotubes attach to other polymer molecules. The drawback from this kind of methodology is that in the case of MWCNTs, the n-doping occurs only in the external nanotubes leaving the internal walls as p-type semiconductor. Thus the total conduction is a combination of the p- and n-type section, which reduces the electrical conductivity [193].

Nitrogen is used as a carbon nanotube dopant because the small size of the atom allows it to be introduced into the CNT lattice. Several configuration in which the nitrogen atoms can be incorporated into the CNT lattice have been discussed, but in the principal ones the nitrogen atom can substitute one carbon atom (graphitic), sit in-plane within the carbon framework in a five-fold ring (pyrrole-like) or in a weaker two-coordinate fashion sharing electrons with only two carbon atoms (pyridine-like) [194]. It is possible to grow nitrogen doped CNTs using a the standard catalytic CVD procedure and adding a nitrogen source to the CNT precursors.

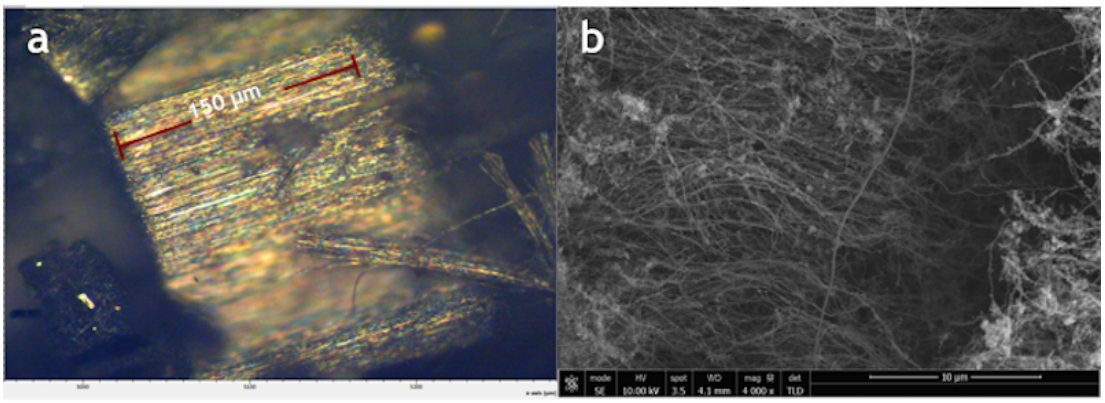

Figure 5.1: A) Optical microscope image of a nitrogen doped CNT carpet. B) SEM image of the same N-doped sample. The nanotubes are longer than 15 µm.

Different research groups have reported the synthesis of CNTs which showed the three types of N-doping using a CVD technique and different nitrogen sources [179, 195–197]. Besides being air-stable, one advantage of it is that opposite to the process describe above, not only the external tubes are doped, but also the inner ones [198]. This increases the overall carrier density of the network, which could lead to higher TEP values.

5.2 Experimental results

Two types of nitrogen-doped carbon nanotubes were grown through CVD deposition. The synthesis process was carried out in a similar way to the one described in Section 4.2.1 for the synthesis of MWCNTs. Pyrazine and benzylamine were used independently as nitrogen sources. These were mixed with ferrocene and toluene to form the CNT feedstock solution. This mixture was introduce into the first zone of furnace at 453 K at a rate of 7.2 ml/h. A flow of 0.7 l/min of argon was used as carrier gas to move the evaporated mixture into the central section of the furnace which was heated at 1033 K.

For the CNTs grown using pyrazine, the feedstock solution was made with a 3 % mass fraction of ferrocene, 67 % of toluene and 30 % of pyrazine. The feedstock for the benzylamine synthesis was a mixture of 5 % mass fraction of ferrocene, 75 % of toluene and 20 % of benzylamine. In both cases the synthesis lasted 4 h.

This synthesis process produces nonotubes longer than 15 µm and possibly up to 100 µm. The diameter of the tubes is 7.2 nm. Figure 5.1 is an image taken using an optical microscope and another one taken using an SEM. They show the

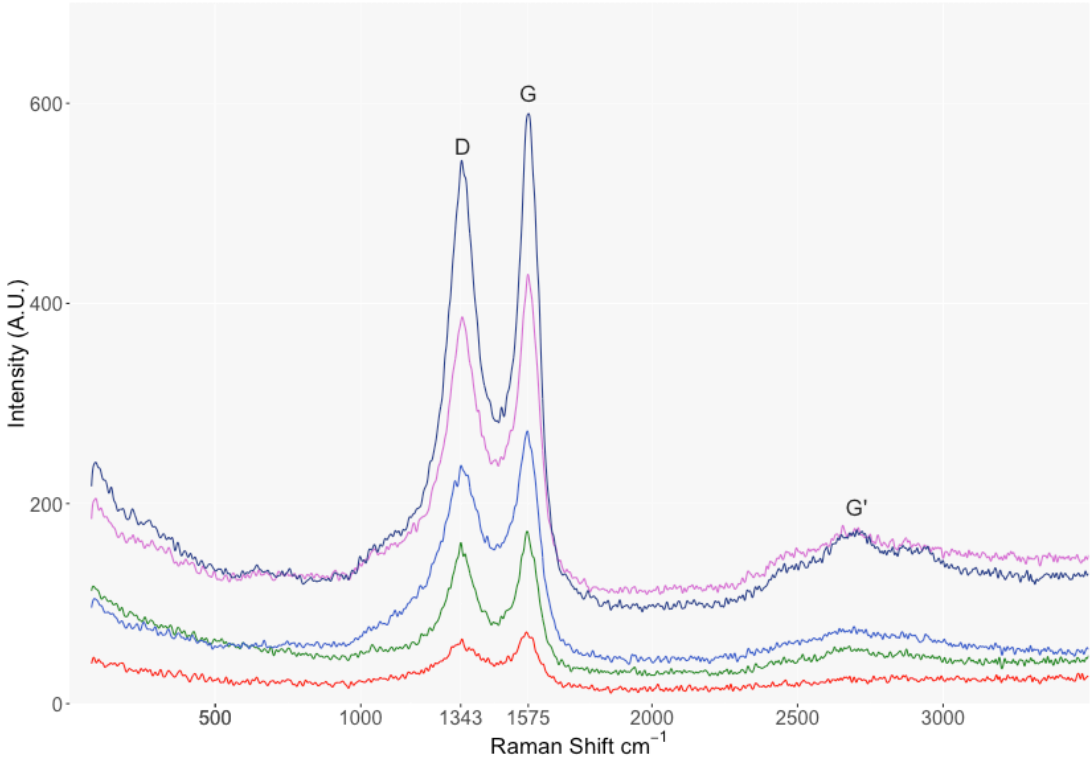

Figure 5.2: Raman spectra of the CNT carpets grown using 20 % mass fraction of benzylamine as nitrogen source.

size and shape of the carpet grown using pyrazine. The SEM image shows the carpets are formed by entanglements of long tubes. The diameter was calculated using the average of 100 tubes taken from SEM images taken in 10 different points in the sample. The length of the tubes synthesised with benzylamine falls within the same range as the pyrazine tubes. The average diameter is larger, 13.4 nm which is consistent with the results reported previously for N-doped CNTs grown under similar conditions [199].

To confirm the presence of nitrogen in the nanotubes, Raman analysis was performed using a Raman microscope (Bruker Senterra). The measurements were carried out using a 532 nm laser at 5 mW. The microscope was set to a 20 X magnification.

Figure 5.2 shows a representative Raman spectra for 5 different points of the benzylamine carpet. The plot shows two maxima at 1343 cm^{-1} and 1575 cm^{-1}. The broadening of the two peaks causes the signals to overlap. The spectra does not show the radial breading modes (RBMS) in the low frequency region between 100 cm^{-1} and 400 cm^{-1}. It has been proposed that in the case of MWCNTs this could mean that the sample contains mainly tubes of large diameter (inner diam-

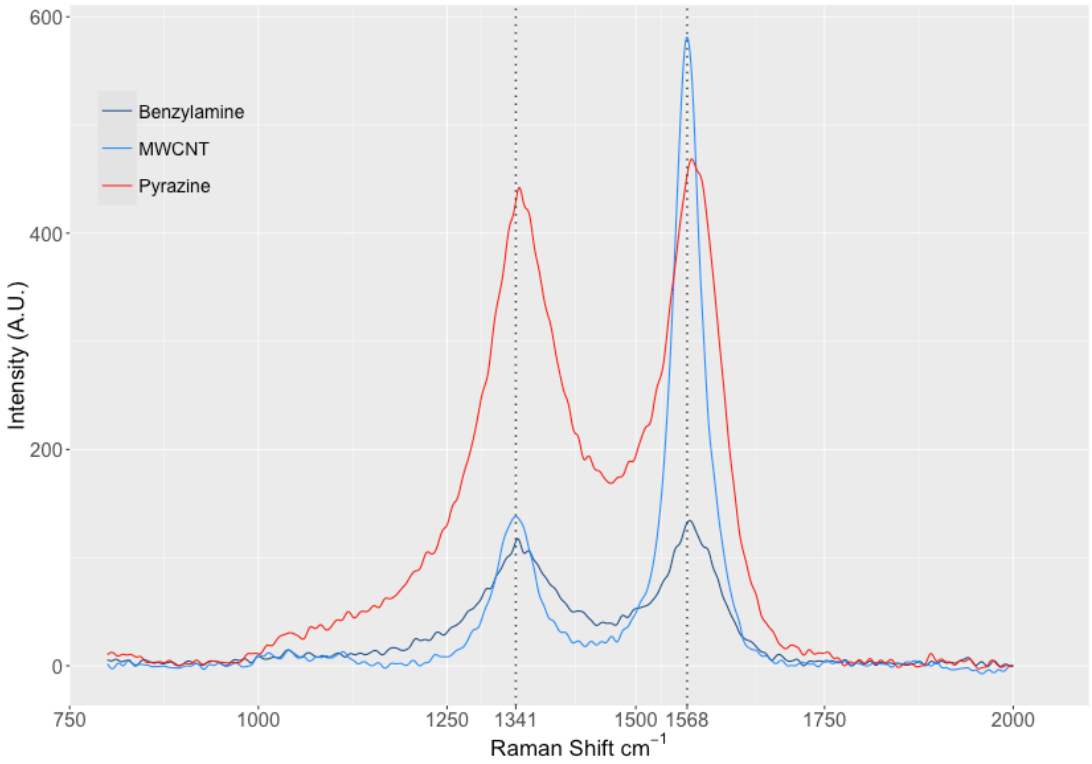

Figure 5.3: Raman spectra of as grown MWCNT and N-doped MWCNT carpets grown using benzylamine and Pyrazine as nitrogen sources.

eter larger than 2 nm) [200]. In the high frequency region, close to 2700 cm^{-1} the G′ band is visible. This band has been associated to the purity of the nanotubes, with higher intensities signifying MWCNT with long range order. In the case of this sample, the intensity of the band is low, which could mean that the tubes contain certain degree of impurities [201, 202].

A deeper evaluation of the CNT doping can be done comparing the Raman spectra of as grown MWCNT carpets and the spectra of the doped CNTs. Figure 5.3 combines the Raman signals of two N-doped CNT samples and one MWCNT carpet. It is clear that the peaks are well defined for the non-doped sample. The base line has been removed from the plot and the frequency range restricted to the region of interest.

The peak at 1548 cm^{-1} corresponds to the G-band which is characteristic in the spectra of sp^2 hybridised carbon. It is arises from the tangential vibration mode of the carbon atoms along the nanotube plane. This band is well defined when there is a good formation of graphitised carbon [203, 204].

At 1341 cm^{-1} the D-band or disorder peak appears. This is an inactive mode which appears when breaks in the symmetry of the carbon lattice occur. It is thus

commonly associated with the degree of defects in the nanotube structure, which can happen through functionalisation, kinks or conversion of the sp^2-hybridised bond into an sp^3-hybridisation [139]. Although it is not possible to associate the intensity of this band to an specific type of defect, the intensity of this band reflects the crystallinity of the sample.

For the benzylamine and pyrazine samples the size of this band indicates the presence of doping. The D-peak broadens and merges with the G band. It forms a shoulder which extends to the frequency $1000\,\mathrm{cm}^{-1}$. This shoulder is not present in the non-doped samples. It has previously been pointed out that the deconvolution of this band can only be made by introducing extra bands to the spectra. In particular the I band, which has also been observed in disordered graphitic carbons. This extra band is the main constituent of the observed shoulder and in this case accounts for the symmetry breaks caused by the introduction of nitrogen in the carbon lattice [205].

Research made in N-doped CNT samples shows that an estimation of the amount of nitrogen doping can be done by calculating the intensity of the D/G band ratio. An increasing absolute value of this ratio would mean a higher nitrogen content in the sample [204, 205]. For the samples analysed in this work, the average D/G ratio corresponding to the non-doped MWCNT carpets was 0.26 ± 0.021. For the carpets grown with using the pyrazine as nitrogen source the D/G ratio was 0.886 ± 0.047 and for the N-doped CNTs grown using benzylamine 0.882 ± 0.06. This results indicate that there is almost no difference in the amount of nitrogen doping achieved with both precursors.

Using both types of N-dope MWCNT carpets, water-based dispersions were prepared with the method described in the previous chapter. 1 % mass fraction of N-doped CNTs were dispersed with 0.25 % mass fraction of SDBS in distilled water. The mixture was sonicated for 2 h whilst immersed in an ice bath. Samples prepared with the resulting dispersions were deposited on glass slides and Raman analysis was performed as described.

Figure 5.4 presents the results of the Raman analysis on the N-doped solutions. The results confirm that the doping is still present after the dispersion process. The broaden D-peak can be seen centred around $1347\,\mathrm{cm}^{-1}$ together with the G-peak at $1576\,\mathrm{cm}^{-1}$. It is worth noting that the intensity of D-band has a reduced magnitude compared to the intensity of the carpets D-band. This is an indicator that the introduction of SDBS and the sonication have an effect on the crystallinity of the nanotubes.

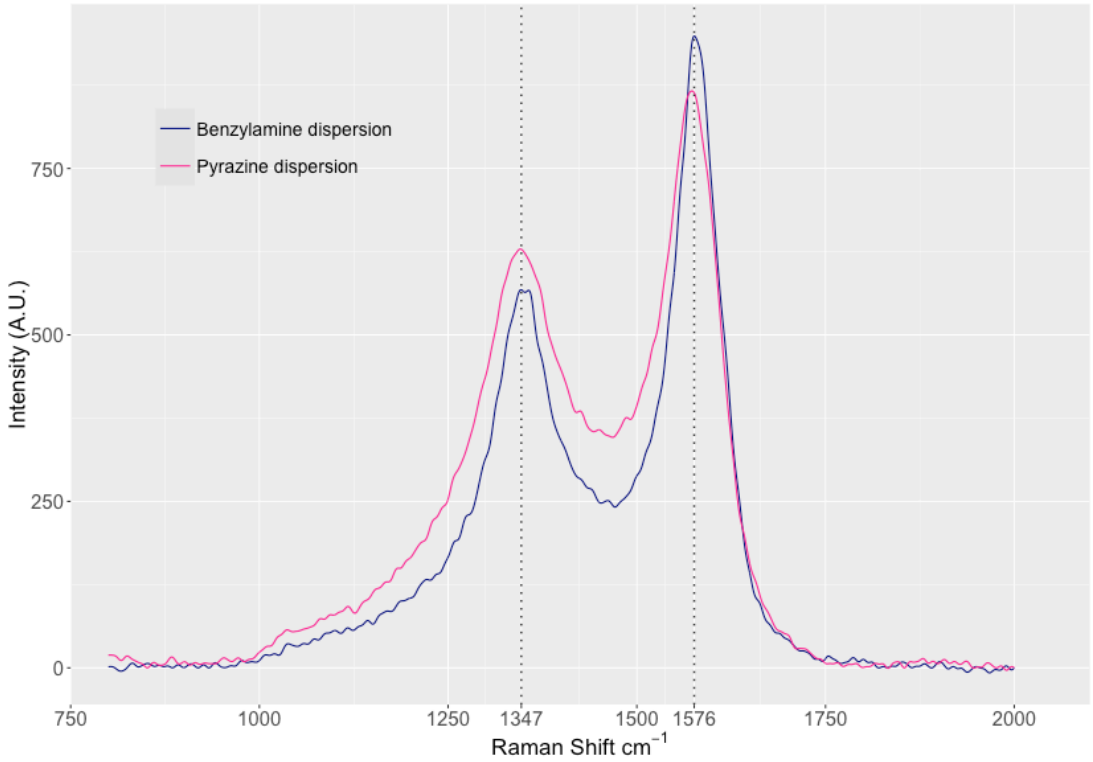

Figure 5.4: Raman spectra of N-doped MWCNT dispersions prepared using MWCNT carpets grown with pyrazine and benzylamine.

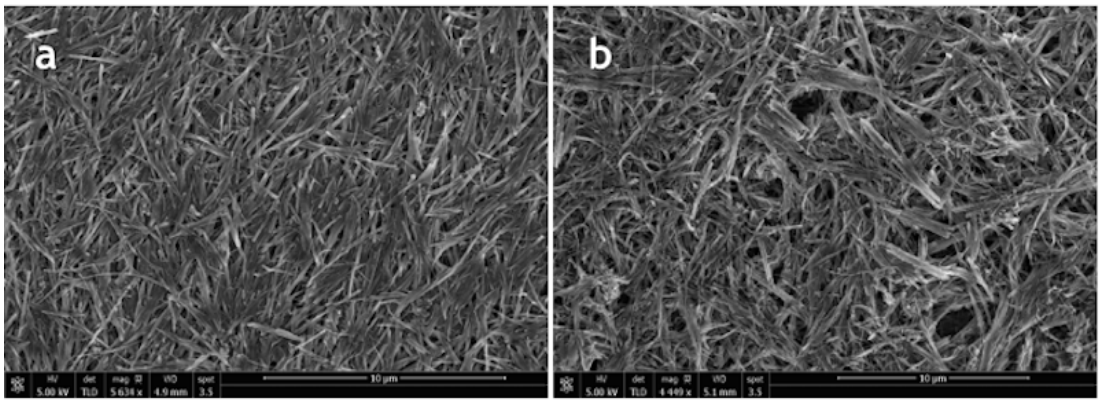

Figure 5.5: SEM image of N-doped MWCNT dispersions. The image show the size of the nanotubes has been considerably reduced. A) Solution prepared using the carpets grown with bezylamine. B) Solutions prepared with the carpets grown unsing pyrazine.

The ratio of the D/G peaks has also decreased its value to an average of 0.5838 ± 0.016 for the benzylamine dispersion and 0.73 ± 0.009 for the pyrazine dispersion. These results indicate that the dispersion process has a smaller effect on the solutions prepared with the carpets grown using pyrazine or that the functionalisation caused by the surfactant has an effect on the intensity of the D-band.

This can be better appreciated in the SEM image shown in Figure 5.5. It is possible to see that the pyrazine dispersion has a higher amount of SDBS on the surface of the nanotubes and that the nanotubes are stacked in thick bundles. The benzylamine dispersion shows less surfactant on the surface and nanotube bundles with smaller diameters.

As expected, the nanotubes in both dispersions have been severely reduced from their original size. This can be related to enhanced breakage during the sonication process, which could have been promoted by the defects present in the nanotube walls. As discussed, the breaking of the nanotubes starts at the sites where the defects are present.

The Seebeck coefficient of the dispersions was measured using the set-up developed in Chapter 2. This measurement was performed to corroborate that the main type of carriers in the dispersion were electrons. Both types of N-doped dispersions were deposited on Kapton tape and dried for one day at 323 K. Once the dispersion was completely dried, the film was peeled from the Kapton tape and placed in the Seebeck measurement set-up using silver paint to fix it to the stage holder.

The measurements were performed in air in the range 293 K to 323 K. It has been shown that the Seebeck coefficient does not change over this temperature range. The measurements performed on 3 samples of pyrazine dispersions resulted in a Seebeck coefficient of $(-43 \pm 3)\,\mu V/K$. A similar measurement on the benzylamine dispersion yielded $(-36 \pm 4)\,\mu V/K$.

These results confirm that the majority of carriers in the samples are electrons and thus the conversion from the intrinsic p-type to n-type behaviour has been achieved. Compared to the values of the Seebeck coefficient measured on the CNT films grown by the CVD process, the value of the Seebeck coefficient of the N-doped dispersions is smaller. Nevertheless, using the synthesis procedure investigated in this chapter can lead to the fabrication of a thermoelectric device made entirely of carbon nanotubes.

5.3 Conclusions

In this chapter the successful synthesis and characterisation of n-type nanotube films was presented. The water-based films were produced using the method described in Chapter 4. These films are necessary for the fabrication of CNT-based TE devices. The films were produced using nitrogen doped CNTs dispersed in water.

The doping of nanotubes was achieved using two different nitrogen precursors during the synthesis of the nanotubes. CNTs produced with pyrazine and benzylamine were characterised to compare the doping effect of these components. This type of CNT doping introduces free electrons into the lattice network, transforming the intrinsic p-type characteristic of CNTs into an n-type conduction which is based on electrons. This doping method was preferred over acid doping to avoid the use of toxic materials and because the resulting material is stable in air.

An analysis of SEM images of the nitrogen doped CNTs showed that both precursors produced nanotubes of similar diameters. CNTs with diameters of 13 nm corresponding to large diameter tubes were observed in samples from pyrazine and benzilamine. These results were confirmed by the absence of RBMs in the Raman spectra of the samples, which indicates the presence of large multiwalled nanotubes.

The Raman spectra of the doped nanotubes was used to evaluate the doping of samples produced with each nitrogen precursor. Higher intensities of the D band were observed in the nitrogen doped nanotubes when compared to the intensity of the D band of non-doped nanotubes. The high intensity of the D band present in the doped nanotubes indicate a higher amount of disruption in the nanotubes lattice. These disruptions were associated to the inclusion of nitrogen into the nanotube walls.

The characteristic G band in the Raman spectra of CNTs was also observed in the pyrazine and benzylamine samples. The calculation of the ratio between the intensity of the D and G band (D/G ratio), which gives an estimate of the amount of nitrogen in a sample, showed that both types of precursors produced nanotubes with a similar amount of nitrogen. The ratio in the two types of materials was found to be D/G= 0.88.

Water-based dispersions of nanotubes were prepared using CNTs produced with pyrazine and benzylamine. Analysis of the Raman spectra of these samples proved that the doping remained after the dispersing process in both types of

samples. The D/G ratio decreased by 10 % in both samples. This is consistent with a higher amount of defects introduced to the nanotubes by the addition of surfactant and sonication.

Finally, a confirmation that the main type carriers in the nitrogen doped samples are electrons was made by measuring the Seebeck coefficient of the samples. It was found that both types of samples had negative coefficients which correspond to n-type semiconducting nanotubes. The samples synthesised using pyrazine had a higher Seebeck coefficient than the samples produced using benzylamine. This result and the magnitude of the D/G ratio indicates that the N-doped nanotubes produced using benzylamine should be the CNTs used in the n-type films for TE devices.

This methodology completes the preparation of the components for the printed thermoelectrics. The next section will concern the evaluation of the transport properties of the n-type and p-type films produced from water-based CNT dispersions. This final characterisation section will be used to evaluate the performance of the CNT thermoelectric devices.

6

Carbon nanotubes thermal properties

To complete the characterisation of the thermoelectric properties of carbon nanotube films made from water dispersions and the ones synthesised using the direct spinning method, it is necessary to measure the thermal conductivity of these materials. This chapter will focus on the development of set-up and a methodology to measure the thermal conductivity of films. This equipment will then be used to compare the thermal conductivities of the different CNT films used in this work.

The measurement of the thermal conductivity of carbon nanotube fibres and films may be considered to be a research topic in itself. There are several complications arising from the measurement of this property in a quasi one-dimensional material. The size of the sample makes it very susceptible to background noise signals and heat losses. It is also hard to place the necessary heaters and thermocouples on the sample. There is no standard method or equipment to measure this property. A very common method used by some groups is the 3ω which consist on applying an AC current at a frequency ω to a thin stripe of metal deposited on the sample. Measuring a third harmonic voltage across the heater at two different frequencies, the thermal conductivity of the sample can be derived. This method is very useful because there is almost no radiation losses associated to it. The drawback is that it requires lithography for the preparation of the

samples [206–208].

Steady state methods are routinely used to measure thermal conductivity because they are relatively easy to implement. They require a reference sample and careful consideration of all the possible heat losses. These could arise from convection through the surrounding medium, heat conduction through the system wires and thermocouples or heat losses by radiation. All of them should be minimised or considered when the calculations are made. There are several variation of this method, but all of them calculate the thermal conductivity through the correlation of power inserted to the sample and the temperature change produced [209, 210].

6.1 Thermal conductivity set-up

In this section a set-up to measure the thermal conductivity of CNT fibres and films is developed. The set-up uses a steady state method called parallel thermal conductance (PTC) [209]. It is based on the work of Jakubinek et al. who used it to measure the thermal conductivity of MWCNT yarns [211]. The method consist on calculating the conductance of the sample (K_s) by measuring the background conductance (K_b) or conductance of the set-up and the parallel thermal conductance, which is produced by the sample contacts and the blackbody radiation from the sample.

Figure 6.1 shows a diagram of the set-up. It consist of a sample holder connected to the a Keithley 2700 multimeter which continuously measures the temperature of the sample. The sample holder is also connected to a Keithley 2200 power source which is used to set the temperature of the sample. Both devices are controlled through a LabVIEW program that acquires and records the data.

To minimise the heat losses in the system through radiation and convection, the sample is placed inside a stainless steel high vacuum chamber. The chamber is connected to a LEYBOLD TURBOVAC TW 250S turbomolecular pump which is controlled by a LEYBOLD CONE.TROL 200 and a COMBIVAC IT23 display system. The rough vacuum needed to start the pump is supplied by an Edwards XDS10 pump. The pressure of the system is monitored by a THERMOVAC pressure sensor connected directly to the chamber. This system is capable of achieving a vacuum of 6×10^{-3} mbar.

The sample holder shown in Figure 6.2.(a) is formed by a 120 kΩ resistor that works as a heater and an aluminium block. The sample is placed on top

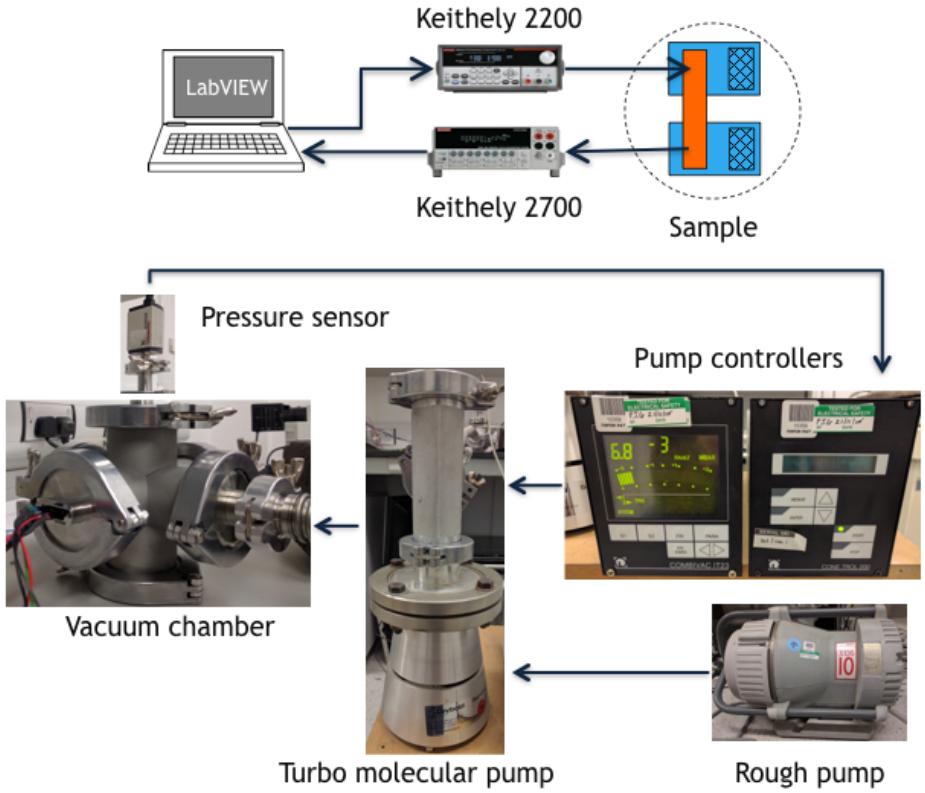

Figure 6.1: Diagram of the set-up to measure thermal conductivity using the PTC method.

of the heater and the aluminium block using silver paint. The metal block is connected thermally in series to the chamber and works as a heat sink. The heater is used to produce the temperature sweeps required by the steady state method. To monitor accurately the temperature gradient across the sample, one high precision thermistor (PT1000) is connected directly to the side of the sample which is in contact with the heater and another thermistor is placed on the aluminium block. To avoid any inaccuracies in the measurement related to the wiring of the system, the change in resistance of the thermistors is measured using a four probe resistance measurement available on the Keithley 2700 multimeter.

Once the sample is placed in the holder, it is introduced into the vacuum chamber and the vacuum system is started. When the pressure reaches 6×10^{-3} mbar, the power supply applies a constant current to the heater. This increases the temperature of one side of the sample. The LabVIEW software is programmed to control the current (I) in order to maintain a constant power input (P) to the sample. When the temperature gradient (ΔT) reaches an equilibrium, the temperature is increased again by inputting more power according to $P = I^2R$, where R is the internal resistance of the heater. This process is repeated in steps

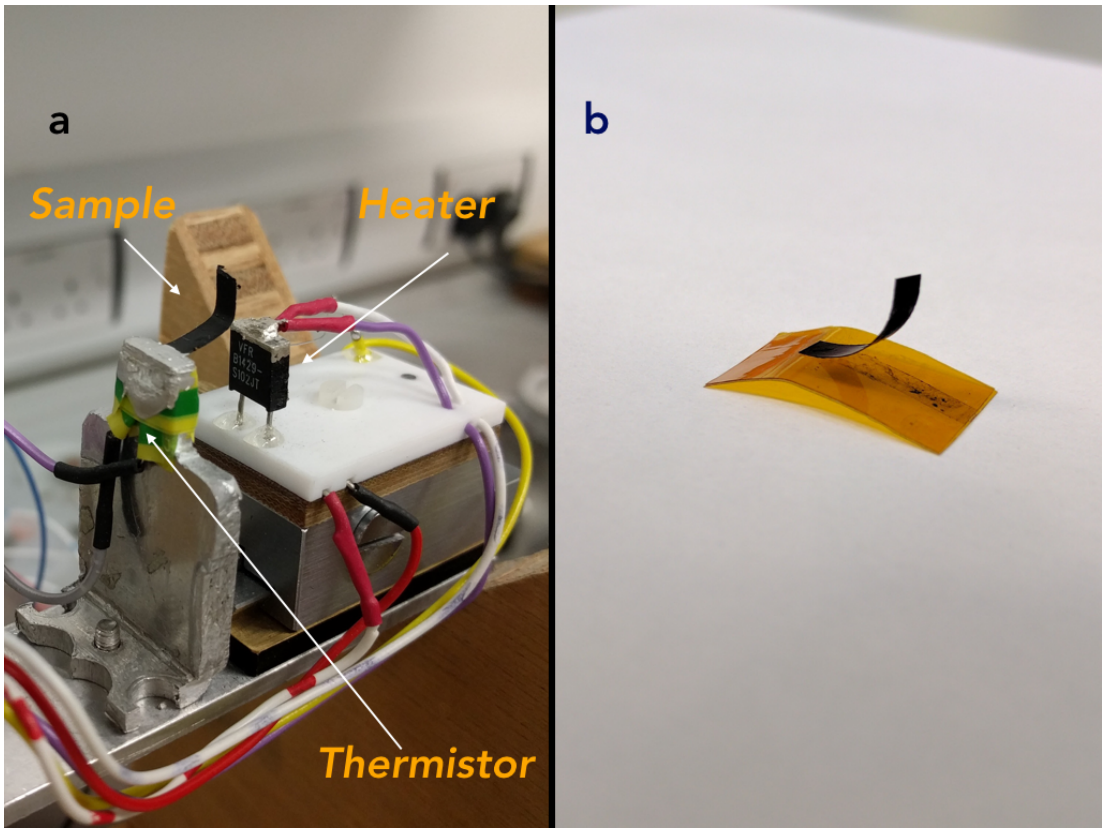

Figure 6.2: a. Image of the thermal conductivity set-up holder. **b.** Peeling process of a CNT film made from a water-based dispersion.

of 50 W until the temperature gradient reaches 40 K.

The process inside the chamber is illustrated in Figure 6.3. The temperature of the hot side, represented by the red curve, requires time to stabilise after each power increment. The inset in Figure 6.3 shows the temperature rapidly increasing until it reaches a stable value. The temperature in the side of the aluminium block, black curve, remains very close to the ambient temperature. The small temperature increase observed on the aluminium block is caused by the radiation process inside the chamber. The magnitude of this process was quantified and subtracted during the calculations.

In order to account for all the thermal process occurring inside the chamber and subtract them from the calculation of the thermal conductance of the sample, the experimental method requires to be run three independent times. In first run, the system is activated with the camber empty. Using the results from this measurement, the background conductance (K_b) caused by the radiation of the heater is calculated. A second experimental run is performed with the sample in place, but connected only to the hot side of the holder. This measurement is

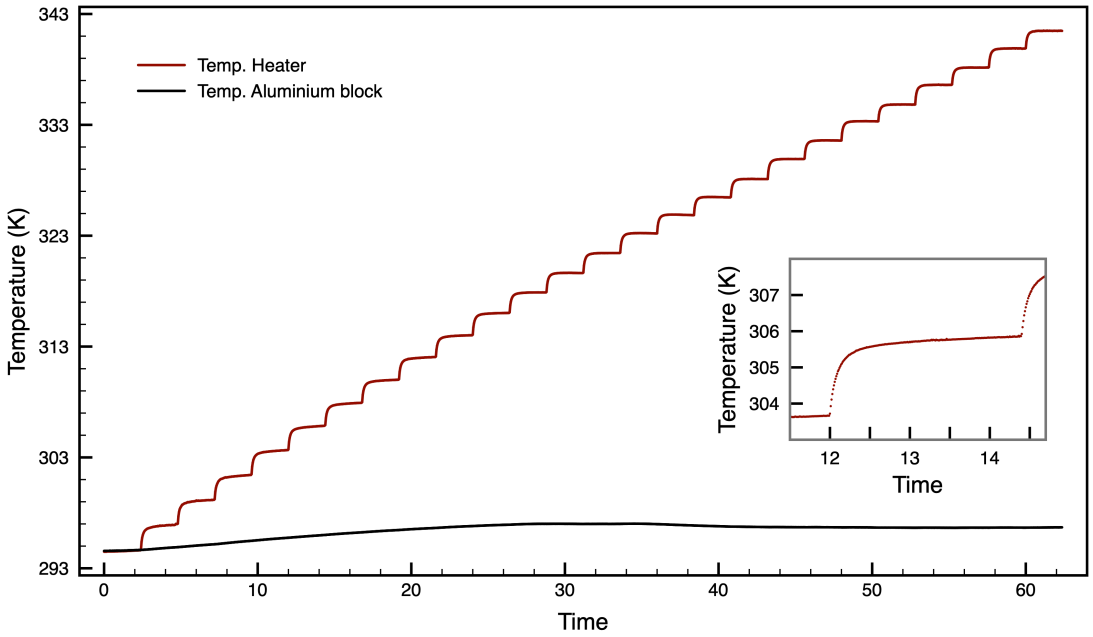

Figure 6.3: Plot of the temperature change in the hot side and in the aluminium block during a experimental run. The inset in this figure shows the detail of one temperature step. The equipment requires time to stabilise the temperature to a constant value.

used to measure any heat loss due to the radiation of the sample and following the nomenclature of Jakubinek et al. is recorded as the thermal conductance K_3. In the third final run, the sample is connected to both sides of the holder and the total conductance is calculated K_t.

The conductance of the sample is thus given by

$$K_s = K_t - K_b - \frac{1}{2}(K_3 - K_b), \tag{6.1}$$

where K_s is the conductance of the sample, K_t the total conductance, K_b the background conductance and K_3 the conductance associated to the radiation of the sample.

Plotting the change in the temperature gradient against the power supplied to the sample, the thermal conductance can be calculated. Figure 6.4 shows the results of a typical 3-step experimental run for one CNT material. The slope of each line corresponds to thermal conductances of the chamber, of the sample connected only to the heater and the total conductance. It is important to keep the calculation of the slope in the linear region of the curve as the thermal conductance is linearly related to the power applied ($P = K_{t,b,3}\Delta T$). Deviations from this linearity could occur at high values of the temperature gradient. These deviations would be associated to uncertainties in the measurement or increased

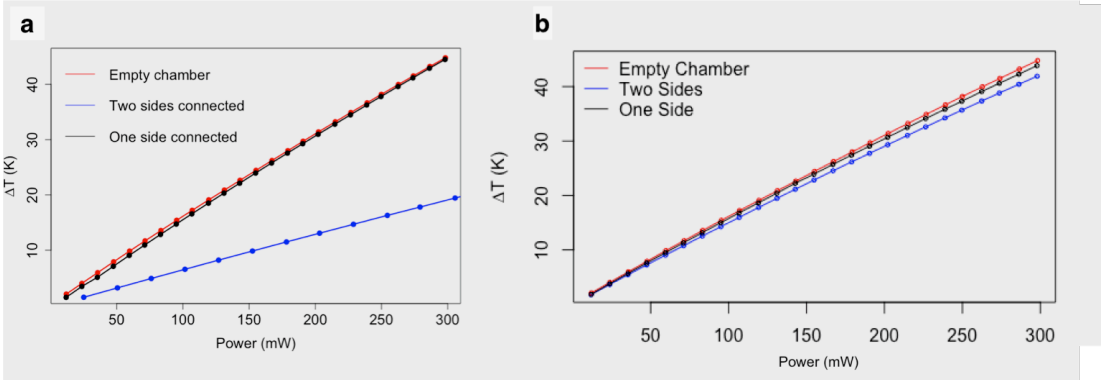

Figure 6.4: a) Plot of temperature gradient against the power supplied to a thick sample. **b)** Plot of temperature gradient against the power supplied to a thin sample.

heat losses. For this reason the temperature gradient was kept below 50 K.

An analysis of the plots in Figure 6.4 reveals that the temperature gradient in the empty chamber always has the highest value. This is because the only heat reaching the aluminium block comes from the radiation of the heater. When the sample is connected to one side and the heat cause by the radiation of the sample reaches the aluminium block, the value of the temperature gradient is lower in comparison to the one recorded for the empty chamber. When the sample is connected to both sides, the heat flow to the heat sink is at is highest, which results in the lowest temperature gradient from the three experimental runs.

The thickness of the sample is important when performing the measurements, as the process just described is enhanced when thicker samples are analysed. Comparing the results of two samples with different dimensions in Figure 6.4. The thicker sample in Figure 6.4.(a) produces a higher difference between the three temperature gradients. When the sample is very thin, there is almost no difference between the gradients, which complicates the calculations. The system is thus restricted by the dimensions of the sample.

The system was calibrated measuring the thermal conductance of a thin film of copper. The dimensions of the film are shown in Table 6.1. The thickness of the sample was measured using a Mitutoyo 293-330 digital micrometer with a 0.001 mm resolution. A summary of the results of the calibration experiments is presented in Table 6.1.

Knowing the dimensions of the sample and its thermal conductance, the thermal conductivity κ can be calculated,

$$\kappa = \frac{K_s A}{L}. \tag{6.2}$$

Table 6.1: Experimental parameters and results of the thermal conductivity measurement of copper.

Dimensions		
Length	0.95	mm
Width	7	mm
Thickness	31.97	µm
Cross sectional area	2.24×10^{-7}	m^2
Conductance (mW/K)		
K_b: background	6.35	
K_3: sample's radiation	6.31	
K_t: total	15.71	
K_s: sample	9.39	
Thermal conductivity	403.83	$W\,m^{-1}\,K^{-1}$

where A is the cross sectional area of the sample and L the length. The thermal conductivity measured for copper was $403.83\,W\,m^{-1}\,K^{-1}$, which is very close to the nominal value of $401\,W\,m^{-1}\,K^{-1}$.

The thermal conductivity of different carbon nanotube based materials was evaluated. Films produced by direct spinning from a catalyst CVD furnace were cut to exact same dimensions using a laser cutter. To evaluate the effect of the alignment of the tubes on the thermal conductivity a batch was cut parallel to the general tube alignment and another batch was cut in a perpendicular direction. To increase the thickness of these samples, several films from the same batch where placed at the same time on the holder.

CNT films prepared from water based dispersions were also analysed. Dispersion with a 2 % mass fraction of MWCNT and 1 % mass fraction of SDBS were prepare and deposited on Kapton tape. They were dried for one day at 323 K and peeled from the tape as see in Figure 6.2.(b) Two types of films were prepared, one batch of nitrogen doped films and one batch of non-doped MWCNTs.

The accurate characterisation of the dimensions of the sample is fundamental for the calculation of the thermal conductivity. In the case the CNT films, the most difficult dimension to measure is the thickness of the film. To address this problem, an optical profilometer Wylko NT3300 was used. The samples were placed on a glass slide and rinsed with acetone to flatten them. Measurements of the sample's profile were performed in different sections of the films. Figure 6.5 shows an image of the profile of one sample. The heat map is the profile of a whole section of the film and the histogram shows the thickness distribution of

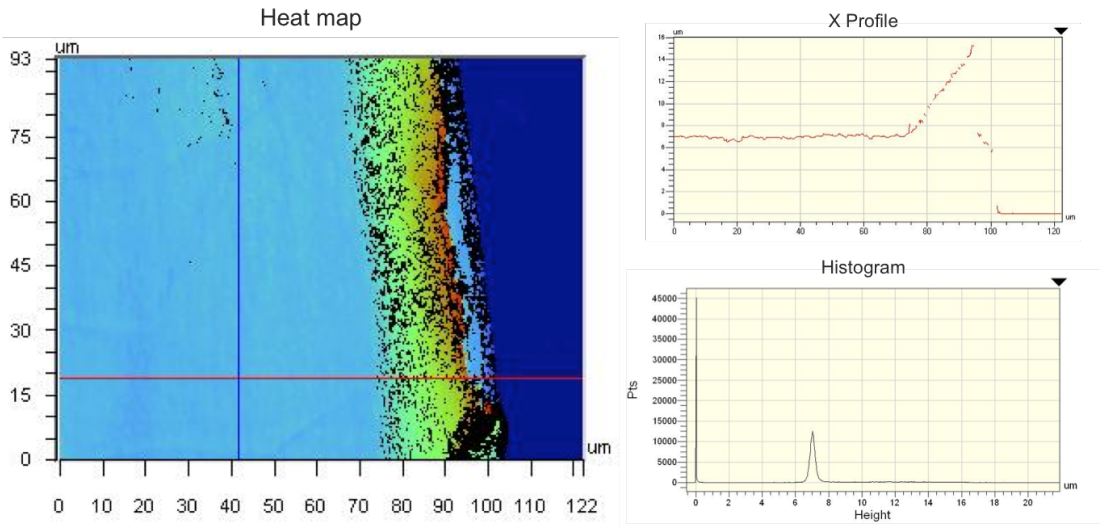

Figure 6.5: Measurement of the thickness of a film using a profilometer

the region.

Table 6.2: Results of the thermal conductivity measurements on different CNT samples.

Material	Nanotube alignment	Thermal conductivity $\mathrm{W\,m^{-1}\,K^{-1}}$
CVD film	perpendicular	75.9743
CVD film	parallel	123.2593
MWCNT dispersion	random	6.9691
N-doped dispersion	random	0.8621

Table 6.2 summarises the properties and the result of the measurement performed on the different materials. The films grown directly from the CVD method have a better thermal conductivity that those prepared from the water based solutions. This can be explained by taking into account that the size of the tubes decreases during sonication, which introduces more nanotube junctions. This junctions are phonon barriers which decrease the thermal conductivity of the sample. In the same way the introduction of SDBS particles into the nanotube network work as phonon and electron barriers.

From the two types of CVD films, those which were cut along the main direction of alignment of the tubes show a slightly higher value than their counterparts. The effect of the direction of alignment on the thermal conductivity is not as strong as the introduction of external particles in the CNT network, but the results suggest that the thermal conductivity is enhanced when the nanotubes are aligned in the direction of the heat flow. This occurs if the main contribution to the thermal transport are phonon travelling along the length of the tube.

Comparing the nanotube films made from the water dispersions. Those with N-doped CNT have a lower thermal conductivity than the non-doped films. This can be attributed to the amount of defects on the carbon lattice which are introduced during the doping process. As discussed in the previous chapter, the introduction of nitrogen breaks the symmetry of the lattice, which causes the scattering of phonon and electrons. It is worth noting that very low thermal conductivities are desirable in thermoelectric materials. Therefore, producing films from carbon nanotube dispersions is a promising approach for thermoelectric applications.

6.2 Thermal stability

Using a custom-made 4-probe set-up, the maximum working temperature of the CNT films made from dispersions was evaluated. The system consisted of a sample holder for a 4-probe measurement which was introduced into a furnace. The temperature of the furnace was controlled using a labVIEW program. The program also recorded the resistance of the sample during the experimental run. All the experiments were made in air.

In the first experiment, the sample was heated to 523 K and then it was cooled down. After the sample reached ambient temperature, it was heated again to 523 K. Figure 6.6 shows a typical curve of resistance versus temperature of a CNT sample. During the first heating, the resistance of the sample decreases with the increase of temperature. When it cools down, the resistance of the sample remains at this value. During the second heating and cooling the resistance displays almost no changes.

The decrease in resistance during the first heating can be attributed to the evaporation of water and some other particles present in the sample. This is an annealing process that can be reverted if the sample is left exposed to oxygen and water molecules from the environment.

In a second experimental run which was designed to evaluate the maximum working temperature of a conductive CNT track. A pre-annealed sample was heated until the resistance of sample dropped. Figure 6.7 shows the result of this experiment. The sample is stable until ≈623 K when the carbon nanotube network starts to disintegrate until it is broken and there are no paths for the flow of electrons. This occurred at approximately 723 K.

This result is important because it shows that when the CNT conductive

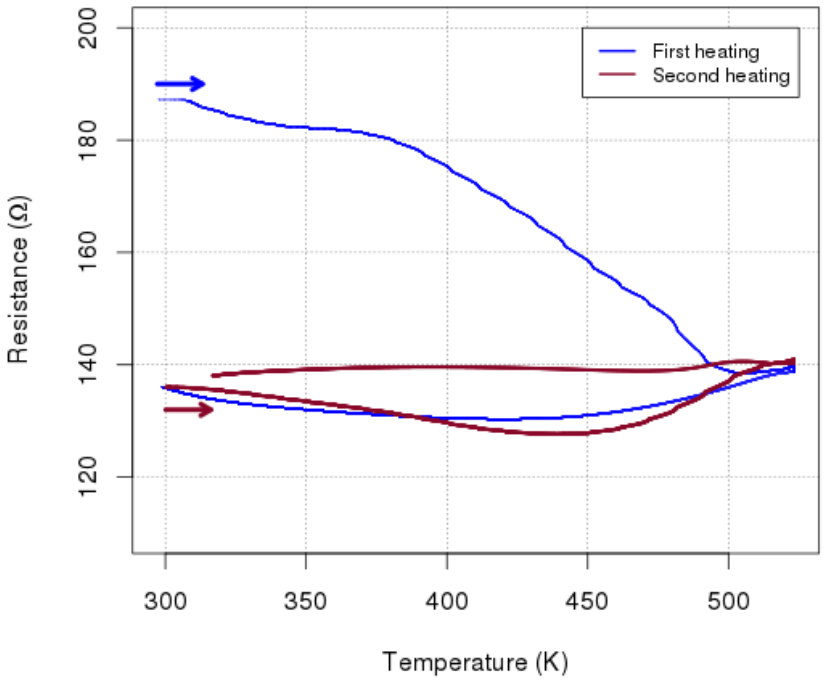

Figure 6.6: Change of resistance with temperature of a CNT sample.

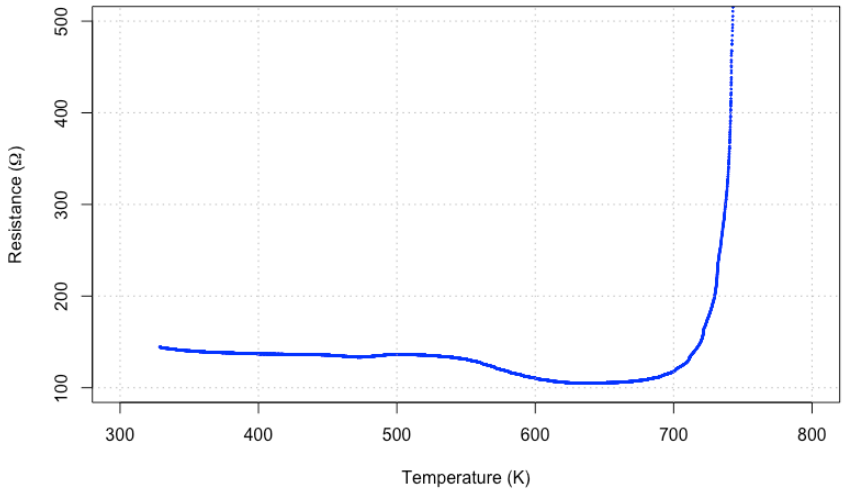

Figure 6.7: Breaking temperature of a CNT conductive track made from a water-based dispersion.

tracks are used in electronic or thermoelectric devices, the maximum temperature at which they can be exposed is close to 670 K.

6.3 Conclusions

The methodology used in this chapter to calculate the thermal conductivity consists in measuring the thermal conductance of the sample to correlate it to the thermal conductivity of the material. The nature of the measurement requires the quantification of the heat losses associated to the background radiation of the system and the radiation of the sample itself. To measure this two quantities it is necessary to carry out two independent experimental runs. The first one with an empty chamber is used to calculate the background radiation. The second one with the sample connected only to the heat source serves to calculate the sample's radiation. Finally a third measurement with the sample connected to the heat source and heat sink gives the total conductance of the system from which the conductance of the sample can be obtained.

This method is a steady-state technique in which the temperature of the heat source is slowly increased in small steps. Between each temperature increase, the temperature must reach an equilibrium and this increases the amount of time needed per experimental run. Each sample requires three experimental runs for one measurement of thermal conductivity. Furthermore, as the measurement has to be performed in high vacuum to minimise the heat losses associated to radiation and eliminate heat losses caused by convection, the overall time required to characterise one sample is more than one day. This can be considered the main disadvantage of this method compared to other techniques like the 3ω method that only require a few minutes per measurement. But the principal advantage of the parallel thermal conductance technique is that it requires almost no sample preparation and can accommodate different sample morphologies.

As shown in the first part of this chapter, the thermal conductivity of films of different thickness and single fibres of a few microns can be measured. The sample holder of the set-up allows for different lengths and a range of morphologies. Once the sample is cut to the required dimensions it only needs to be attached to the holder using conductive silver paint. The thermal conductivity of the silver paint is not known, but it is assumed to be higher or at least the same order of magnitude than the thermal conductivity of the samples that were analysed.

If the thermal conductivity of the material used at the interface between the

heat source, the heat sink and the sample had a low thermal conductivity; the heat transferred from the heater to the sample would be lower and the same would occur at the sink side. The radiation at the interface would also have a higher value than with a highly thermally conductive material. The fact that the thermistor that measures the temperature at the heater and at the sink side is placed at the interface and not in direct contact with the sample or the heat sink/source, guarantees that the heat losses associated to the thermal conductivity of the interface materials are accounted for. The only effect that this would have is on the amount of power needed to increase the temperature at the heat source side. The heat losses attributed to the radiation of the silver paint are quantified during the thermal conductance background measurements.

The limits of the method are given by the thermal conductance of the sample. As it was shown by the experiments, when the conductance is very low, i.e. it approaches the background thermal conductance, the conductance of the sample approaches the uncertainty of the measurement. Further experiments to determine the minimum value that can be measure are needed.

The accuracy of the thermal conductivity measurement depends highly on the correct determination of the cross sectional area of the sample. In the case of CNT and other films, two methods have been presented. The thickness of metallic samples like aluminium, copper, constantan films can be quickly determined using a micrometer, but for more heterogeneous samples like CNT films or fibres, the cross sectional area has to be determined by other means. Focused ion beam microscopy can be used to find the thickness of films and diameter of fibres, scanning electron microscopy can be used to measure the diameter of fibres and profilometry could be useful to the determine the thickness of films. In any of these methods, an average of the dimensions has to be used in the calculation of the thermal conductivity. This introduces an uncertainty in the measurement that cannot be avoided in the case of these materials.

The results from the thermal stability measurements carried out in CNT films show the highest temperature at which this material can operate in air if it is used to conduct electricity. The resistivity of the samples analysed starts increasing when the sample is exposed to more 700 K in air. This is consistent with the results obtained from the thermogravimetric analysis in Chapter 4. After 570 K amorphous carbon, small diameter nanotubes and defective tubes start degrading. When these material burn, they deteriorate the carbon nanotube network causing an irreversible increase in the overall resistivity of the material.

If the CNT network is exposed to lower temperatures than the breaking point, the effect is completely different. During the first exposure to high temperatures, the resistivity of the sample decreases. This is attributed to an annealing process that removes water particles and residues of the CNT synthesis. This effect can be partially reversed if the sample is exposed again to an ambient environment, as re-absorption of molecules will occur. This result points to the possibility of pre-treating the CNT films prior to it use in thermoelectric devices. But as pointed out, it will only have a permanent effect in the conductivity of the material if it is not exposed to oxygen.

Summary of characterisation techniques

The objective of this work was to study the thermoelectric properties of carbon nanotube based macroscopic materials, in particular carbon nanotube films. These materials were selected because they can be fabricated using scalable processes that can be brought into real world applications. To study the thermoelectric properties of these materials it is necessary to characterise three key parameters. The Seebeck coefficient, the thermal conductivity and the electrical conductivity.

An important contribution of this work was the development of characterisation equipment that can be use to asses the properties of different types of films. The methods and equipment developed are not restricted to carbon nanotube based materials. In the first section of the dissertation, a set-up to evaluate the Seebeck coefficient of films was fabricated and calibrated using constantan as a standard material. The results obtained with this equipment are consistent with the ones reported in literature.

The Seebeck coefficient of three types of CNT films was analysed. Films spun directly from a CVD furnace showed the highest values reaching up to $70\,\mu V/K$. The measured value of the Seebeck coefficient of MWCNT-based films prepared from water-based dispersions was $60\,\mu V/K$. These values are comparable to the Seebeck coefficient reported for other thermoelectric materials like some antimony-based thermoelectrics and to the best conductive polymers like poly(3,4-ethylenedioxythiophene)(PEDOT) or doped polyaniline (PANI).

Using the Seebeck coefficient measurement set-up, the type of carriers present in the semiconducting CNT films was determined. The positive values measured on as-produced CNT films are attributed to an electronic transport dominated by positive carriers, making these materials p-type semiconductors. In the case of constantan and nitrogen doped CNT films, the values measured at room temperature were $-40\,\mu V/K$ and $-43\,\mu V/K$ respectively, showing that electrons are the main type of carriers in these materials making them n-type semiconductors.

Two prototypes of thermoelectric devices were manufactured. These devices proved that energy harvesting using CNT-based thermoelectric devices is possible. These two first prototypes had problems associated with the manufacture technique. As the prototypes were hand-made, some of the junctions at the interface of the n-type and p-type legs resulted in poor electrical connections which highly increased the resistivity of the affected thermoelectric cells. These cells had to be removed from the finalised devices.

These results were used as the starting point for the design of a new process which would improve the manufacture of CNT-based TE devices. Printing technologies, were envisioned as fast and scalable fabrication methods. A process of this nature required the CNTs to be dispersed into a printable solutions. As CNTs are produced as a network of entangled nanotubes, a methodology to disperse them had to be developed. To avoid restricting the possible applications of these dispersions, water was chosen as the solvent.

As produced, CNTs are not dispersible in water. The different methods available for the production of water-based CNT dispersions were discussed and the functionalisation of CNTs through surfactants was selected as the dispersing methodology. Sodium dodecylbenzene (SDBS) was used as surfactant in the preparation of CNT dispersions. As the surfactant attaches to the surface of the nanotubes they render the CNTs dispersible in water, but at the same time, this molecules work as barrier for the free movement of electrons. For this reason, and analysis to determine the lowest amount of surfactant necessary to achieve stable dispersions was carried out.

Carbon nanotubes produced as carpets were disperse in water using ultrasonication. Once the nanotubes were dispersed, centrifugation and thermogravimetrical analysis were carried out to determine the concentration of nanotubes and surfactant in the dispersions. The results of this analysis showed that only 0.25 % mass fraction of SDBS is necessary to disperse carbon nanotubes in water. It was also found that the highest ratio of surfactant to CNT that should be used is 1:1 as higher ratios did not improve the dispersing process.

The effect that ultrasonication has in the nanotubes was also explored. Using SEM images, an analysis of the length of the nanotubes of dispersion sonicated for two and three hours was carried out. This analysis showed that the majority of CNTs sonicated for three hours were 20 % smaller than the ones sonicated for two hours. This proved that a minimum sonication time has to be used in order to minimise the damage to the nanotubes, as shortening or destruction of the

walls has an effect on the electrical and thermal properties of the nanotubes.

In order to fabricate a TE device made completely with carbon nanotubes, it was necessary to make CNT dispersions in which the main type of carriers were electrons. This was achieved by synthesising nitrogen doped carbon nanotubes carpets. These N-doped nanotubes were dispersed in water applying the same methodology used for non-doped CNTs. Two types of nitrogen sources were explored, benzylamine and pyrazine. The doping effect of these precursors was studied using Raman spectroscopy. Both types of N-doped CNTs presented similar spectra associated to the defects introduced by the nitrogen doping. To confirm that the main carriers were electrons, Seebeck coefficient measurements were carried out on these dispersions. The measurements in both types of samples resulted in negative Seebeck coefficients which confirmed the materials as n-type semiconductors.

As part of the characterisation process of the thermoelectric solutions, a set-up to measure the thermal conductivity of films was fabricated. The set-up was based on the measurement of the thermal conductance of the sample. It was demonstrated that the results obtained were in agreement with the values reported for the calibration samples. The thermal conductivity of the CNT films was found to be between $0.68\,\mathrm{W\,m^{-1}\,K^{-1}}$ for the N-doped films and up to $123\,\mathrm{W\,m^{-1}\,K^{-1}}$ for the CNT films synthesised using the direct spinning method.

The thermal resistance of the samples was evaluated by measuring the increase of resistance of the samples when they were subjected to high temperatures in air. When the temperature of the samples reached 700 K, the nanotube network started disintegrating leading to an increase in resistivity. This result showed that the operating temperature in air of a TE device made from CNTs should be kept below this point.

The final chapter of this work will focus on the development of a technique to print p-type and n-type carbon nanotube dispersions. These CNT solutions will be used to fabricate thermoelectric devices made purely with carbon nanotube based materials. The performance of this devices will be analysed using the techniques developed until this point.

7

Printed thermoelectric devices

7.1 3D printing system

The controlled deposition of carbon nanotubes dispersions was achieved using a custom-made 3D printer. The system is shown in Figure 7.1. It is the integration of a deposition system and a CNC machine that controls the position of the printer's nozzle. The printing head is formed by a TS5000DMP auger valve connected to a TS500R digital controller.

The system is integrated using the WIPC-NC NC USB controller software. Using the programming language G-code, the printer head can be positioned through coordinates (x, y, z) within the working area x =720 mm, y =420 mm and z =110 mm. The precision of the system is 30 µm.

An air pump supplies 500 kPa to the deposition system. The controller regulates the pressure supply to the auger valve. The opening of the auger valve is electronically controlled and it is synchronised with the positioning system using the CNC machine software.

The internal diameter of the valve's nozzle can be easily changed. Diameters from 0.06 mm to 1.55 mm can be selected. The diameter required will depend on the size of the pattern to be printed and the viscosity of the material. Due to

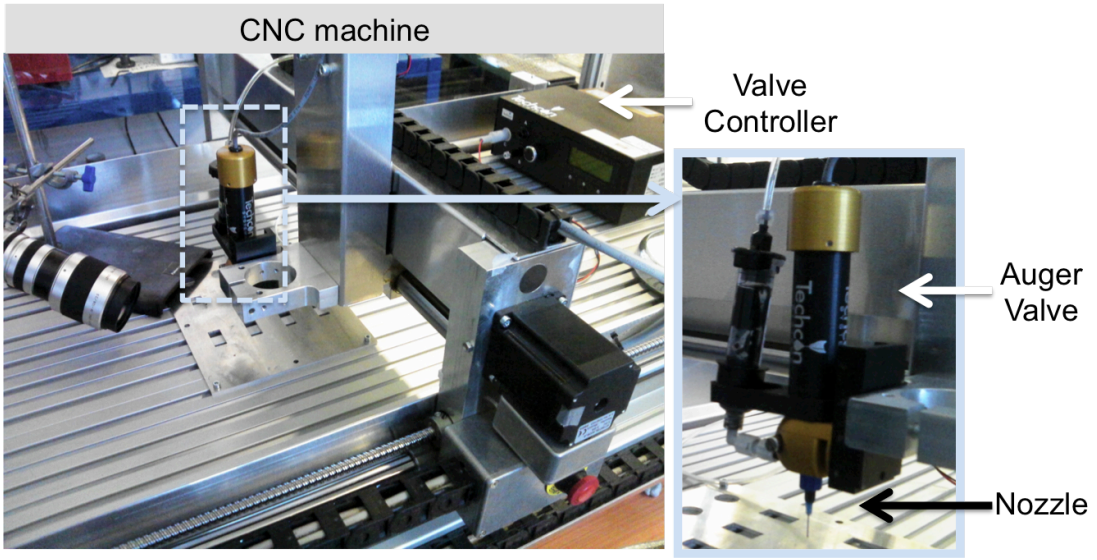

Figure 7.1: Custom-made 3D printing set-up for the deposition of CNT dispersions.

the fact that CNTs tend to form agglomerates, the use of nozzles with a diameter below 0.2 mm is restricted to dispersion with low CNTs concentration, i.e. under 1 % mass fraction of CNT's.

The deposition system allows for the control of three main parameters: the concentration of the dispersion (proportional to the viscosity), the pressure in the nozzle and the speed of deposition. This printing technique requires a continuous flow of liquid, but it must be properly selected according to the size of the nozzle and the viscosity of the fluid. The amount and speed of the liquid that comes out of the nozzle head is controlled by the pressure applied to the valve. Figure 7.2.(A) shows an image of four different pressure settings. At very low pressure the liquid is just collected at the nozzle's opening. As the pressure increases the flow starts until an optimum pressure setting is reached where a continuous flow is sustained.

The speed of deposition is manipulated by the movement of the CNC machine arm that holds the nozzle. The machine is capable of moving at a maximum speed of 4000 mm/min, the nominal speed being half of this value. The speed at which the arm moves must match the nozzle's output rate in order to achieve a good definition of the printed features. Figure 7.2.(B) shows the effect of 3 different speed depositions. The highest speed normally results in the best definition when a continuous flow method is used. In the samples shown in the figure, the highest speed rate available (200 % of the nominal deposition speed) had to be used in order to print a line with a thickness of 1 mm.

Another important consideration is the distance from the nozzle to the substrate. Using the automatic positioning of the CNC machine, the nozzle can

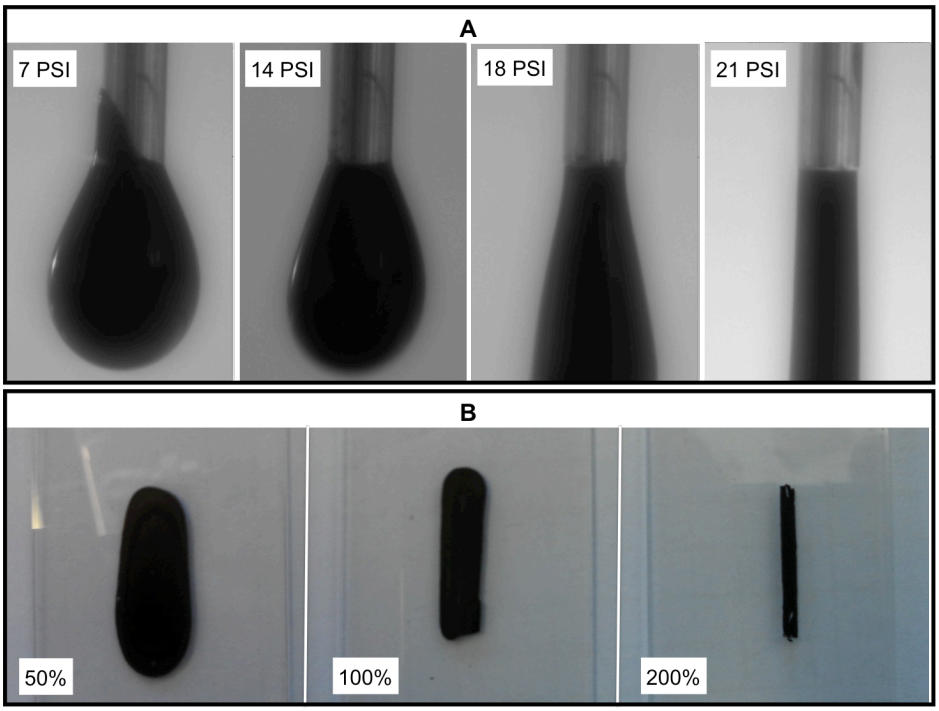

Figure 7.2: A) Formation of a continuous flow during the printing process of a CNT dispersion. B) Effect of the printing speed on the deposition process.

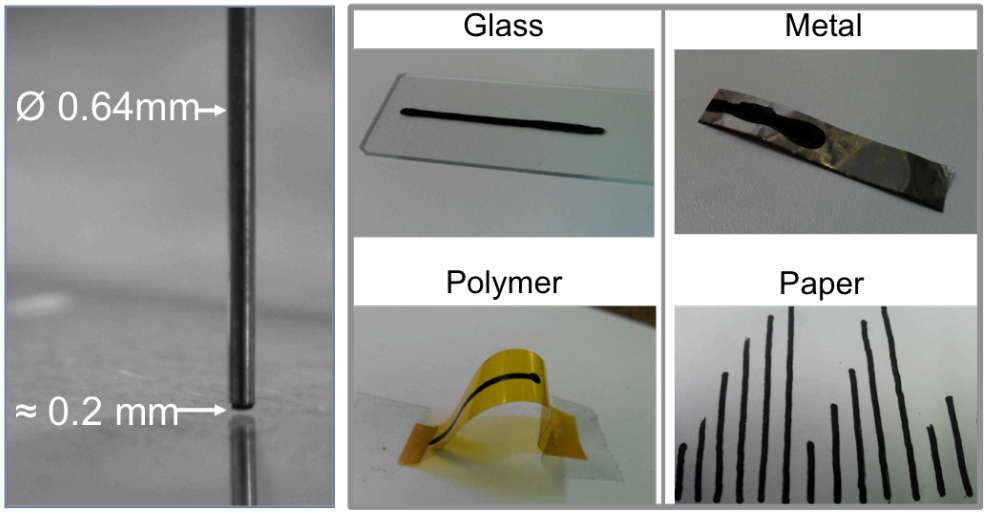

Figure 7.3: A) Working distance of a 0.64 mm nozzle. B) Printing of a CNT dispersion on glass, metal, polymer and paper.

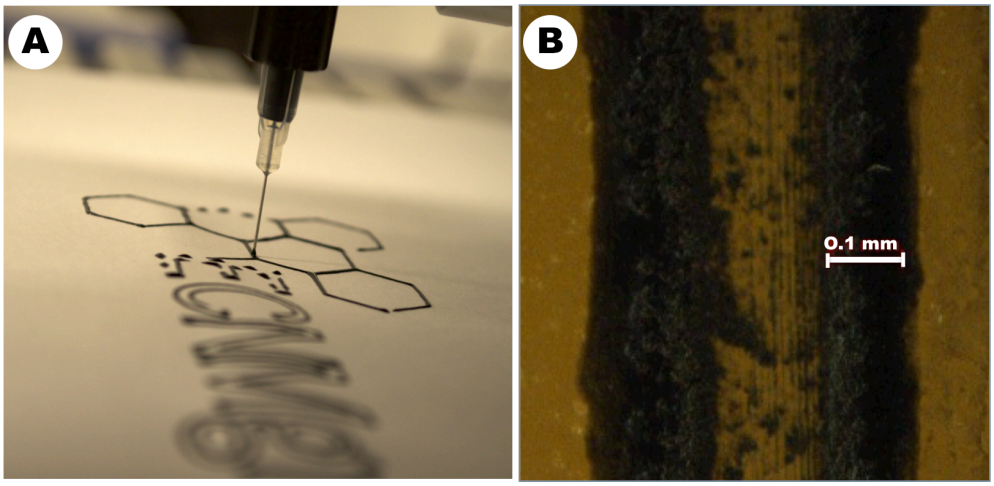

Figure 7.4: A) ECNM pattern printed using a CNT dispersion. B) Parallel stripes of CNT's printed on polymer. The pattern is made by 60 depositions.

be placed at any distance required. It was found that when the nozzle was positioned as close as possible to the deposition surface without putting them in contact, better results were achieved. By using a camera connected to the system's computer and a telephoto lens it was possible to determine that a good working distance was approximately 0.2 mm. This is illustrated in Figure 7.3.(A) for a 0.64 mm nozzle.

Using this printing system, CNT dispersions can be deposited on different materials. These include, metals, glass, paper and polymers (Figure 7.3.(B)). One key advantage is the possibility of printing on flexible substrates. Complex patterns like the one shown in Figure 7.4.(A) can be routinely printed. It is only necessary to have a CAD design of the pattern and input it into the system as G-code.

The system is also capable of printing very fine features. Figure 7.4.(B) shows the printing of two parallel stripes of 0.1 mm of thickness. Despite that such fine detail is achievable, the drawback is that the resistivity drops drastically when the amount the material deposited decreases. The pattern shown in the figure is formed by 60 layers printed on top of each other. It was necessary to print that many layers to achieve a conductive track with a resistivity of $\approx 100\,\Omega$.

An analysis of the interface between layers of CNT dispersions deposited on top of each other shows that there is a good contact between them. In Figure 7.5.(A) an image taken with an FIB microscope shows the cross sectional area of the deposition of one CNT layer. The thickness of this particular sample varies between 5.2 µm and 5.9 µm. In this image, the interface between the

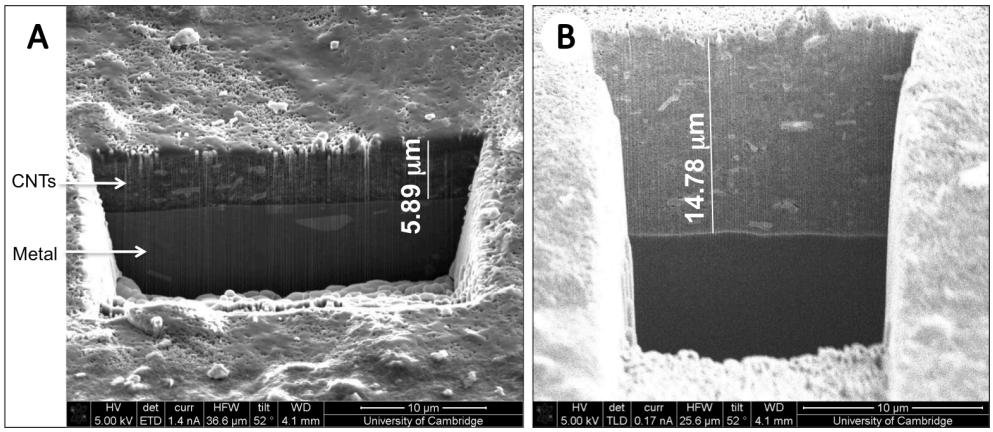

Figure 7.5: A) FIB image of the cross sectional area of a CNT dispersion formed by one deposition . B) Cross sectional area of CNT printed track formed by 3 layers.

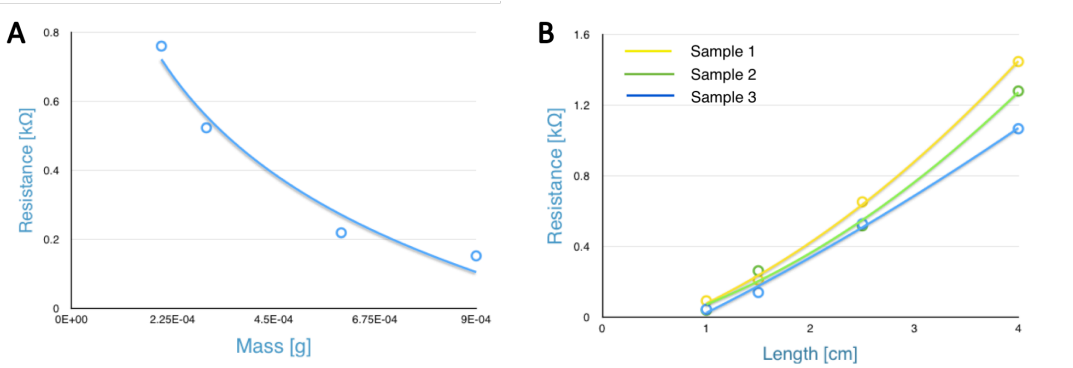

Figure 7.6: A) Plot of the resistance of a CNT deposition as a function of the weight and length of the sample. B) Plot of the resistance of 3 CNT depositions as a function of the length the sample. The three samples have a similar mass.

CNTs and the metal is evident. Figure 7.5.(B) shows the cross sectional area of a deposition of 3 CNT layers. As the image shows, there is no clear interface between the 3 depositions. This means that using this printing method a good CNT network can be constructed, which translates in materials that can be used for electronic transport.

To evaluate the change in resistance as a function of the number of depositions, samples formed by different number of layers where printed. The results are plotted in Figure 7.6.(A) As expected the resistance of the sample is inversely proportional to its mass. As the amount of material increases the nanotube network grows providing paths for the movement of carriers. This is true for all samples with the same length. In Figure 7.6.(B), the resistance of three samples of the same length and almost equal mass is plotted. The resistance of the material increases proportionally to the length in each sample.

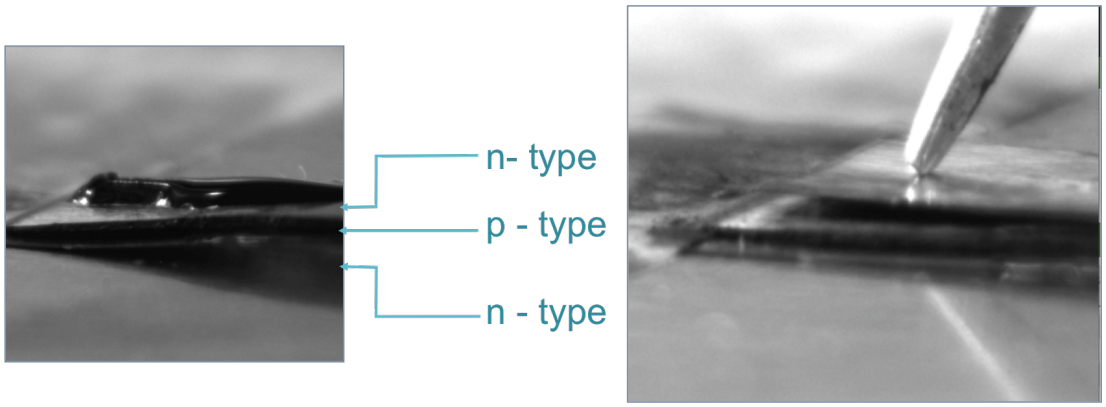

Figure 7.7: Thermoelectric device made of a printed CNT solution on constantan.

7.2 Printed thermoelectrics

Using this system, CNT-based thermoelectric devices were fabricated. In Chapter 3 the manufacture of devices made with CNT films and constantan was demonstrated. The first device made with the printer was formed by a leg of CNT-dispersion printed on a strip of constantan. One feature of the 3D printing machine is that the height of the nozzle can be precisely modified. This allows to create structures formed by layers of different materials.

A CNT dispersion with a 2 % mass fraction of CNT's and 0.5 % of SDBS was deposited on a stripe of constantan. The constantan leg was cut to 30 mm wide and 2 cm long. The deposition of the layers is shown in Figure 7.7. The constantan leg was covered by a layer of nitrocellulose which worked as a insulation layer between the CNT's and the constantan. A section of 2 mm was left uncovered to form the device junction. Before the CNT dispersion was completely dried, a second layer of insulation and constantan was placed on top to form a second thermoelectric junction. This process was repeated a third time to form the thermoelectric device shown in Figure 7.7 which consists of 3 junctions.

Table 7.1: Properties and performance of a thermoelectric device made with constantan and CNT dispersions.

	Resistance (Ω)	Seebeck coefficient(μV/K)		ΔT (K)	Voltage (mV)
		n-type leg	p-type leg		
1 layer	22	-40.3	65.2	5	0.9
3 layers	70	-40.3	65.2	5	2.4

The performance of the device was evaluated applying a temperature gradient to the junctions. The results are show in Table 7.1. Increasing the number of

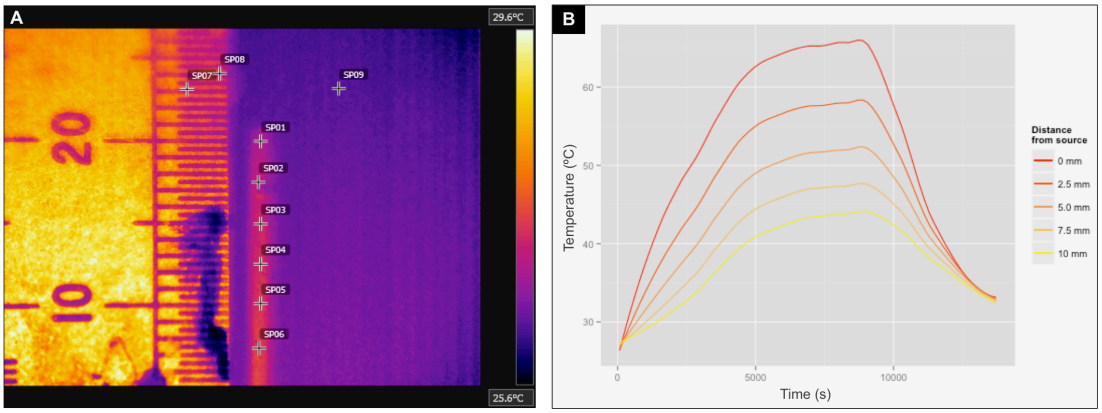

Figure 7.8: A) Heat map of a CNT track showing the temperature in different points. B) Plot of the temperature distribution in a the same CNT sample.

layers leads to a higher voltage output. The voltage increases linearly with the number of layers. In contrast to the hand-made device, there is no increase in resistance due to the contact at the junctions and therefore the current and voltage losses are reduced.

In order to the determine the optimum size of the CNT leg of a thermoelectric device, an analysis of temperature distribution along the CNT sample was performed. One of the ends of the sample was placed on a hot plate and the change of temperature at different distances from the source was monitored using a FLIR T450sc thermal camera. The layout of the experiment is shown in Figure 7.8.(A). The temperature of the sample was changed from 25 °C to 70 °C. The plot of the evolution of temperature versus time is shown in Figure 7.8.(B). At 75 °C the temperature difference between the heat source and the nearest point at 2.5 mm is 10 °C and the temperature difference between 10 mm and the source is 25 °C. This means that even very short samples will sustain a temperature gradient large enough to create a voltage difference.

To analyse the stability of a CNT thermoelectric device, three thermoelectric cells were fabricated using CNT dispersions. The p-type legs of the cells were made from a CNT dispersion of MWCNT with 2 % mass fraction of nanotubes. The n-type legs were prepared using a dispersion with the same concentration but processed with n-doped MWCNT's.

The voltage of the thermoelectric cells was recorded using a 2182A Keithley nanovoltmeter. The temperature gradient was calculated measuring the temperature at the hot junction and at the cold end of the TE cell. The results of the experiment are presented in Figure 7.9. In the first experiment (Figure 7.9.(A)), the samples were submitted to a temperature gradient of 40 °C. The tempera-

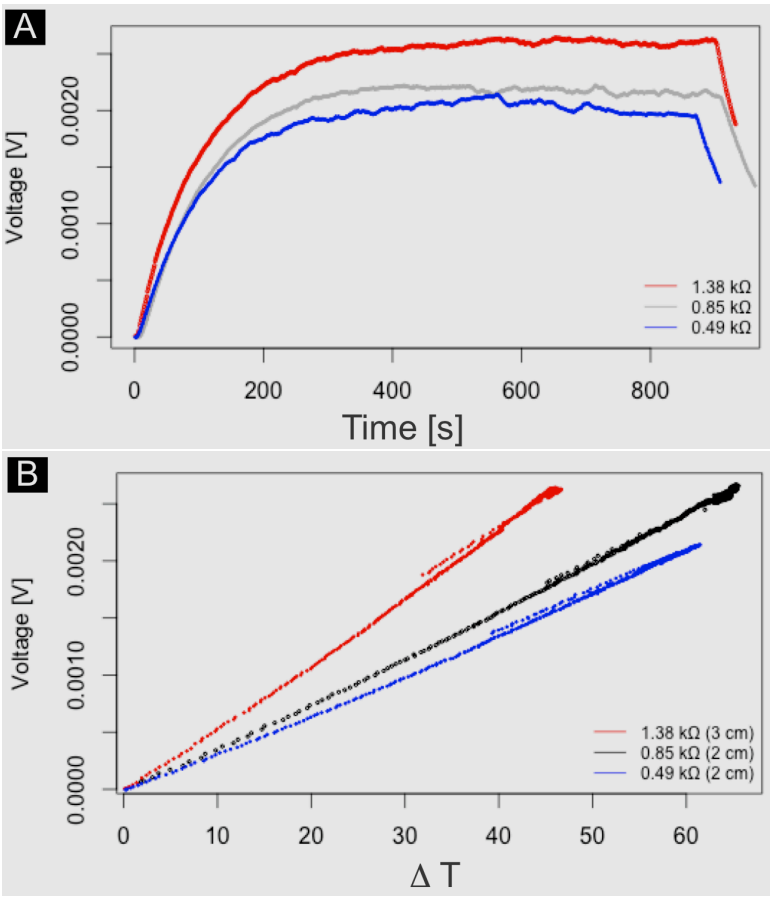

Figure 7.9: A) Voltage delivered by 3 different CNT thermoelectric cells over time. The legend shows the resistivity of the TE cell, the red curve corresponding to a 3 cm long TE cell with 1.38 kΩ resistance, the black curve to a sample 2 cm long and 0.85 kΩ resistance and the blue curve to a 2 cm long TE cell with 0.49 kΩ resistance. B) Voltage produced by the same CNT cells at different temperature gradients.

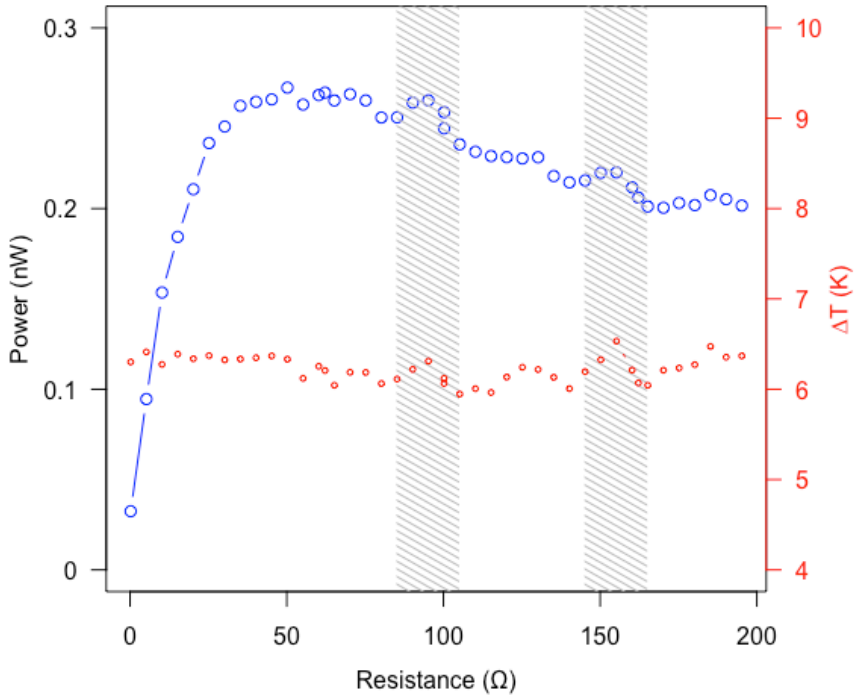

Figure 7.10: Power produced by thermoelectric cells connected to a circuit load. The power reaches a maximum when the resistance load matches the resistance of the TE cell.

ture at the source was sustained during the experimental run and the change in voltage was monitored. It can be observed in Figure 7.9.A that once the sample has achieved the maximum output voltage, it is maintained during the whole experimental run. This is an important result as it means that the device can be used continuously over long periods of time.

In a second experiment, the three samples where exposed to different temperature gradients and the output voltage was recorded. Samples with similar geometries but different resistances were analysed. From the results shown in Figure 7.9.(B) it is apparent that samples with higher resistances produce a higher output voltage. It is important to note that this measurements were performed in an open-circuit configuration. This means that there is no electrical load connected to the device.

The performance of a thermoelectric device can be evaluated by measuring the output power that it delivers when it is connected to a circuit load. This configuration would represent the working conditions of a TE device in real world applications. To simulate this conditions, one thermoelectric cell made of a CNT

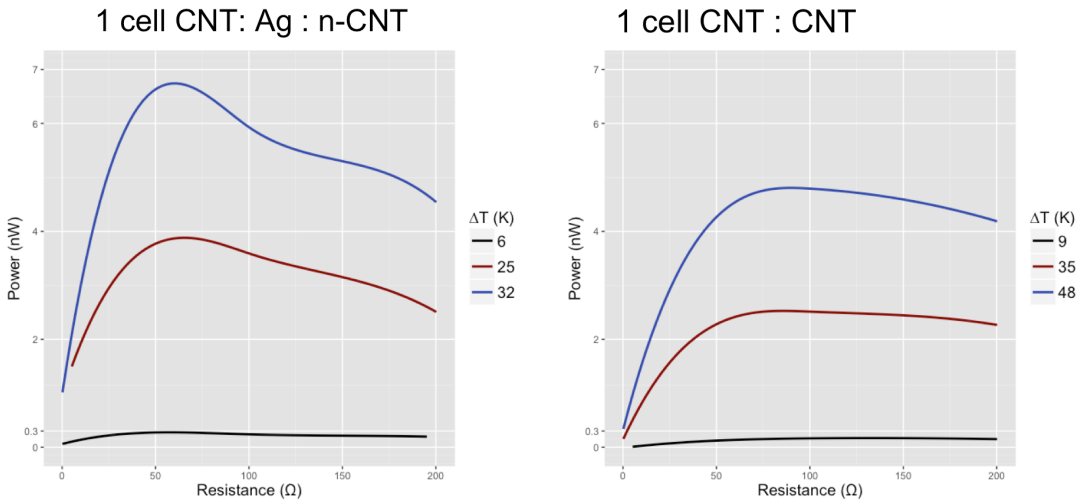

Figure 7.11: Power produced by thermoelectric cells in a closed-circuit configuration. The first plot corresponds to a cell made with CNT legs joined by a layer of silver paint at the junction. The second plot shows the voltage of a CNT TE made solely of carbon nanotubes.

p-type leg and one CNT n-type leg was printed and connected to a series of potentiometers. A temperature gradient was applied to the TE cell and the value of the resistance connected was increased in small steps.

Figure 7.10 shows the results of the measurement. As the value of the resistance increases, the power output measured in nano watts nW also increases until it reaches a maximum value. This maximum matches the values of the internal resistance of the thermoelectric cell. The plot also shows that a small change in the applied temperature gradient has an immediate effect on the power output, as it can be seen in the grey-shaded areas. The results of this experiment are important as they show that the optimum working conditions of any thermoelectric cell are those where the value of the circuit load matches the internal resistance of the cell. A similar result has been used by some groups to develop devices that maximise the power output of thermoelectric devices under changing working conditions.

To evaluate the effect of interface at the junction of the thermoelectric legs, two thermoelectric cells were fabricated. The first one was created by joining two ends of the carbon nanotube legs (p-type and n-type) with a silver interface between them. The CNT legs were printed from CNT dispersions. The second cell was also made by printing an n-type leg and joining one of its ends to the p-type leg, this time putting them into direct contact, without using the silver paint as interface.

Both TE cells were subjected to similar temperature gradients to evaluate the

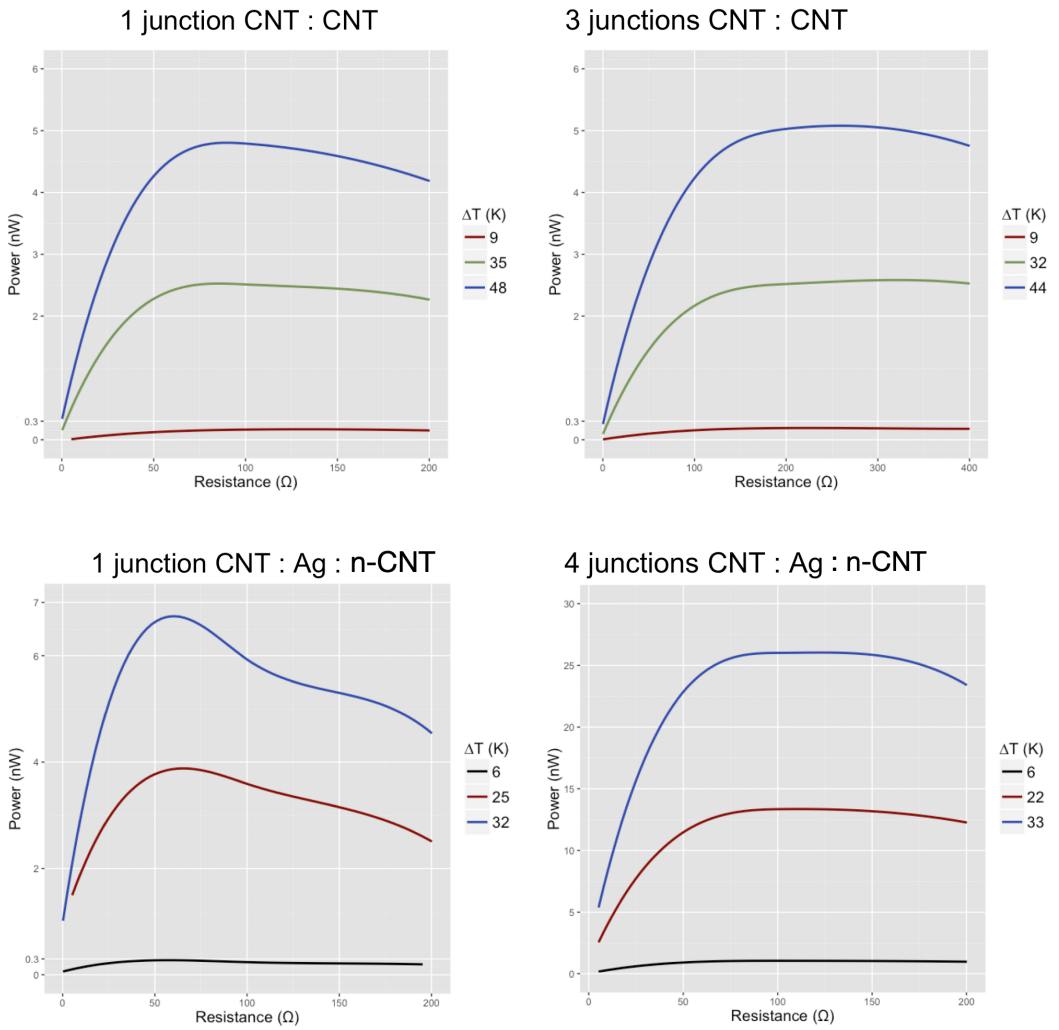

Figure 7.12: Comparison of the power produced by two thermoelectric devices. The image shows the comparison between the power produced by one TE cell and the one produced by a device comprised of 4 TE junctions. The first row correspond to devices made without the silver at the interface and the second row of device made with the silver paint.

performance of both cells. The results presented in Figure 7.11 show that the TE cell with the silver paint at the interface performs better than the pure CNT TE device. To further investigate this, two thermoelectric devices formed by three junctions were printed. The first device comprised junctions with silver paint at the interface. The second device was formed by pure n-type and p-type junctions.

The comparison of the performance of both type of devices is shown in Figure 7.12. The results in the first row correspond to the TE device made purely with CNT dispersions. The second row presents the result of the device where the silver paint was added to the junction.

When there is no silver paint at the junction, adding TE cells to the device

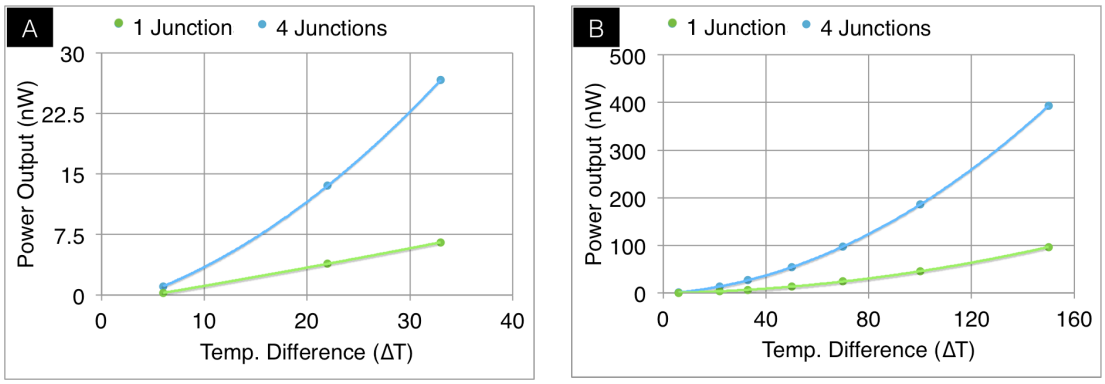

Figure 7.13: Measurement of the power produced by two thermoelectric devices subjected to different temperature gradients. The green curve represents the power output of a TE device made by one junction and the blue curve the power output of a 4 junctions TE device. A) Evaluated using temperature gradients ΔT between 0 K and 40 K. B) Evaluated using temperature gradients ΔT between 0 K and 150 K.

has no effect on the power output. The overall resistance of the printed thermoelectric increases linearly with the number of cells, but the power output remains constant. This means that the cells are acting as a bank of resistance and not as thermoelectric device. This result is confirmed by looking at the plots of the TE device formed with the silver paint shown at the bottom row. When the TE cells are joined together, the power output increases linearly. One TE cell produces 6.5 nW at 32 K of temperature difference and 26 nW at 33 K when 4 junctions are added together.

The power output of two thermoelectric devices produced with the techniques described so far, was evaluated at different temperature gradients. The results are show in Figure 7.13. The performance depends on the physical characteristics of the device, the electrical conductivity of the p-type and n-type legs, their Seebeck coefficient and their thermal conductivity. Regardless of the difference in properties, the power output (P) of a TE device has a quadratic dependence to the temperature difference between the hot and cold end of the device.

$$P \sim \Delta T^2. \tag{7.1}$$

To prove the capabilities of this printing method, a thermoelectric device formed by 9 junctions was printed on a flexible substrate. The device is shown in Figure 7.14. This device shows one of the key advantages of the method developed to produce CNT-based thermoelectric which is the possibility of producing complex patterns that can be used to recover energy from heat source with almost any shape.

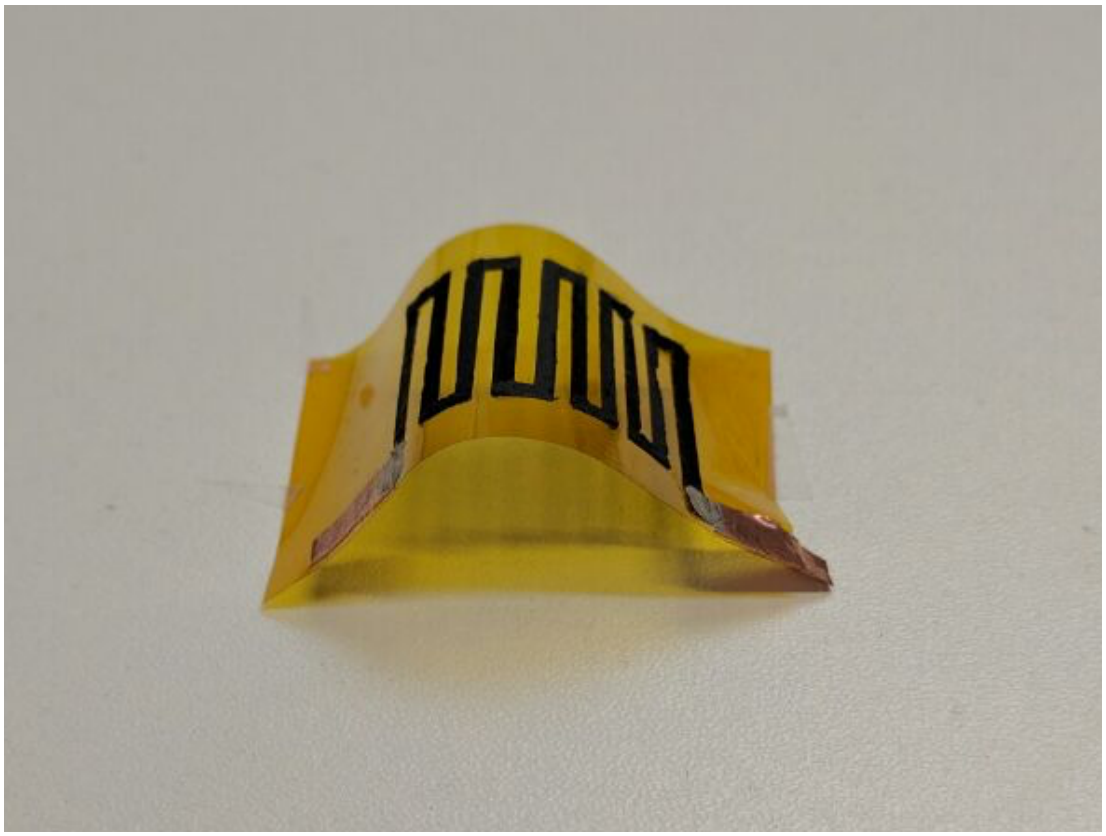

Figure 7.14: 9-junction CNT thermoelectric device printed on Kapton, used to prove the printing of TE devices on flexible substrates.

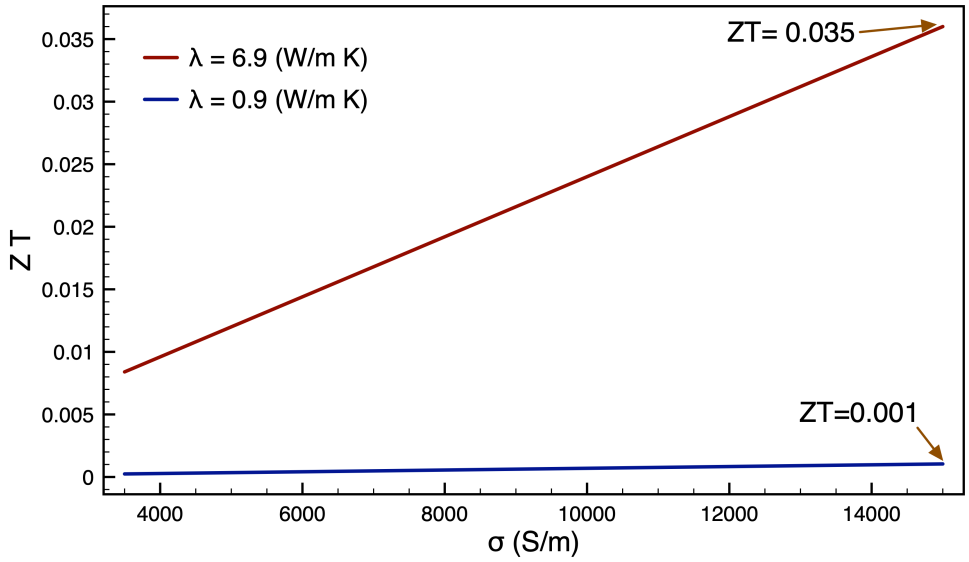

Figure 7.15: Figure of merit of the CNT-based thermoelectric devices evaluated at room temperature as a function of the electrical conductivity.

The characterisation of the CNT thermoelectric devices is completed by calculating their figure of merit. As described before, the figure of merit

$$ZT = \frac{\alpha^2 \sigma}{\lambda} T, \tag{7.2}$$

where α is the Seebeck coefficient, σ the electrical conductivity and λ the thermal conductivity, is a quantity that represents the efficiency of the TE generators. In Figure 7.15, the figure of merit at room temperature is plotted for the CNT TE devices made with p-type and n-type water-based dispersions. The plot shows the value of the figure of merit for different electrical conductivities. The electrical conductivity of the CNT films depends on several factors, type of nanotubes, length, number of walls, diameter; but the values of electrical conductivity measured for this type of films fall within $7800\,\mathrm{S\,m^{-1}}$ to $14\,100\,\mathrm{S\,m^{-1}}$.

The area enclosed between the red and blue line in Figure 7.15 represents all the possible values of the figure of merit for the CNT devices. As the properties of the films change according to the materials used to prepare them and the fabrication parameters, this plot gives an upper and lower limit to the values of the figure of merit. The measured values of the Seebeck coefficient were between $40\,\mu\mathrm{V/K}$ and $80\,\mu\mathrm{V/K}$ and the measured thermal conductivity was between $0.86\,\mathrm{W\,m^{-1}\,K^{-1}}$ and $6.9\,\mathrm{W\,m^{-1}\,K^{-1}}$.

In Figure 7.15, the thermal conductivity defines the limits of the figure of merit. The maximum values (red line) correspond to films with a thermal conductivity of $0.86\,\mathrm{W\,m^{-1}\,K^{-1}}$ and the minimum values (blue line) to thermal conductivities of $6.9\,\mathrm{W\,m^{-1}\,K^{-1}}$. The changes in thermal conductivity are also caused by the fabrication parameter of the films. For example, the sonication time can change the size of the nantoubes; films with smaller nanotubes would have more nanotube junctions which would increase the phonon scattering and decrease the thermal conductivity. The same would happen if the amount of surfactant molecules in the film increases, the thermal conductivity would decrease.

The different fabrication parameters yield values of the figure of merit between 0.001 and 0.035. A deeper study of the fabrication conditions of the CNT films would be required to understand their effect on the Seebeck coefficient, thermal and electrical conductivity. This work focused on the characterisation of the TE devices. The values of the figure of merit obtained can still be optimised and ideally controlled according to the requirements of the different applications.

7.3 Conclusions

In this chapter a method to print the dispersions produced in the previous sections was developed. The system was made by coupling a CNC machine and dispensing valves capable of depositing CNT dispersions with high weight content of nanotubes. The system was used to produce TE devices in which the size and position of the thermoelements were accurately controlled.

Using this system it was possible to print conductive tracks formed by a network of CNTs on different substrates, i.e. glass, flexible polymers and metals. This was achieved by a careful control of the experimental parameters associated to the printing of carbon nanotube dispersions. The system requires the control of the speed deposition and pressure applied to the nozzles according to the type of substrate and viscosity of the nanotube dispersion. Complex patters can be printed with a minimum feature size of 1 mm at speeds of 8 m/min. Although this is not comparable to traditional inkjet printing methods, which can print features of up to 30 µm [212], the capacity of printing solutions with high viscosities means that conductive tracks can be achieved by a single deposition. This is not possible using traditional inkjet technologies which require several depositions to increase the conductivity [213].

The thermoelectric devices were printed using water-based CNT inks. The thermoelements were made from p-type and n-type CNT dispersions. The performance of these devices was evaluated by applying different temperature gradients and recording the power output. The power delivered by the TE device is not the same when it is measured in an open circuit configuration or when an electric load is connect to the TE generator. In an open circuit configuration, the resistance connected to the device is equal to zero and the power output is minimum. When a load is connected, the maximum power output for a specific thermal gradient is obtained when the resistance of the load matches the internal resistance of the device.

This result implies that in real world applications, the efficiency of the thermoelectric device is not only determined by the temperature gradient and the properties of the thermoelements. The power output is also associated to the load connected. This means that the internal resistance of the TE generator, which is given by the number of TE elements, has to be designed for every specific type of application. This is a problem that has been encountered in other types of power generation technologies, like solar cells. Electronic components known as maxi-

mum power point tracking devices (MPPT) are used to continuously monitor the operating conditions that maximise the efficiency of the generators. MPPT can also be used with TE devices and would be a requirement to obtain the highest conversion efficiency of the generators [214, 215].

The effect of the TE junction discussed in Section 3.3 was further explored in this chapter. Printed TE devices with silver paint at the interface between the p-type and n-type thermoelements were fabricated and compared to printed generators without a metallic interface. It was found that when the metallic interface was used, several TE junctions could be connected in series and the power output would increase linearly with the number of junctions. If the metallic interface was removed from the junction, connecting additional junctions in series would not have an effect on the power output of the device. The extra junctions would only increase the resistance of the TE generator.

These effect can be explained in terms of the type of junction formed. When there is a metallic layer between the two semiconductors, an ohmic contact or a Schottky barrier is formed, then the carrier concentration is increased in the hot side and the current flows through the device. When there in no metallic layer, the p-type and n-type semiconductor are in direct contact, this forms a p-n junction that generates a localised depletion zone at the junction. When the negative charges diffuse into the p-side, they recombine with holes near the junction creating a negatively charged area. The opposite effect occurs with the holes from the p-type semiconductor migrating into the n-side of the junction. The charged regions near the junction create an electric field that opposes the movement of carriers limiting the power output of the device. This highlights the importance of the metallic interface at the junction.

The final characterisation of the CNT thermoelectric devices was made by calculating the figure of merit at room temperature. The value of the figure of merit is highly dependant on the thermal and electrical conductivities of the samples. The values of the figure of merit were found to be in a region between 0.001 and 0.035. This places the efficiency of the CNT devices at least one order of magnitude below that of the highest figures of merit recorded in the best thermoelectric materials ($ZT \approx 0.8$), but comparable to thermoelectric devices made with organic materials and doped polymers [97].

Comparing the devices made with this printing method to the hand-made devices presented in the first part of this work. Several advantages can be pointed out. The controlled deposition allows for the creation of complex patterns, the

ease of using an automated method improves the amount of time spent in the fabrication of the devices. Flexible devices is another advantage that this method provides, the hand-made devices had to be rigid to maintain the integrity of the junction. A critical improvement achieved with this method is the quality of the junctions. As the materials dry on top of each other when they are deposited, the peeling process that ruined the junctions in the first prototypes does not occur. This also improves the contact resistance at the junction, which was described as a key parameter in the fabrication of thermoelectric generators.

These results were obtained from a first approach using this specific printing method. There is still plenty of room for improvement, which requires more experimentation with materials to improve the thermoelements, junctions and fabrication parameters.

8

Conclusions and future work

The aim of this work was to develop a methodology for the fabrication and characterisation of thermoelectric devices made with carbon nanotubes films. It was decided that the work would focus on the development of power generators. For this reason an important requirement of this work was the development of prototypes that demonstrated the feasibility of transforming temperature differences into power using carbon nanotubes.

Careful evaluation of the theoretical background and literature available regarding the thermoelectric phenomena in different materials, indicated that it is necessary to evaluate three material properties associated to the thermoelectric characteristics of the CNTs. The electrical conductivity, Seebeck coefficient and Thermal conductivity. From these properties, electrical conductivity measurements could be carried out using the ready available 4-probe method technique. But the characterisation of the Seebeck coefficient and the thermal conductivity required the development of specialised equipment.

Carbon nanotube films can be produced from CNT carpets using different methods, all of them require the processing of the nanotubes into a liquid solution which is later deposited and dried to form the CNT film. Another available method to produce films is the directly spinning of the CNT film from the hot zone of a CVD reactor. Due to the fact that this technique is a one-step processing

method, it was decided to use this material in the first stage of this work.

This first part involved the characterisation of the Seebeck coefficient of the material. The different techniques available for the measurement of this property were analysed. Considering the geometry of the material, a film of a few microns of thickness, the equipment required and the accuracy of the methods; it was decided to fabricate a 2-probe set-up to measure the Seebeck coefficient which would use a quasi-steady technique in which the sample is subjected to different temperature gradients and the voltage generated is recorded.

The fabrication of the set-up was discussed and the experimental parameters for a reliable measurement were defined. The set-up was evaluated using constant films, a material which is commonly used as reference in this type of measurements. The results of the measurements of the Seebeck coefficient of constantan ($-40\,\mu V\,K^{-1}$) were in agreement with the values reported in literature[75, 77]. The Seebeck coefficient measurement on the CVD produced CNT films resulted in positive values between $40\,\mu V\,K^{-1}$ and $80\,\mu V\,K^{-1}$. In literature it is reported that the CNTs have an intrinsic positive Seebeck coefficient value that has been associated to oxygen doping [186]. This was confirmed by the results of the measurements in this work.

The carbon nanotubes in these type of films are oriented parallel to the longitudinal axis of the film, which is defined by the direction in which it was spun. Measurements of electrical conductivity have reported difference according to the direction in which the measurement is made [216]. In the case of the Seebeck coefficient, the alignment of the tubes had little effect on the value measured along the main direction of orientation of the nanotubes or measured perpendicularly. The reported values are very similar in both directions.

The magnitude of the Seebeck coefficient measured in carbon nanotube films is not as high as standard thermoelectric materials, like bismuth telluride ($\approx 150\,\mu V\,K$) [87] or lead telluride ($\approx 200\,\mu V\,K$) [90]. But it places this material close to any other organic thermoelectric, which can be used in applications where flexible and light weight materials are required.

One of the main advantages of the set-up developed to measure the Seebeck coefficient that it is not restricted to a specific material, it can be used different types of films as it was demonstrated. It also allows for films with different geometries. The limitations of this set-up are that measurements can only be performed in a very small temperature range, from room temperature to $\approx 400\,K$ and currently can only be done in air.

Future work would include improvements to this set-up to allow the characterisation of the Seebeck coefficient of films in a much broader temperature range. This could be achieve by introducing additional heaters to the chamber not in contact with the sample and designing a new holder which can be placed in a cryostat. Regarding the measurements performed in the CNT films, the evaluation of the Seebeck coefficient in vacuum or other atmospheres would also complete the characterisation of this property. Measurements on films produced with carbon precursors other than toluene should be performed to correlate the Seebeck coefficient to the parameters of the CVD process.

After the evaluation of the Seebeck coefficient of constantan and the CVD CNT films, the first thermoelectric prototypes were fabricated. A TE device requires the creation of a junction between a p-type conductor and an n-type conductor. As the main types of carriers in constantan are electrons, it is an n-type conductor. In the case of the the CNT films, the positive Seebeck coefficient indicates that the main type of carriers are holes, which makes it a p-type semiconductor. Taking this into account and the similar magnitude of the Seebeck coefficient of both materials, these films were selected to form a TE device.

The method used for the manufacture of the TE generator involved several steps, from laser cutting the films to specific dimensions to the manual creation of the metallic junction at the interface of the p-type and n-type legs. This process was slow and prone to errors, as it was shown when the junctions in the first prototype failed due to an increase in the contact resistance at the junction. This first prototype produced 1.9 V when subjected to a temperature gradient of 220 K. A second device where the manufacture process was improved and the dimensions of the devices decreased, resulted in a TE generator that produced 2.4 V under the same temperature gradient.

These devices proved that it was possible to generate power using the CNT films, but they also showed that the manufacture process could be greatly improved. The key results obtained were related to the scalability of the TE generator and the quality of the junctions. When the device dimensions where optimised and the number of TE junctions increased, the voltage produced by the device increased proportionally. It was also shown that the resistance at the junction plays an important part on the overall conversion efficiency of the TE generator. When the resistance of the contact between the thermoelements increases, it leads to heat loses and diminished flow of carriers at the junction, which directly affects the efficiency of the device.

These results motivated the search for a new manufacture method in which the dimensions of the thermoelements could be controlled and the quality of their junction improved. Printing technologies are good alternative for the controlled deposition of the CNTs, but they required the nanotubes to be dispersed into a printable solution.

An analysis of the theoretical background of nanotube dispersions resulted in the decision of dispersing the nanotubes in water using sodium dodecylbenzemne (SDBS) as the dispersing agent. This dispersing methodology was a good compromise between a method that avoided toxic elements and the lowest damage possible to the structure of the nanotubes. As carbon nanotubes are hydrophobic, the use of a surfactant was necessary to disperse them in water. To introduce the surfactant molecules between the nanotubes, energy has to be applied to the nanotube bundles to separate the tubes. This energy was supplied through sonication with an ultra sonication horn.

Both processes, addition of surfactant and sonication, have an effect on the CNT network. The surfactant molecules create barriers for the free movement of carriers through the nanotube network. The sonication damages the nanotube walls and shortens the tubes which also affects the path of the carriers by creating more nanotube junctions. Because of these two effects, the experimental parameters to find the minimum amount of SDBS required to disperse the tubes were explored. This resulted in a minimum 0.25 wt% of surfactant per 1 wt% of CNTs.

The effect of the sonication was explored by comparing the size of the nanotubes after different sonication times. The technique presented involved the analysis of SEM images of nanotubes sonicated for two and three hours. This analysis resulted in curves that described the nanotube size distribution in the samples. After two hours of sonication the majority of nanotubes were about 4 µm long. One extra hour of sonication shortened the tubes by 20 %.

The measurement of the length of the nanotubes in films is a hard problem to attack. As produced, the nanotubes in the films are interlaced between themselves, this makes it difficult to measurement the length of the nanotubes using any imaging analysis as it is not possible to see where the nanotube starts or where it ends. Using the technique presented here, the initial nanotube size could be extrapolated from the measurement of the nanotube size after different sonication times. The drawback from this technique is the amount of time that the analysis of the SEM images requires. But this could be done using special

software for image analysis.

To fabricate a fully printed TE device from CNT water-based dispersions, it was necessary to produce an n-type nanotube dispersion. To modify the intrinsic p-type characteristics of the nanotubes it is necessary to dope them with an electron donor. In this work, the doping was made through substitutional nitrogen. This type of doping was chosen because it is stable in air. CNTs were synthesised using CVD and pyrazine and benzylamine as nitrogen precursors. The doped nanotubes were dispersed in water and the doping was evaluated through Raman spectroscopy and measurements of the Seebeck coefficient. These measurements resulted in values between $-36\,\mu V\,K^{-1}$ and $-46\,\mu V\,K^{-1}$ which confirmed the n-type semiconducting nature of the doped samples.

Thermal conductivity measurements were carried out to conclude the characterisation of the CNT films. A parallel thermal conductance method was used to measure the conductance of the sample and correlate it to its thermal conductivity. This steady-sate method was chosen because it requires almost no sample preparation and it allows the easy measurement of conductance in several sample morphologies like fibres or films. A set-up was built to perform this measurements. The manufacture of the set-up and the experimental parameters were presented. The system was calibrated by measuring the thermal conductivity of copper films. The obtained value was $403\,W\,m^{-1}\,K^{-1}$ which is almost the same as the nominal value of $401\,W\,m^{-1}\,K^{-1}$.

The thermal conductivity of different CNT films was evaluated. The lowest thermal conductivity was found to be $0.86\,W\,m^{-1}\,K^{-1}$ and it was measured in the nitrogen doped films made from the CNT water dispersions. The highest value was $123\,W\,m^{-1}\,K^{-1}$ for the CVD CNT films measured along the main direction of the nanotubes alignment.

As discussed before, the dispersing process creates disruptions in the nanotube network. These disruptions act as barriers for the movement of carriers and are also phonon scattering points. Since the conduction of heat in the material is done by a combination of carrier and phonon movement, the CNT films made from water dispersions are expected to have lower thermal conductivities than the films synthesised directly from the CVD method. This is consistent with the measured values of thermal conductivity. In the case of the doped samples, it was shown using Raman analysis that there is a higher amount of defects present in the nanotube lattice. This defects are introduced by the substitutional nitrogen atoms. This is the reason why the lowest thermal conductivity was found in the

N-doped films.

The method presented to measure the thermal conductivity relies heavily on a good determination of the dimensions of the sample. In the case of solid materials, like the copper films, this does not represent a problem. The method assumes that the cross-sectional area of the sample is constant. This is not true for the CNT films, which have empty spaces between nanotubes. Further studies have to be made to calculate an scaling factor that consider this type of morphology. If a smaller cross-sectional area is considered for the CNT films, the magnitude of the thermal conductivity will also decrease.

In the final section of this dissertation, thermoelectric devices made from dispersions of CNTs were fabricated. In order to deposit the dispersions in a controlled manner, a system to print the CNT solutions was built. This system is capable of printing CNT dispersions with a high content of CNTs, which is necessary to have conductive tracks.

Dispersions of p-type and n-type nanotubes where printed on Kapton to form the legs of thermoelectric devices made from several TE junctions in series. The evaluation of the power output of these devices revealed important parameters that control the efficiency of the Te generators. It was found that the maximum power output of the devices was achieved when an electrical load matching the internal resistance of the generator was connected to the device. The lowest power output was seen when the measurement was made on a device with no electrical load. This result showed that not only the thermoelectric properties of the thermoelements control the efficiency of a thermoelectric generator, but also the type of application in which the device is used.

Printing thermoelectric devices with no metallic interface at the junction between the thermoelements showed the importance of the interface. When the metal was present Schottky barriers were formed between the metal and the semiconductor. These type of junction promoted the movement of carriers and therefore the power generation. When the metal was removed from the interface, a pure p-n junction was formed with strong localised energy fields that reduced the movement of carriers and decreased the efficiency of the device.

In this work, silver paint was used as a metallic interface, but as it was discussed, other types of metals could be used to improve even further the junction between the thermoelements. In fact, the enhancement of the flow of carriers at the junction can be done if more than one metal is used at the same time in the metallic interface. A metal that matches the p-type and creates a low Schottky

barrier at the p-side and a different metal that creates an ohmic contact at the n-type interface.

When the printed TE devices were made, the CNT dispersions were deposited with the printer, but the silver paint was added manually. Further improvements to the printing equipment should allow the deposition of different materials at the same time. The additional equipment would have to include printer heads capable of depositing metals.

The evaluation of the figure of merit of the CNT thermoelectric devices yielded a maximum figure of merit at room temperature of $ZT = 0.035$. This value is at least 20 times smaller than established thermoelectric materials ($ZT > 0.8$), but it has the advantage of being a non optimised value. Further research can be done to improve this figure of merit. Different solvents can be explored, other types doping which could improve the electrical conductivity or the Seebeck coefficient. The CNT dispersions could also be prepared using pre-selected nanotubes, for example, dispersions of only single walled nanotubes. Films containing a higher amount of metallic nanotubes can also be explored. Combinations of conductive polymers and nanotubes could be used instead of surfactants to improve the electrical conductivity of the dispersions.

The field of organic thermoelectrics is still being developed and there are many routes that can be explored to improve the efficiencies and manufacturing processes of TE generators. This work showed one of these possible routes of improvement, starting from a device made from the combination of organic and metal thermoelements to the development of a printing technology that can be used to manufacture flexible organic thermoelectrics.

Bibliography

[1] R.H. Baughman, A. A. Zakhidov, and de Heer W. A. Carbon nanotubes – the route toward applications. *Science*, 297:787–792, 2002.

[2] Thomas Johann Seebeck. Magnetic polarization of metals and minerals. *Abhandlungen der Deutschen Akademie der Wissenschaften zu Berlin*, 265:1822–1823, 1822.

[3] Thomas Johann Seebeck. *Magnetische polarisation der metalle und erze durch temperatur-differenz*. W. Engelmann, 1895.

[4] J. C. Peltier. Nouvelles experiences sur la caloricite des courans electrique. *Ann. chim*, 56:371, 1834.

[5] Daniel D. Pollock. *Thermocouples: Theory and Properties*. CRC Press, 1991.

[6] ASTM Committee E20 on Temperature Measurement. *Manual on the Use of Thermocouples in Temperature Measurement*. ASTM manual series MNL 12-4TH. ASTM, fourth edition, 1993.

[7] William Thomson. On a mechanical theory of thermoelectric currents. *Proceedings of the Royal Society of Edinburgh*, 91:1851, 1851.

[8] Daniel D. Pollock. *Physical Properties of Materials for Engineers*. CRC Press, 1993.

[9] Lord Rayleigh. Xliii. on the thermodynamic efficiency of the thermopile. *Philosophical Magazine Series 5*, 20(125):361–363, 1885.

[10] E. Altenkirch. Über den nutzeffekt der thermosäule. *Physikalische Zeitschrift*, 10:560, 1909.

[11] E. Altenkirch. Elektrothermische kälteerzeugung und reversible elektrische heizung. *Physikalische Zeitschrift*, 12:920–924, 1911.

[12] David M. Rowe, editor. *CRC Handbook of Thermoelectrics*. CRC Press, Boca Raton, Fla. ; London, 1995.

[13] M. S. Dresselhaus, G. Chen, M. Y. Tang, R. G. Yang, H. Lee, D. Z. Wang, Z. F. Ren, J.-P. Fleurial, and P. Gogna. New directions for low-dimensional thermoelectric materials. *Advanced Materials*, 19(8):1043–1053, 2007.

[14] Arun Majumdar. Thermoelectricity in semiconductor nanostructures. *Science*, 303(5659):777–778, 2004.

[15] Maria Telkes. The efficiency of thermoelectric generators. I. *Journal of Applied Physics*, 18(12):1116 –1127, 1947.

[16] Abram Federovich Ioffe. *Semiconductor Thermoelements and Thermoelectric Cooling. [Based on Poluprovodnikovye Termoelementy by A.F. Ioffe and Termoelektricheskoe Okhlazhdenie by A.F. Ioffe and others]*. Infosearch Limited, London, [1957], 1957.

[17] Daniel D. Pollock. *Thermoelectricity: theory, thermometry, tool*. ASTM special technical publication ; 852. ASTM, Philadelphia, PA, 1985.

[18] A. W. Fenton. How do thermocouples work? *Nuclear Energy*, 19(1):61–63, 1980.

[19] Charles Kittel. *Introduction to solid state physics*. Wiley, Hoboken, N.J, 8th ed., wiley international ed edition, 2005.

[20] I. B. Cadoff and E. Miller. *Thermoelectric materials and devices*. Materials technology series. Reinhold Publishing Corporation, 1960.

[21] David M. Rowe. Recent advances in silicon-germanium alloy technology and an assessment of the problems of building the modules for a radioisotope thermo-electric generator. *Journal of Power Sources*, 19(4):247 – 259, 1987.

[22] Glen A. Slack and Moayyed A. Hussain. The maximum possible conversion efficiency of silicon-germanium thermoelectric generators. *Journal of applied physics*, 70(5):2694–2718, 1991.

[23] R. A. Hutner, E. S. Rittner, and F. K. DuPre. Fermi levels in semiconductors. *Philips Res. Rep*, 5:188, 1950.

[24] Victor Fistul. *Heavily doped semiconductors*. Plenum Press, New York, Plenum Press, 1969, 1969. Translated from Russian by Albin Tybulewicz.

[25] David M. Rowe and C. M. Bhandari. *Modern Thermoelectrics*. Reston Publishing Company, 1983.

[26] H. J. Goldsmid. *Electronic refrigeration*. Pion, 1986.

[27] F. DuPre Rosi. Thermoelectricity and thermoelectric power generation. *Solid-State Electronics*, 11(9):833 – 868, 1968.

[28] John Edwin Parrott and Audrey D. Stuckes. *Thermal conductivity of solids*, volume 8. Pion London, 1975.

[29] G. Chen, M. S. Dresselhaus, G. Dresselhaus, J-P Fleurial, and T. Caillat. Recent developments in thermoelectric materials. *International Materials Reviews*, 48(1):45–66, 2003.

[30] H. J. Goldsmid and A.W. Penn. Boundary scattering of phonons in solid solutions. *Physics Letters A*, 27(8):523 – 524, 1968.

[31] Dong-Hwan Kim and Tadaoki Mitani. Thermoelectric properties of fine-grained Bi_2Te_3 alloys. *Journal of Alloys and Compounds*, 399(1-2):14 – 19, 2005.

[32] H. R. Meddins and J. E. Parrott. The thermal and thermoelectric properties of sintered germanium-silicon alloys. *Journal of Physics C: Solid State Physics*, 9(7):1263, 1976.

[33] David M. Rowe and C. M. Bhandari. Effect of grain size on the thermoelectric conversion efficiency of semiconductor alloys at high temperature. *Applied Energy*, 6(5):347 – 351, 1980.

[34] P. G. Klemens. The scattering of low-frequency lattice waves by static imperfections. *Proceedings of the Physical Society. Section A*, 68(12):1113, 1955.

[35] C. T. Walker and R. O. Pohl. Phonon scattering by point defects. *Physical Review*, 131(4):1433, 1963.

[36] Gerald Mahan, Brian Sales, and Jeff Sharp. Thermoelectric materials: New approaches to an old problem. *Physics Today*, 50:42, 1997.

[37] G. Mahan. Figure of merit for thermoelectrics. *Journal of Applied Physics*, 65(4):1578–1583, 1989.

[38] David M. Rowe. Thermoelectric waste heat recovery as a renewable energy source. *International Journal of Innovations in Energy Systems and Power*, 1(1):13–23, 2006.

[39] H. J. Goldsmid, A. R. Sheard, and D. A. Wright. The performance of bismuth telluride thermojunctions. *British Journal of Applied Physics*, 9(9):365, 1958.

[40] Hiroshi Julian Goldsmid. *Thermoelectric refrigeration*, volume 1. Plenum Press New York, 1964.

[41] W. M. Yim and F. DuPre Rosi. Compound tellurides and their alloys for peltier cooling—a review. *Solid-state electronics*, 15(10):1121–1140, 1972.

[42] B. Abeles and R. W. Cohen. Ge-si thermoelectric power generator. *Journal of Applied Physics*, 35(1):247–248, 1964.

[43] Hiroshi Julian Goldsmid and Bernard Lister Worsnop. *Applications of thermoelectricity*, volume 960. Methuen London, 1960.

[44] Wonjoon Choi, Joel T. Abrahamson, Jennifer M. Strano, and Michael S. Strano. Carbon nanotube-guided thermopower waves. *Materials Today*, 13(10):22 – 33, 2010.

[45] Amy M. Marconnet, Matthew A. Panzer, and Kenneth E. Goodson. Thermal conduction phenomena in carbon nanotubes and related nanostructured materials. *Rev. Mod. Phys.*, 85:1295–1326, Aug 2013.

[46] C. Yu, L. Shi, Z. Yao, D. Li, and A. Majumdar. Thermal conductance and thermopower of an individual single-wall carbon nanotube. *Nano Letters*, 5(9):1842–1846, 2005.

[47] P. Kim, L. Shi, A. Majumdar, and P. L. McEuen. Thermal transport measurements of individual multiwalled nanotubes. *Phys. Rev. Lett.*, 87:215502, Oct 2001.

[48] Y.-M. Choi, D.-S. Lee, R. Czerw, P.-W. Chiu, N. Grobert, M. Terrones, M. Reyes-Reyes, H. Terrones, J.-C. Charlier, P. M. Ajayan, S. Roth, D. L. Carroll, and Y.-W. Park. Nonlinear behavior in the thermopower of doped

carbon nanotubes due to strong, localized states. *Nano Letters*, 3(6):839–842, 2003.

[49] H. E. Romero, G. U. Sumanasekera, G. D. Mahan, and P. C. Eklund. Thermoelectric power of single-walled carbon nanotube films. *Physical Review B*, 65(20), may 2002.

[50] Chuizhou Meng, Changhong Liu, and Shoushan Fan. A promising approach to enhanced thermoelectric properties using carbon nanotube networks. *Advanced Materials*, 22(4):535–539, 2010.

[51] Tingting Miao, Weigang Ma, Xing Zhang, Jinquan Wei, and Jialin Sun. Significantly enhanced thermoelectric properties of ultralong double-walled carbon nanotube bundle. *Applied Physics Letters*, 102(5):053105, feb 2013.

[52] J. Hone, I. Ellwood, M. Muno, Ari Mizel, Marvin L. Cohen, A. Zettl, Andrew G. Rinzler, and R. E. Smalley. Thermoelectric power of single-walled carbon nanotubes. *Physical review letters*, 80(5):1042, 1998.

[53] Hai-Long Zhang, Jing-Feng Li, Bo-Ping Zhang, Ke-Fu Yao, Wei-Shu Liu, and Heng Wang. Electrical and thermal properties of carbon nanotube bulk materials: Experimental studies for the 328–958 K temperature range. *Physical Review B*, 75:205407, May 2007.

[54] Choongho Yu, Yeon Seok Kim, Dasaroyong Kim, and Jaime C Grunlan. Thermoelectric behavior of segregated-network polymer nanocomposites. *Nano letters*, 8(12):4428–4432, 2008.

[55] Joshua Martin, T. Tritt, and C. Uher. High temperature Seebeck coefficient metrology. *Journal of Applied Physics*, 108(12):121101, dec 2010.

[56] Joshua Martin. Protocols for the high temperature measurement of the Seebeck coefficient in thermoelectric materials. *Measurement Science and Technology*, 24(8):085601, jul 2013.

[57] Kasper A. Borup, Johannes de Boor, Heng Wang, Fivos Drymiotis, Franck Gascoin, Xun Shi, Lidong Chen, Mikhail I. Fedorov, Eckhard Müller, Bo B. Iversen, and G. Jeffrey Snyder. Measuring thermoelectric transport properties of materials. *Energy & Environmental Science*, 8(2):423–435, 2015.

[58] C. Wood, A. Chmielewski, and D. Zoltan. Measurement of Seebeck coefficient using a large thermal gradient. *Review of Scientific Instruments*, 59(6):951–954, jun 1988.

[59] Pankaj K. Rawat and Biplab Paul. Simple design for seebeck measurement of bulk sample by 2-probe method concurrently with electrical resistivity by 4-probe method in the temperature range 300–1000 K. *Measurement*, 91:613–619, sep 2016.

[60] Ashutosh Patel and Sudhir K. Pandey. Automated instrumentation for high-temperature Seebeck coefficient measurements. *Instrumentation Science & Technology*, 45(4):366–381, nov 2016.

[61] A. Narjis, M. Elyaagoubi, A. Outzourhit, and L. Nkhaili. Design of a simple apparatus for the measurement of the Seebeck coefficient. *Measurement*, 133:433–438, feb 2019.

[62] Avinna Mishra, Sarama Bhattacharjee, and Shahid Anwar. Simple apparatus to measure Seebeck coefficient up to 900 K. *Measurement*, 68:295–301, may 2015.

[63] Joshua Martin. Apparatus for the high temperature measurement of the Seebeck coefficient in thermoelectric materials. *Review of Scientific Instruments*, 83(6):065101, jun 2012.

[64] Shiho Iwanaga, Eric S. Toberer, Aaron LaLonde, and G. Jeffrey Snyder. A high temperature apparatus for measurement of the Seebeck coefficient. *Review of Scientific Instruments*, 82(6):063905, jun 2011.

[65] Qiang Fu, Yucheng Xiong, Wenhua Zhang, and Dongyan Xu. A setup for measuring the seebeck coefficient and the electrical resistivity of bulk thermoelectric materials. *Review of Scientific Instruments*, 88(9):095111, sep 2017.

[66] Aiqiang Guan, Hanfu Wang, Hao Jin, Weiguo Chu, Yanjun Guo, and Guiwu Lu. An experimental apparatus for simultaneously measuring Seebeck coefficient and electrical resistivity from 100 K to 600 K. *Review of Scientific Instruments*, 84(4):043903, apr 2013.

[67] Hanfu Wang, Fanglong Yang, Yanjun Guo, Kaiwu Peng, Dongwei Wang, Weiguo Chu, and Shuqi Zheng. Determination of the thermopower of microscale samples with an AC method. *Measurement*, 131:204–210, jan 2019.

[68] Sanjay Kumar Kedia, Anil Singh, and Sujeet Chaudhary. Design, development, and testing of a thermopower measurement system by studying the electron transport properties on indium and nitrogen co-doped sputtered ZnO films. *Measurement*, 117:49–56, mar 2018.

[69] Mohammad Abir Hossain, Seyedhamidreza Alaie, and Mehran Tehrani. Measurement of the thermoelectric power factor of films over the 10–400 K range. *Review of Scientific Instruments*, 87(4):045111, apr 2016.

[70] A. T. Burkov, A. Heinrich, P. P. Konstantinov, T. Nakama, and K. Yagasaki. Experimental set-up for thermopower and resistivity measurements at 100–1300 K. *Measurement Science and Technology*, 12(3):264, 2001.

[71] R. H. Kropschot and F. J. Blatt. Thermoelectric power of cold-rolled pure copper. *Phys. Rev.*, 116:617–620, Nov 1959.

[72] Andrew I. Dahl W. F. Roeser. Reference tables for iron constantan and copper constantan thermocouples. *Journal of Research of the National Bureau of Standards*, 20:337–356, March 1938.

[73] J. R. Davis, editor. *ASM Speciality Handbook Copper and Copper Alloys*. ASM International, 2001.

[74] Samuel J. Rosenberg. Nickel and its alloys. Technical report, DTIC Document, 1968.

[75] H. M Ahmad and D. Greig. The electrical resistivity and thermopower of nickel-copper alloys. *Le Journal de Physique Colloques*, 35(C4):C4–223, 1974.

[76] Eundeok Mun, Sergey L Bud'ko, Milton S Torikachvili, and Paul C Canfield. Experimental setup for the measurement of the thermoelectric power in zero and applied magnetic field. *Measurement Science and Technology*, 21(5):055104, 2010.

[77] N. D. Lowhorn, W. Wong-Ng, W. Zhang, Z. Q. Lu, M. Otani, E. Thomas, M. Green, T. N. Tran, N. Dilley, S. Ghamaty, N. Elsner, T. Hogan, A. D.

Downey, Q. Jie, Q. Li, H. Obara, J. Sharp, C. Caylor, R. Venkatasubramanian, R. Willigan, J. Yang, J. Martin, G. Nolas, B. Edwards, and T. Tritt. Round-robin measurements of two candidate materials for a Seebeck coefficient standard reference material™. *Applied Physics A*, 94(2):231–234, sep 2008.

[78] K. L. Chopra, S. K. Bahl, and M. R. Randlett. Thermopower in thin-film copper—constantan couples. *Journal of Applied Physics*, 39(3):1525–1528, 1968.

[79] T. S. Gspann, F. R. Smail, and A. H. Windle. Spinning of carbon nanotube fibres using the floating catalyst high temperature route: purity issues and the critical role of sulphur. *Faraday Discuss.*, 173:47–65, 2014.

[80] Ya-Li Li, Ian A. Kinloch, and Alan H. Windle. Direct spinning of carbon nanotube fibers from chemical vapor deposition synthesis. *Science*, 304(5668):276–278, 2004.

[81] Krzysztof Koziol, Juan Vilatela, Anna Moisala, Marcelo Motta, Philip Cunniff, Michael Sennett, and Alan Windle. High-performance carbon nanotube fiber. *Science*, 318(5858):1892–1895, 2007.

[82] Kelly Stano L., Krzysztof Koziol, Martin Pick, Marcelo S. Motta, Anna Moisala, Juan J. Vilatela, Stuart Frasier, and Alan H. Windle. Direct spinning of carbon nanotube fibres from liquid feedstock. *International Journal of Material Forming*, 1(2):59–62, 2008.

[83] Juan José Vilatela García. *Structure, Properties and Treatments of Carbon Nanotube Fibres*. PhD thesis, University of Cambridge, 2009.

[84] M. Motta, A. Moisala, I. A. Kinloch, and Alan H. Windle. High performance fibres from , dog bone, carbon nanotubes. *Advanced Materials*, 19(21):3721–3726, 2007.

[85] Lei Ding, Alexander Tselev, Jinyong Wang, Dongning Yuan, Haibin Chu, Thomas P McNicholas, Yan Li, and Jie Liu. Selective growth of well-aligned semiconducting single-walled carbon nanotubes. *Nano letters*, 9(2):800–805, 2009.

[86] H. Huang, C. H. Liu, Y. Wu, and S. Fan. Aligned carbon nanotube composite films for thermal management. *Advanced Materials*, 17(13):1652–1656, 2005.

[87] J. C. Peltier, P. Fleurial, L. Gailliard, R. Triboulet, H. Scherrer, and S. Scherrer. Thermal properties of high quality single crystals of bismuth telluride, Part I: Experimental characterization. *Journal of Physics and Chemistry of Solids*, 49(10):1237 – 1247, 1988.

[88] A. F. Gibson, editor. *Progress in semiconductors. Volume 7.* Heywood, London, 1963.

[89] Norman Neill Greenwood. *Chemistry of the elements.* Butterworth-Heinemann, Oxford, 2nd ed edition, 1997.

[90] D. A. Wright. Materials for direct-conversion thermoelectric generators. *International Materials Reviews*, 15(1):147–160, 1970.

[91] A. A. Machonis and I. B. Cadoff. Investigation of alloys of the system PbTe-SnTe. *Trans. Met. Soc. AIME*, 230:333–339, 1964.

[92] Ronald J. Gripshover, John B. VanZytveld, and Jack Bass. Thermopower of pure aluminum. *Phys. Rev.*, 163:598–603, Nov 1967.

[93] Diederick Jan van Ooijen. *The thermoelectric power of copper, silver and gold after coldworking.* PhD thesis, 's-Gravenhage Nertherland, 1957.

[94] Dawid Janas and Krzysztof K. Koziol. Rapid electrothermal response of high-temperature carbon nanotube film heaters. *Carbon*, 59(0):457 – 463, 2013.

[95] Bed Poudel, Qing Hao, Yi Ma, Yucheng Lan, Austin Minnich, Bo Yu, Xiao Yan, Dezhi Wang, Andrew Muto, Daryoosh Vashaee, Xiaoyuan Chen, Junming Liu, Mildred S. Dresselhaus, Gang Chen, and Zhifeng Ren. High-thermoelectric performance of nanostructured bismuth antimony telluride bulk alloys. *Science*, 320(5876):634–638, 2008.

[96] R. Murugasami, P. Vivekanandhan, S. Kumaran, R. Suresh Kumar, and T. John Tharakan. Thermoelectric power factor performance of silicon-germanium alloy doped with phosphorus prepared by spark plasma assisted transient liquid phase sintering. *Scripta Materialia*, 143:35 – 39, 2018.

[97] David M. Rowe. *Thermoelectrics Handbook: Macro to Nano*. Taylor & Francis, 2010.

[98] Saniya LeBlanc. Thermoelectric generators: Linking material properties and systems engineering for waste heat recovery applications. *Sustainable Materials and Technologies*, 1-2:26–35, dec 2014.

[99] Boris Russ, Anne Glaudell, Jeffrey J. Urban, Michael L. Chabinyc, and Rachel A. Segalman. Organic thermoelectric materials for energy harvesting and temperature control. *Nature Reviews Materials*, 1(10), aug 2016.

[100] Mario Culebras, Kyungwho Choi, and Chungyeon Cho. Recent progress in flexible organic thermoelectrics. *Micromachines*, 9(12):638, nov 2018.

[101] G-H. Kim, L. Shao, K. Zhang, and K. P. Pipe. Engineered doping of organic semiconductors for enhanced thermoelectric efficiency. *Nature Materials*, 12(8):719–723, may 2013.

[102] Desalegn A. Mengistie, Chang-Hsiao Chen, Karunakara M. Boopathi, Ferry W. Pranoto, Lain-Jong Li, and Chih-Wei Chu. Enhanced thermoelectric performance of PEDOT:PSS flexible bulky papers by treatment with secondary dopants. *ACS Applied Materials & Interfaces*, 7(1):94–100, dec 2014.

[103] Qin Yao, Qun Wang, Liming Wang, Yan Wang, Jing Sun, Huarong Zeng, Zhiyue Jin, Xianliang Huang, and Lidong Chen. The synergic regulation of conductivity and Seebeck coefficient in pure polyaniline by chemically changing the ordered degree of molecular chains. *J. Mater. Chem. A*, 2(8):2634–2640, 2014.

[104] Hongfei Zhu, Congcong Liu, Haijun Song, Jingkun Xu, Fangfang Kong, and Jianmin Wang. Thermoelectric performance of poly(3-hexylthiophene) films doped by iodine vapor with promising high Seebeck coefficient. *Electronic Materials Letters*, 10(2):427–431, mar 2014.

[105] Chungyeon Cho, Kevin L. Wallace, Ping Tzeng, Jui-Hung Hsu, Choongho Yu, and Jaime C. Grunlan. Outstanding low temperature thermoelectric power factor from completely organic thin films enabled by multidimensional conjugated nanomaterials. *Advanced Energy Materials*, 6(7):1502168, jan 2016.

[106] Chungyeon Cho, Bart Stevens, Jui-Hung Hsu, Ricky Bureau, David A. Hagen, Oren Regev, Choongho Yu, and Jaime C. Grunlan. Completely organic multilayer thin film with thermoelectric power factor rivaling inorganic tellurides. *Advanced Materials*, 27(19):2996–3001, apr 2015.

[107] D.J Benford, T.J Powers, and S.H Moseley. Thermal conductivity of kapton tape. *Cryogenics*, 39(1):93 – 95, 1999.

[108] N. I. Erzin and Makov N. V. Bonding of thermoelements in thermoelectric devices. *Applied Solar Energy*, 1:32–39, 1965.

[109] Dinesh K. Aswal, Ranita Basu, and Ajay Singh. Key issues in development of thermoelectric power generators: High figure-of-merit materials and their highly conducting interfaces with metallic interconnects. *Energy Conversion and Management*, 114:50–67, apr 2016.

[110] Ka Xiong, Weichao Wang, Husam N Alshareef, Rahul P Gupta, John B White, Bruce E Gnade, and Kyeongjae Cho. Electronic structures and stability of Ni/Bi_2Te_3 and Co/Bi_2Te_3 interfaces. *Journal of Physics D: Applied Physics*, 43(11):115303, mar 2010.

[111] Agnieszka Lekawa-Raus, Jeff Patmore, Lukasz Kurzepa, John Bulmer, and Krzysztof Koziol. Electrical properties of carbon nanotube based fibers and their future use in electrical wiring. *Advanced Functional Materials*, 24(24):3661–3682, mar 2014.

[112] Johannes Svensson and Eleanor E. B. Campbell. Schottky barriers in carbon nanotube-metal contacts. *Journal of Applied Physics*, 110(11):111101, dec 2011.

[113] Seong Chu Lim, Jin Ho Jang, Dong Jae Bae, Gang Hee Han, Sunwoo Lee, In-Seok Yeo, and Young Hee Lee. Contact resistance between metal and carbon nanotube interconnects: Effect of work function and wettability. *Applied Physics Letters*, 95(26):264103, dec 2009.

[114] Shafi Ullah Khan, Jayaram R. Pothnis, and Jang-Kyo Kim. Effects of carbon nanotube alignment on electrical and mechanical properties of epoxy nanocomposites. *Composites Part A: Applied Science and Manufacturing*, 49:26 – 34, 2013.

[115] K.-Y. Chun, Y. Oh, J. Rho, J.-H. Ahn, Y.-J. Kim, H.R. Choi, and S. Baik. Highly conductive, printable and stretchable composite films of carbon nanotubes and silver. *Nature Nanotechnology*, 5(12):853–857, 2010. cited By 287.

[116] Brigitte Vigolo, Alain Pénicaud, Claude Coulon, Cédric Sauder, René Pailler, Catherine Journet, Patrick Bernier, and Philippe Poulin. Macroscopic fibers and ribbons of oriented carbon nanotubes. *Science*, 290(5495):1331–1334, 2000.

[117] Jinhu Chen, James A. Trevarthen, Tong Deng, Michael S.A. Bradley, Sameer S. Rahatekar, and Krzysztof K.K. Koziol. Aligned carbon nanotube reinforced high performance polymer composites with low erosive wear. *Composites Part A: Applied Science and Manufacturing*, 67:86 – 95, 2014.

[118] Rajyashree M. Sundaram, Krzysztof K. K. Koziol, and Alan H. Windle. Continuous direct spinning of fibers of single-walled carbon nanotubes with metallic chirality. *Advanced Materials*, 23(43):5064–5068, 2011.

[119] L. A. Girifalco, Miroslav Hodak, and Roland S. Lee. Carbon nanotubes, buckyballs, ropes, and a universal graphitic potential. *Phys. Rev. B*, 62:13104–13110, Nov 2000.

[120] Jean-Paul Salvetat, G. Andrew D. Briggs, Jean-Marc Bonard, Revathi R. Bacsa, Andrzej J. Kulik, Thomas Stöckli, Nancy A. Burnham, and László Forró. Elastic and shear moduli of single-walled carbon nanotube ropes. *Phys. Rev. Lett.*, 82:944–947, Feb 1999.

[121] D. Qian, E. C. Dickey, R. Andrews, and T. Rantell. Load transfer and deformation mechanisms in carbon nanotube-polystyrene composites. *Applied Physics Letters*, 76(20):2868–2870, 2000.

[122] Joel R. Fried. *Polymer Science and Technology*, chapter 3: Conformation, Solutions, and Molecular Weight, pages 87–152. Prentice Hall, 2nd edition, 2003.

[123] Shane D. Bergin, Valeria Nicolosi, Philip V. Streich, Silvia Giordani, Zhenyu Sun, Alan H. Windle, Peter Ryan, N. Peter P. Niraj, Zhi-Tao T.

Wang, Leslie Carpenter, Werner J. Blau, John J. Boland, James P. Hamilton, and Jonathan N. Coleman. Towards solutions of single-walled carbon nanotubes in common solvents. *Advanced Materials*, 20(10):1876–1881, 2008.

[124] Reto Haggenmueller, Sameer S. Rahatekar, Jeffrey A. Fagan, Jaehun Chun, Matthew L. Becker, Rajesh R. Naik, Todd Krauss, Lisa Carlson, John F. Kadla, Paul C. Trulove, Douglas F. Fox, Hugh C. DeLong, Zhichao Fang, Shana O. Kelley, and Jeffrey W. Gilman. Comparison of the quality of aqueous dispersions of single wall carbon nanotubes using surfactants and biomolecules. *Langmuir*, 24(9):5070–5078, 2008. PMID: 18442227.

[125] Leah S. Witus, John-David R. Rocha, Virany M. Yuwono, Sergey E. Paramonov, R. Bruce Weisman, and Jeffrey D. Hartgerink. Peptides that noncovalently functionalize single-walled carbon nanotubes to give controlled solubility characteristics. *J. Mater. Chem.*, 17:1909–1915, 2007.

[126] M. Zheng, A. Jagota, E.D. Semke, B.A. Diner, R.S. McLean, S.R. Lustig, R.E. Richardson, and N.G. Tassi. DNA-assisted dispersion and separation of carbon nanotubes. *Nature Materials*, 2(5):338–342, 2003.

[127] Linda Vaisman, H. Daniel Wagner, and Gad Marom. The role of surfactants in dispersion of carbon nanotubes. *Advances in Colloid and Interface Science*, 128–130:37 – 46, 2006.

[128] Xiaolin Li, Li Zhang, Xinran Wang, Iwao Shimoyama, Xiaoming Sun, Won-Seok Seo, and Hongjie Dai. Langmuir−blodgett assembly of densely aligned single-walled carbon nanotubes from bulk materials. *Journal of the American Chemical Society*, 129(16):4890–4891, 2007. PMID: 17394327.

[129] Silvia Giordani, Shane D. Bergin, Valeria Nicolosi, Sergei Lebedkin, Manfred M. Kappes, Werner J. Blau, and Jonathan N. Coleman. Debundling of single-walled nanotubes by dilution: observation of large populations of individual nanotubes in amide solvent dispersions. *The Journal of Physical Chemistry B*, 110(32):15708–15718, 2006. PMID: 16898715.

[130] C. A. Furtado, U. J. Kim, H. R. Gutierrez, Ling Pan, E. C. Dickey, and Peter C. Eklund. Debundling and dissolution of single-walled carbon nanotubes in amide solvents. *Journal of the American Chemical Society*, 126(19):6095–6105, 2004. PMID: 15137775.

[131] Jonathan N. Coleman. Liquid-phase exfoliation of nanotubes and graphene. *Advanced Functional Materials*, 19(23):3680–3695, 2009.

[132] Wen-Bin Liu, Songfeng Pei, Jinhong Du, Bilu Liu, Libo Gao, Yang Su, Chang Liu, and Hui-Ming Cheng. Additive-free dispersion of single-walled carbon nanotubes and its application for transparent conductive films. *Advanced Functional Materials*, 21(12):2330–2337, 2011.

[133] S. Banerjee, T. Hemraj-Benny, and S. S. Wong. Covalent surface chemistry of single-walled carbon nanotubes. *Advanced Materials*, 17(1):17–29, 2005.

[134] V. Datsyuk, M. Kalyva, K. Papagelis, J. Parthenios, D. Tasis, A. Siokou, I. Kallitsis, and C. Galiotis. Chemical oxidation of multiwalled carbon nanotubes. *Carbon*, 46(6):833 – 840, 2008.

[135] Shanju Zhang, Ian A. Kinloch, and Alan H. Windle. Mesogenicity drives fractionation in lyotropic aqueous suspensions of multiwall carbon nanotubes. *Nano Letters*, 6(3):568–572, 2006. PMID: 16522064.

[136] V.A. Davis, L.M. Ericson, A.N.G. Parra-Vasquez, H. Fan, Y. Wang, V. Prieto, J.A. Longoria, S. Ramesh, R.K. Saini, C. Kittrell, W.E. Billups, W.W. Adams, R.H. Hauge, R.E. Smalley, and M. Pasquali. Phase behavior and rheology of SWNTs in superacids. *Macromolecules*, 37(1):154–160, 2004. cited By 249.

[137] V. A. Davis, A. N. G. Parra-Vasquez, M. J. Green, P. K. Rai, N. Behabtu, V. Prieto, R. D. Booker, J. Schmidt, E. Kesselman, W. Zhou, H. Fan, W. W. Adams, R. H. Hauge, J. E. Fischer, Y. Cohen, Y. Talmon, R. E. Smalley, and M. Pasquali. True solutions of single-walled carbon nanotubes for assembly into macroscopic materials. *Nature Nanotechnology*, 4(12):830–834, 2009.

[138] Jenny Hilding, Eric A. Grulke, Z. George Zhang, and Fran Lockwood. Dispersion of carbon nanotubes in liquids. *Journal of Dispersion Science and Technology*, 24(1):1–41, 2003.

[139] A. Nicholas G. Parra-Vasquez, Natnael Behabtu, Micah J. Green, Cary L. Pint, Colin C. Young, Judith Schmidt, Ellina Kesselman, Anubha Goyal, Pulickel M. Ajayan, Yachin Cohen, Yeshayahu Talmon, Robert H. Hauge, and Matteo Pasquali. Spontaneous dissolution of ultralong single- and

multiwalled carbon nanotubes. *ACS Nano*, 4(7):3969–3978, 2010. PMID: 20593770.

[140] Zheyi Chen, Kazufumi Kobashi, Urs Rauwald, Richard Booker, Hua Fan, Wen-Fang Hwang, and James M. Tour. Soluble ultra-short single-walled carbon nanotubes. *Journal of the American Chemical Society*, 128(32):10568–10571, 2006. PMID: 16895425.

[141] Richa Rastogi, Rahul Kaushal, S.K. Tripathi, Amit L. Sharma, Inderpreet Kaur, and Lalit M. Bharadwaj. Comparative study of carbon nanotube dispersion using surfactants. *Journal of Colloid and Interface Science*, 328(2):421 – 428, 2008.

[142] Konstantinos G. Dassios, Panagiota Alafogianni, Stelios K. Antiohos, Christos Leptokaridis, Nektaria-Marianthi Barkoula, and Theodore E. Matikas. Optimization of sonication parameters for homogeneous surfactant-assisted dispersion of multiwalled carbon nanotubes in aqueous solutions. *The Journal of Physical Chemistry C*, 119(13):7506–7516, 2015.

[143] Yu Wang, Chong-an Di, Yunqi Liu, Hisashi Kajiura, Shanghui Ye, Lingchao Cao, Dacheng Wei, Hongliang Zhang, Yongming Li, and Kazuhiro Noda. Optimizing single-walled carbon nanotube films for applications in electroluminescent devices. *Advanced Materials*, 20(23):4442–4449, 12 2008.

[144] Hyeong Taek Ham, Yeong Suk Choi, and In Jae Chung. An explanation of dispersion states of single-walled carbon nanotubes in solvents and aqueous surfactant solutions using solubility parameters. *Journal of Colloid and Interface Science*, 286(1):216 – 223, 2005.

[145] Linqin Jiang, Lian Gao, and Jing Sun. Production of aqueous colloidal dispersions of carbon nanotubes. *Journal of colloid and interface science*, 260(1):89—94, April 2003.

[146] Rajdip Bandyopadhyaya, Einat Nativ-Roth, Oren Regev, and Rachel Yerushalmi-Rozen. Stabilization of individual carbon nanotubes in aqueous solutions. *Nano Letters*, 2(1):25–28, 2002.

[147] Michael S. Strano, Valerie C. Moore, Michael K. Miller, Mathew J. Allen, Erik H. Haroz, Carter Kittrell, Robert H. Hauge, and R. E. Smalley. The role of surfactant adsorption during ultrasonication in the dispersion of

single-walled carbon nanotubes. *Journal of Nanoscience and Nanotechnology*, 3(1-1):81–86, 2003.

[148] Robert J. Hunter. *Foundations of colloid science*. Oxford University Press, 2nd edition, 2001.

[149] Michael J. O'Connell, Sergei M. Bachilo, Chad B. Huffman, Valerie C. Moore, Michael S. Strano, Erik H. Haroz, Kristy L. Rialon, Peter J. Boul, William H. Noon, Carter Kittrell, Jianpeng Ma, Robert H. Hauge, R. Bruce Weisman, and Richard E. Smalley. Band gap fluorescence from individual single-walled carbon nanotubes. *Science*, 297(5581):593–596, 2002.

[150] Olga Matarredona, Heather Rhoads, Zhongrui Li, Jeffrey H. Harwell, Leandro Balzano, and Daniel E. Resasco. Dispersion of single-walled carbon nanotubes in aqueous solutions of the anionic surfactant naddbs. *The Journal of Physical Chemistry B*, 107(48):13357–13367, 2003.

[151] M. F. Islam, E. Rojas, D. M. Bergey, A. T. Johnson, and A. G. Yodh. High weight fraction surfactant solubilization of single-wall carbon nanotubes in water. *Nano Letters*, 3(2):269–273, 2003.

[152] Koray Yurekli, Cynthia A. Mitchell, and Ramanan Krishnamoorti. Small-angle neutron scattering from surfactant-assisted aqueous dispersions of carbon nanotubes. *Journal of the American Chemical Society*, 126(32):9902–9903, 2004. PMID: 15303847.

[153] Panagiotis Angelikopoulos and Henry Bock. Directed self-assembly of surfactants in carbon nanotube materials. *The Journal of Physical Chemistry B*, 112(44):13793–13801, 2008. PMID: 18855463.

[154] Matteo Calvaresi, Marco Dallavalle, and Francesco Zerbetto. Wrapping nanotubes with micelles, hemimicelles, and cylindrical micelles. *Small*, 5(19):2191–2198, 2009.

[155] Evgeniy E. Tkalya, Marcos Ghislandi, Gijsbertus de With, and Cor E. Koning. The use of surfactants for dispersing carbon nanotubes and graphene to make conductive nanocomposites. *Current Opinion in Colloid & Interface Science*, 17(4):225 – 232, 2012.

[156] Timothy J. McDonald, Chaiwat Engtrakul, Marcus Jones, Garry Rumbles, , and Michael J. Heben. Kinetics of PL quenching during single-walled carbon nanotube rebundling and diameter-dependent surfactant interactions. *The Journal of Physical Chemistry B*, 110(50):25339–25346, 2006. PMID: 17165980.

[157] Toshiya Okazaki, Takeshi Saito, Koji Matsuura, Satoshi Ohshima, Motoo Yumura, and Sumio Iijima. Photoluminescence mapping of "as-grown" single-walled carbon nanotubes: a comparison with micelle-encapsulated nanotube solutions. *Nano Letters*, 5(12):2618–2623, 2005. PMID: 16351225.

[158] Beate Krause, Gudrun Petzold, Sven Pegel, and Petra Pötschke. Correlation of carbon nanotube dispersability in aqueous surfactant solutions and polymers. *Carbon*, 47(3):602 – 612, 2009.

[159] Sigma-Aldrich. Sodium dodecylbenzenesulfonate. datasheet 6.0, November 2016.

[160] F. Ray Bettley. The influence of detergents and surfactants on epidermal permiability. *British Journal of Dermatology*, 77(2):98–100, feb 1965.

[161] Ik Joon Kang, Junya Moroishi, Mitoshi Yamasuga, Sang Gyoon Kim, and Yuji Oshima. Swimming behavioral toxicity in japanese medaka (oryzias latipes) exposed to various chemicals for biological monitoring of water quality. In *Atmospheric and Biological Environmental Monitoring*, pages 285–293. Springer Netherlands, 2009.

[162] Ying Zhang, Jing Ma, Siyun Zhou, and Fang Ma. Concentration-dependent toxicity effect of SDBS on swimming behavior of freshwater fishes. *Environmental Toxicology and Pharmacology*, 40(1):77–85, jul 2015.

[163] Tomislav Ivanković and Jasna Hrenović. Surfactants in the environment. *Archives of Industrial Hygiene and Toxicology*, 61(1), jan 2010.

[164] Charanjeet Singh, Milo Shaffer, Ian Kinloch, and Alan Windle. Production of aligned carbon nanotubes by the CVD injection method. *Physica B: Condensed Matter*, 323(1–4):339 – 340, 2002. Proceedings of the Tsukuba Symposium on Carbon Nanotube in Commemoration of the 10th Anniversary of its Discovery.

[165] Charanjeet Singh, Milo S.P Shaffer, and Alan H Windle. Production of controlled architectures of aligned carbon nanotubes by an injection chemical vapour deposition method. *Carbon*, 41(2):359 – 368, 2003.

[166] Patrick J. Smith. *Chemistry of inkjet inks*, chapter 4: The behaviour of a droplet on the substrate, pages 55–72. World Scientific, 2010.

[167] Nicole D.R. Leifer, Malachi Noked, Gilbert D. Nessim, and Doron Aurbach. A straightforward and reliable method for the characterization of carbon nanotube dispersions. *Carbon*, 49(3):1042 – 1047, 2011.

[168] A. Windle. Processing: Superacids offer nanotube solution. *Nature Nanotechnology*, 4(12):800–801, 2009.

[169] Junrong Yu, Nadia Grossiord, Cor E. Koning, and Joachim Loos. Controlling the dispersion of multi-wall carbon nanotubes in aqueous surfactant solution. *Carbon*, 45(3):618 – 623, 2007.

[170] Adam J. Blanch, Claire E. Lenehan, and Jamie S. Quinton. Optimizing surfactant concentrations for dispersion of single-walled carbon nanotubes in aqueous solution. *The Journal of Physical Chemistry B*, 114(30):9805–9811, 2010. PMID: 20666522.

[171] Howard Wang, Wei Zhou, Derek L. Ho, Karen I. Winey, John E. Fischer, Charles J. Glinka, and Erik K. Hobbie. Dispersing single-walled carbon nanotubes with surfactants: a small angle neutron scattering study. *Nano Letters*, 4(9):1789–1793, 2004.

[172] W.M. Groenewoud. Thermogravimetry. In *Characterisation of Polymers by Thermal Analysis*, pages 61–76. Elsevier, 2001.

[173] João Paulo C. Trigueiro, Glaura G. Silva, Rodrigo L. Lavall, Clascídia A. Furtado, Sérgio Oliveira, Andre S. Ferlauto, Rodrigo G. Lacerda, Luiz O. Ladeira, Jiang-Wen Liu, Ray L. Frost, and Graeme A. George. Purity evaluation of carbon nanotube materials by thermogravimetric, TEM, and SEM methods. *Journal of Nanoscience and Nanotechnology*, 7(10):3477–3486, oct 2007.

[174] P. S. Gill, S. R. Sauerbrunn, and B. S. Crowe. High resolution thermogravimetry. *Journal of Thermal Analysis*, 38(3):255–266, mar 1992.

[175] Louis S. K. Pang, John D. Saxby, and S. Peter Chatfield. Thermogravimetric analysis of carbon nanotubes and nanoparticles. *The Journal of Physical Chemistry*, 97(27):6941–6942, jul 1993.

[176] David Bom, Rodney Andrews, David Jacques, John Anthony, Bailin Chen, Mark S. Meier, and John P. Selegue. Thermogravimetric analysis of the oxidation of multiwalled carbon nanotubes: evidence for the role of defect sites in carbon nanotube chemistry. *Nano Letters*, 2(6):615–619, jun 2002.

[177] W Zhou, Y.H Ooi, R Russo, P Papanek, D.E Luzzi, J.E Fischer, M.J Bronikowski, P.A Willis, and R.E Smalley. Structural characterization and diameter-dependent oxidative stability of single wall carbon nanotubes synthesized by the catalytic decomposition of CO. *Chemical Physics Letters*, 350(1-2):6–14, dec 2001.

[178] Elisabeth Mansfield, Aparna Kar, and Stephanie A. Hooker. Applications of TGA in quality control of SWCNTs. *Analytical and Bioanalytical Chemistry*, 396(3):1071–1077, 2010.

[179] F. Villalpando-Paez, A. Zamudio, A.L. Elias, H. Son, E.B. Barros, S.G. Chou, Y.A. Kim, H. Muramatsu, T. Hayashi, J. Kong, and et al. Synthesis and characterization of long strands of nitrogen-doped single-walled carbon nanotubes. *Chemical Physics Letters*, 424(4-6):345 – 352, Jun 2006.

[180] Robert Murphy, Jonathan N. Coleman, Martin Cadek, Brendan McCarthy, Matthew Bent, Anna Drury, Robert C. Barklie, and Werner J. Blau. High-yield, nondestructive purification and quantification method for multiwalled carbon nanotubes. *The Journal of Physical Chemistry B*, 106(12):3087–3091, 2002.

[181] K.L. Lu, R.M. Lago, Y.K. Chen, M.L.H. Green, P.J.F. Harris, and S.C. Tsang. Mechanical damage of carbon nanotubes by ultrasound. *Carbon*, 34(6):814–816, 1996.

[182] Kingsuk Mukhopadhyay, Chandra Dhar Dwivedi, and Gyanesh Narayan Mathur. Conversion of carbon nanotubes to carbon nanofibers by sonication. *Carbon*, 40(8):1373 – 1376, 2002.

[183] Corey A. Hewitt, Matt Craps, Richard Czerw, and David L. Carroll. The effects of high energy probe sonication on the thermoelectric power of large

diameter multiwalled carbon nanotubes synthesized by chemical vapor deposition. *Synthetic Metals*, 184:68 – 72, 2013.

[184] Frank Hennrich, Ralph Krupke, Katharina Arnold, Jan A. Rojas Stütz, Sergei Lebedkin, Thomas Koch, Thomas Schimmel, and Manfred M. Kappes. The mechanism of cavitation-induced scission of single-walled carbon nanotubes. *The Journal of Physical Chemistry B*, 111(8):1932–1937, mar 2007.

[185] Antoine Lucas, Cécile Zakri, Maryse Maugey, Matteo Pasquali, Paul van der Schoot, and Philippe Poulin. Kinetics of nanotube and microfiber scission under sonication. *The Journal of Physical Chemistry C*, 113(48):20599–20605, nov 2009.

[186] Philip G. Collins, Keith Bradley, Masa Ishigami, and A. Zettl. Extreme oxygen sensitivity of electronic properties of carbon nanotubes. *Science*, 287(5459):1801–1804, 2000.

[187] Keith Bradley, Seung-Hoon Jhi, Philip G. Collins, J. Hone, Marvin L. Cohen, S. G. Louie, and A. Zettl. Is the intrinsic thermoelectric power of carbon nanotubes positive? *Phys. Rev. Lett.*, 85:4361–4364, Nov 2000.

[188] R. S. Lee, H. J. Kim, J. E. Fischer, A. Thess, and R. E. Smalley. Conductivity enhancement in single-walled carbon nanotube bundles doped with K and Br. *Nature*, 388(6639):255–257, 07 1997.

[189] Choongho Yu, Advaith Murali, Kyungwho Choi, and Yeontack Ryu. Air-stable fabric thermoelectric modules made of n- and p-type carbon nanotubes. *Energy & Environmental Science*, 5(11):9481–9486, 2012.

[190] Yeontack Ryu, Dallas Freeman, and Choongho Yu. High electrical conductivity and n-type thermopower from double-/single-wall carbon nanotubes by manipulating charge interactions between nanotubes and organic/inorganic nanomaterials. *Carbon*, 49(14):4745 – 4751, 2011.

[191] Mingxing Piao, Junhong Na, Jaewan Choi, Jaesung Kim, Gary P. Kennedy, Gyutae Kim, Siegmar Roth, and Urszula Dettlaff-Weglikowska. Increasing the thermoelectric power generated by composite films using chemically functionalized single-walled carbon nanotubes. *Carbon*, 62:430–437, Oct 2013.

[192] Yoshiyuki Nonoguchi, Kenji Ohashi, Rui Kanazawa, Koji Ashiba, Kenji Hata, Tetsuya Nakagawa, Chihaya Adachi, Tomoaki Tanase, and Tsuyoshi Kawai. Systematic conversion of single walled carbon nanotubes into n-type thermoelectric materials by molecular dopants. *Scientific Reports*, 3:3344 EP –, 11 2013.

[193] Dallas D. Freeman, Kyungwho Choi, and Choongho Yu. N-type thermoelectric performance of functionalized carbon nanotube-filled polymer composites. *PLoS ONE*, 7(11):e47822, Nov 2012.

[194] C.P. Ewels and M. Glerup. Nitrogen doping in carbon nanotubes. *Journal of Nanoscience and Nanotechnology*, 5(9):1345–1363, 2005. cited By 281.

[195] M. Glerup, M. Castignolles, M. Holzinger, G. Hug, A. Loiseau, and P. Bernier. Synthesis of highly nitrogen-doped multi-walled carbon nanotubes. *Chem. Commun.*, pages 2542–2543, 2003.

[196] M. Terrones, H. Terrones, N. Grobert, W. K. Hsu, Y. Q. Zhu, J. P. Hare, H. W. Kroto, D. R. M. Walton, Ph. Kohler-Redlich, M. Rühle, J. P. Zhang, and A. K. Cheetham. Efficient route to large arrays of CNx nanofibers by pyrolysis of ferrocene/melamine mixtures. *Applied Physics Letters*, 75(25):3932–3934, 1999.

[197] Chengchun Tang, Yoshio Bando, Dmitri Golberg, and Fangfang Xu. Structure and nitrogen incorporation of carbon nanotubes synthesized by catalytic pyrolysis of dimethylformamide. *Carbon*, 42(12–13):2625 – 2633, 2004.

[198] Hyun Chul Choi, Seung Yong Bae, Jeunghee Park, Kwanyong Seo, Changwook Kim, Bongsoo Kim, Ha Jin Song, and Hyun-Joon Shin. Experimental and theoretical studies on the structure of N-doped carbon nanotubes: Possibility of intercalated molecular n2. *Applied Physics Letters*, 85(23):5742–5744, 2004.

[199] Iuliana P. Morjan, Rodica Alexandrescu, Ion Morjan, Catalin Luculescu, Eugeniu Vasile, Petre Osiceanu, Monica Scarisoreanu, and Gabriela Demian. Effect of the manufacturing parameters on the structure of nitrogen-doped carbon nanotubes produced by catalytic laser-induced chemical vapor deposition. *Journal of Nanoparticle Research*, 15(11):2045, 2013.

[200] S. Lefrant. Raman and SERS studies of carbon nanotube systems. *Current Applied Physics*, 2(6):479 – 482, 2002.

[201] John H. Lehman, Mauricio Terrones, Elisabeth Mansfield, Katherine E. Hurst, and Vincent Meunier. Evaluating the characteristics of multiwall carbon nanotubes. *Carbon*, 49(8):2581 – 2602, 2011.

[202] Roberta A. DiLeo, Brian J. Landi, and Ryne P. Raffaelle. Purity assessment of multiwalled carbon nanotubes by Raman spectroscopy. *Journal of Applied Physics*, 101(6):064307, 2007.

[203] Hao Liu, Yong Zhang, Ruying Li, Xueliang Sun, Sylvain Désilets, Hakima Abou-Rachid, Mounir Jaidann, and Louis-Simon Lussier. Structural and morphological control of aligned nitrogen-doped carbon nanotubes. *Carbon*, 48(5):1498 – 1507, 2010.

[204] Kyoung-Yong Chun, Heon Sang Lee, and Cheol Jin Lee. Nitrogen doping effects on the structure behavior and the field emission performance of double-walled carbon nanotubes. *Carbon*, 47(1):169 – 177, 2009.

[205] Stephen Maldonado, Stephen Morin, and Keith J. Stevenson. Structure, composition, and chemical reactivity of carbon nanotubes by selective nitrogen doping. *Carbon*, 44(8):1429 – 1437, 2006.

[206] David G. Cahill. Thermal conductivity measurement from 30 to 750 K: the 3ω method. *Review of Scientific Instruments*, 61(2):802–808, 1990.

[207] David G. Cahill and R. O. Pohl. Thermal conductivity of amorphous solids above the plateau. *Phys. Rev. B*, 35:4067–4073, Mar 1987.

[208] L. Lu, W. Yi, and D. L. Zhang. 3ω method for specific heat and thermal conductivity measurements. *Review of Scientific Instruments*, 72(7):2996–3003, 2001.

[209] Bartosz M. Zawilski, Roy T. Littleton IV, and Terry M. Tritt. Description of the parallel thermal conductance technique for the measurement of the thermal conductivity of small diameter samples. *Review of Scientific Instruments*, 72(3):1770–1774, 2001.

[210] Nayandeep K. Mahanta and Alexis R. Abramson. The dual-mode heat flow meter technique: A versatile method for characterizing thermal conductiv-

ity. *International Journal of Heat and Mass Transfer*, 53(23–24):5581 – 5586, 2010.

[211] Michael B. Jakubinek, Michel B. Johnson, Mary Anne White, Chaminda Jayasinghe, Ge Li, Wondong Cho, Mark J. Schulz, and Vesselin Shanov. Thermal and electrical conductivity of array-spun multi-walled carbon nanotube yarns. *Carbon*, 50(1):244 – 248, 2012.

[212] Brian Derby. Inkjet printing of functional and structural materials: Fluid property requirements, feature stability, and resolution. *Annual Review of Materials Research*, 40(1):395–414, jun 2010.

[213] Krisztián Kordás, Tero Mustonen, Géza Tóth, Heli Jantunen, Marja Lajunen, Caterina Soldano, Saikat Talapatra, Swastik Kar, Robert Vajtai, and Pulickel M Ajayan. Inkjet printing of electrically conductive patterns of carbon nanotubes. *Small*, 2(8-9):1021–1025, 2006.

[214] Andrea Montecucco and Andrew R. Knox. Maximum power point tracking converter based on the open-circuit voltage method for thermoelectric generators. *IEEE Transactions on Power Electronics*, 30(2):828–839, feb 2015.

[215] Chuang Yu and K.T. Chau. Thermoelectric automotive waste heat energy recovery using maximum power point tracking. *Energy Conversion and Management*, 50(6):1506–1512, jun 2009.

[216] Agnieszka Lekawa-Raus. *Carbon nanotube fibres for electrical wiring applications*. PhD thesis, University of Cambridge, 2012.